Fall 9-27-2019

Modeling and Control of Magnetic Gear Dynamics in a Wind Turbine Drivetrain

Danielle Vournas
Portland State University

Modeling and Control of Magnetic Gear Dynamics in a Wind Turbine Drivetrain

by

Danielle Gené Vournas

A thesis submitted in partial fulfillment of the
requirements for the degree of

Master of Science
in
Electrical and Computer Engineering

Thesis Committee:
Dr. Jonathan Bird, Chair
Dr. Robert Bass
Dr. John Lipor

Portland State University
2019

Abstract

This thesis looks at the modeling and simulation of linear and nonlinear magnetic gear dynamics in a wind turbine drivetrain. The objective is to lay the groundwork for analysis, modeling and optimization of control structures focused on pole-slip prevention. A classical mechanical two-mass torsion spring model is used as the basis for developing the dynamic system equations and Simulink models. The wind turbine torque input to the low speed rotor is modeled as a disturbance input, the generator torque is modeled as a controlled input, and the high-speed rotor speed is the only measured output. The nonlinear dynamics are linearized; and a state space model is built that utilizes both gear rotor speeds and the load angle as states. A state space feedback compensation controller is designed using pole placement techniques; and the sensitivity of the selected poles is tested across the full range of rated load angles. A full order observer is combined with state feedback compensation and the performance is evaluated with and without load angle speed regulation and integral action. A reduced order observer is designed with load torque estimation as an additional ‘metastate’, which is then used to calculate the load angle, providing a better estimate than what the observer directly provides. Finally, the accuracy of the reduced order observer to is tested using real torque data from a wind turbine.

This work was in part supported by the National Science Foundation under award 1636704 and award number 1827801.

Acknowledgements

The author would like to thank Dr. Jonathan Bird for providing the opportunity to participate in magnetic gear research; and for providing direction, support and encouragement throughout the arc of thesis development. Eternal gratitude goes to my partner, Jonathan Jelen, for being patient and supportive every step of the way.

Table of Contents

List of Tables

List of Figures

1 Introduction

1.1 Background

Magnetic gears show promise as an alternative to mechanical gears, providing a way to increase or decrease speed without any mechanical contact between gears. Torque is transmitted by a magnetic gear utilizing magnetic field space modulation. The benefits of contact-less torque transmission include a reduction in wear and tear resulting in less maintenance requirements, elimination of the need for lubrication and the risk of lubrication leaks, and quieter operation than mechanical gears [1]. These features make them a good option for use in wind turbines and ocean wave energy generators. The arc of their development shows continued improvements in torque density and power conversion efficiency that may eventually allow them to surpass their mechanical counterparts [2]. As energy demand increases, so does the need for gearboxes with increasing volumetric torque density. This is because increased capacity wind turbines have longer blades and sit on top of taller towers (Figure 1.1, [3]), creating a need to reduce the weight of the gearbox. Another potential benefit of magnetic gears is the fact that overload torque will cause the rotors to break contact without rotor damage. This overload torque feature, known as pole slipping, could make them a particularly good replacement in wind turbines, where mechanical gearbox failures account for approximately 20% of downtime [4].

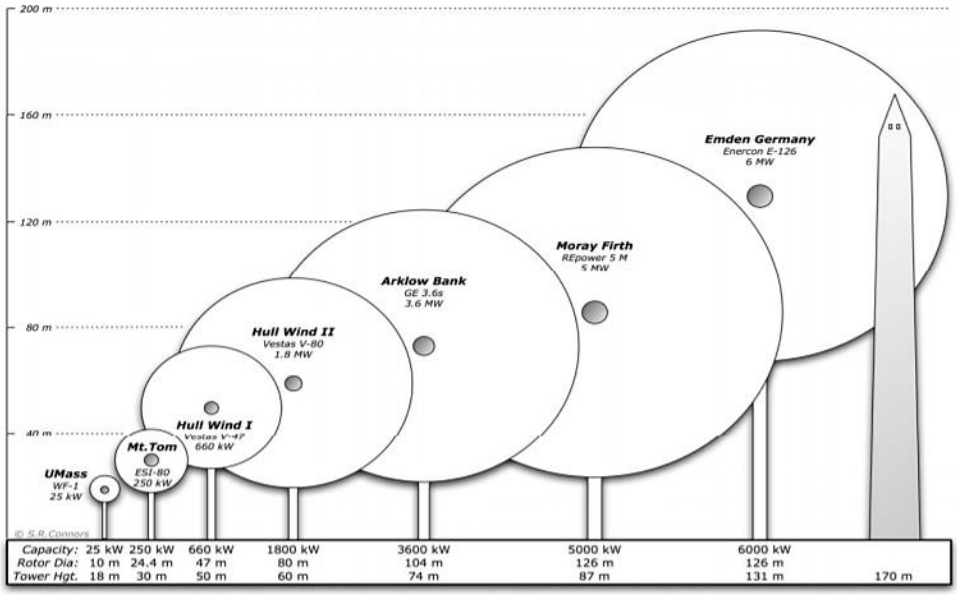

Figure 1.1. Tower height, swept rotor diameter and rated capacity of existing onshore and offshore wind turbines [3].

Magnetic gears could generally be considered as being in the technology development phase more than application development. There are far more papers being published on gear design and optimization than on control. Much work has been and continues to be done to optimize different magnetic gear typologies in terms of peak torque, efficiency, torque density, vibration reduction, as well as developing them with variable transmission capabilities and integrating them into permanent magnet machines [5]. While these developments are all key to making magnetic gears a viable replacement for mechanical, the dynamic control of magnetic gears in a stiff mechanical drivetrain needs to be addressed as well. The most common control objectives for a mechanical gear in a mechanical drivetrain are to:

- Track the speed or position of the load to a desired setpoint, with minimal overshoot and fast response time.

- Reject load torque disturbances while tracking the setpoint, also known as regulation [6].
- Minimize torsional vibrations or resonance.

A control system designed for a magnetic gear replacing a mechanical gear must also satisfy these objectives, but there are some unique characteristics of magnetic transmission that need to be considered and addressed in the design. Initially, however, the dynamic model of a magnetic gear in a drivetrain can be (and frequently has been) approximated by a well-known mechanical model - two rotating mass/inertias connected through a torsion spring.

1.2 Two-Mass Model of a Mechanical Coupling

It has been frequently proposed [7-14] that, for the purpose of control system design, elements that are mechanically coupled in a drivetrain where coupling flexibility is a factor can be modeled as two mass/inertias coupled by a torsion spring. Common examples include rolling mills, machining tools, flexible joint robots, and ball screw positioning systems [14] where two rotating masses represent a load coupled to a driving motor through a compliant, flexible shaft or joint. Figure 1.2 shows a model of this system, where T_{EM} is the electromagnetic torque developed by the motor and J_M, B_M, ω_M, and θ_M are the lumped inertia, damping, speed, and angular position of the motor, respectively. The torque transferred through the shaft, T_S, is a function of the shaft/spring stiffness, K_S and the angular difference between the motor angular position, θ_M, and the load angular position, θ_L, such that

$$\theta_D = \theta_M - \theta_L \tag{1.1}$$

where the transmission torque is then

$$T_S = K_S \theta_D . \tag{1.2}$$

The inertia, speed and torque developed by the load are J_L, ω_L, and T_L respectively. Because the coupling is compliant, changes in speed or position commanded from the motor side and/or disturbance torque changes on the load side will result in a transient period where the speed and position of the motor are different from that of the load. Another negative consequence of shaft compliance is that torque changes on either the motor or load sides can lead to torsional vibrations or resonance, which can make speed/position control difficult and cause mechanical stress or even failure [15].

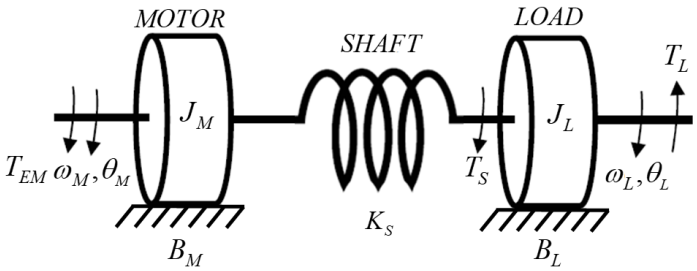

Figure 1.2. Two mass model of a compliant mechanical coupling

1.3 Two-Mass Model of a Magnetic Gear

In order to use the two-mass model of a mechanical coupling for a magnetic gear, the following things must be considered. First, while a magnetic gear has a gear ratio, that does not preclude it from being modeled as a 1:1 magnetic coupling. Magnetic torque transmission can be effectively modeled according to [16] as a 1:1 coupling connecting two geared mass/inertias. A representation of this can be seen in Figure 1.3. The gear, with gear ratio n_2 / n_1, is separated into two gearboxes, a step up and a step down. In this way the stiffness component of the transmission dynamics is separated from the gearing component.

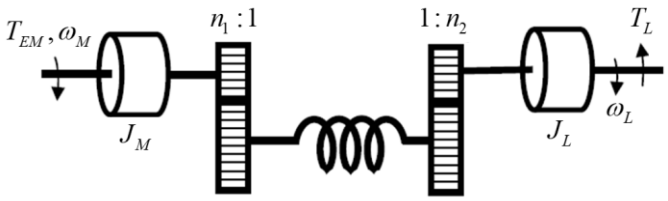

Figure 1.3. Equivalent model of a magnetic gear [16]

The second thing that should be noted is that the stiffness or compliance of magnetic gear rotors is non-linear, whereas it is generally considered to be linear in mechanical couplings. This concept was illustrated nicely by [16], repeated here in Figure 1.4.

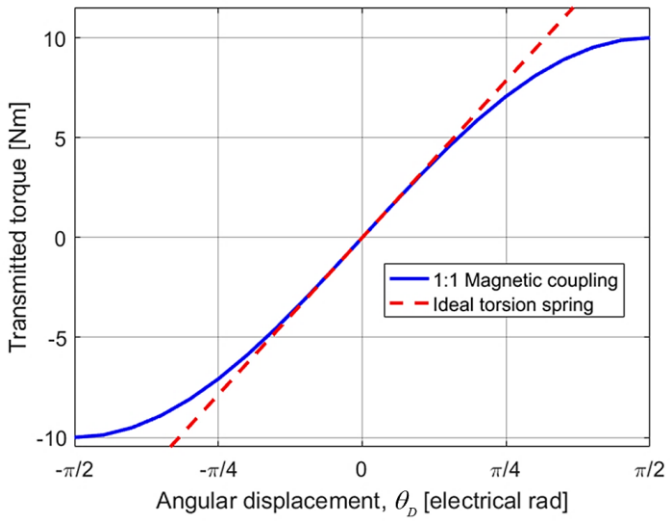

Figure 1.4. Comparison of torque transferred through an ideal torsion spring and a magnetic coupling [16]

The dashed line depicts torque transferred through an ideal torsion spring/mechanical coupling, as a function of angular displacement (1.1) between the motor and the load. As the angular displacement increases, the transmitted torque increases, but the relationship is linear. In the context of the two-mass model, the slope of this line is the spring constant, K_S shown in Figure 1.2, with typical units of [Nm/rad]. Here, the angle is given in electrical radians to illustrate an important point. The peak torque transferred through a magnetic gear always occurs at +/- 90 electrical degrees or +/- π/2 radians. This is the stable operating region for torque transfer, but it is also clear from Figure 1.4 that the transfer is not linear over this entire operating range. The torque transferred through a magnetic gear is, in fact, sinusoidal, as shown in (Figure 1.5), accordingly

$$T_t = T_m \sin(\theta_M - \theta_L) \tag{1.3}$$

for a 1:1 magnetic coupling, and

$$T_t = T_m \sin(n_1\theta_M - n_2\theta_L) \tag{1.4}$$

for a magnetic gear with the gear ratio shown in Figure 1.3. T_m is the peak or pullout torque of the gear; and the parameter defined by

$$n_1\theta_M - n_2\theta_L \tag{1.5}$$

is called the load angle, ϕ. This will be discussed in more detail in Chapter 2. Referring to Figure 1.5, there are stable and unstable regions of torque transmission. Note the rate of torque transfer decreases approaching peak torque, which could influence the actual peak torque achievable. Also, if the load angle reaches an unstable region, pole slipping will occur.

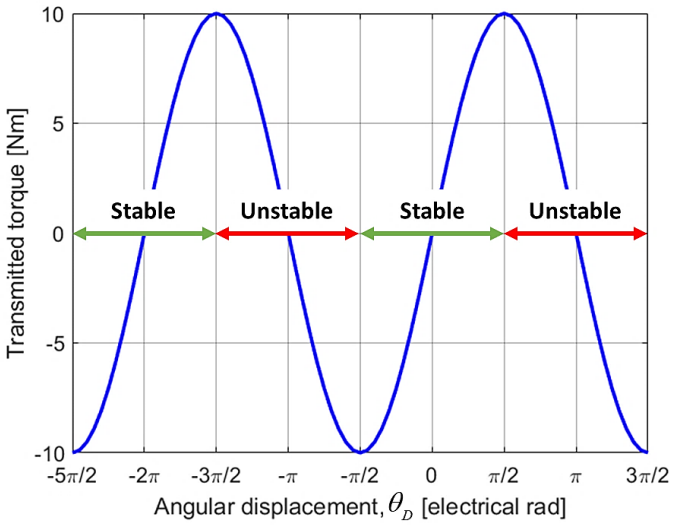

Figure 1.5. Stable and unstable regions of torque transmission.

The phenomenon of pole slipping in magnetic gears is frequently pointed to as beneficial torque overload protection. Part of what makes mechanical gears prone to failure, particularly in wind turbine generators, is that when they are subject to large load

transients, they maintain physical contact until the transient passes, or they fail catastrophically. Magnetic gears do not operate through physical contact and the magnetic field connection will break rotor contact if the transient torque is beyond the rated torque of the gear. This phenomenon is known as pole slipping. When this happens, the rotors spin freely, slowing down to 0 or maintain speed in accordance with the dynamics on each side. An example of pole slipping, from experiments performed by [16] using a 1:1 magnetic coupling, is shown in Figure 1.6. The speed responses of the motor and load side rotors are shown, following an overload torque at t = 2 s. Contact between the coupling rotors is broken and the speed on both sides eventually drops to 0. The fact that the speed of both sides goes to 0 indicates that there are no torque inputs to either side following the overload event.

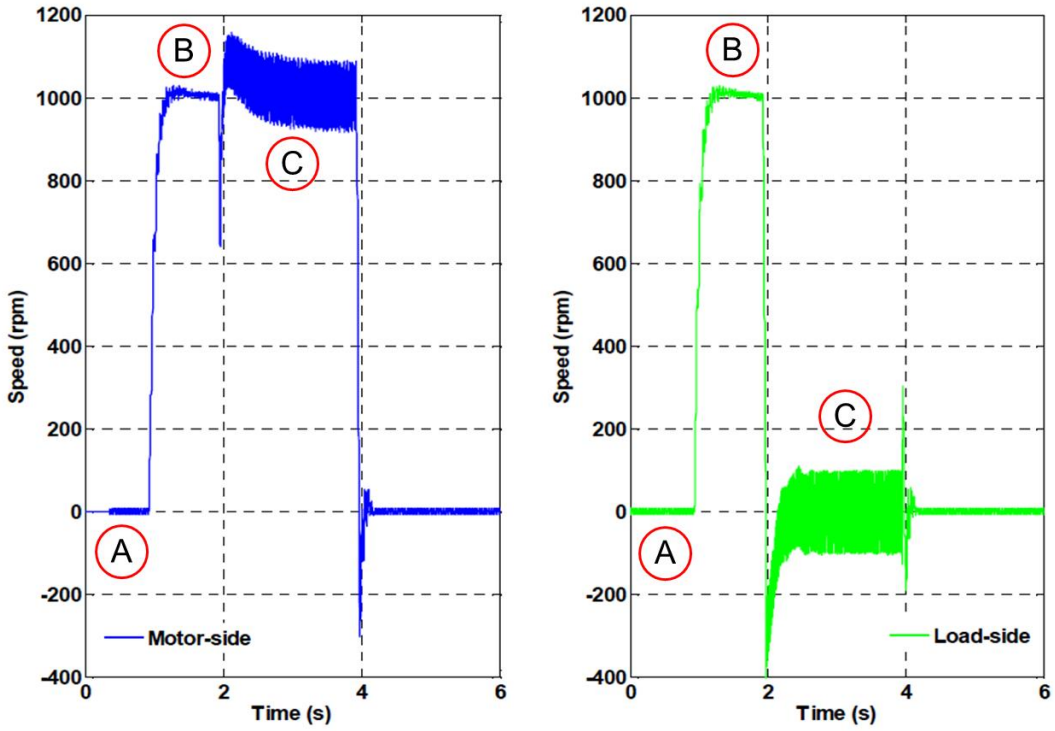

Figure 1.6. Motor and load side rotor speed response of a 1:1 magnetic coupling. Starting at 0 Nm of load torque (A), the load torque increases at t = 1 s (B). An increase again at t = 2s (C) leads to pole slipping [16].

The gear rotors of the magnetic gear will eventually re-engage, given the right conditions, essentially allowing it to serve the function of a torque 'breaker'. While it is clear how this can be a benefit, it also represents a loss of control of the drivetrain. A sudden loss of contact at high speeds could have damaging oscillatory effects on the drivetrain [17]. If a control system were in place to monitor, detect, and remediate pole slipping, preventative schemes could be employed to reduce occurrences; and protocols could be set for bringing the gear rotors back into synchronism as quickly as possible. Non-linear stiffness and pole-slipping are the key features of magnetic transmission that this thesis will examine as a part of the control system design.

1.4 Review of Magnetic Gear Control

At the time this thesis was written, there were less than 10 published papers or theses discussing pole-slip prevention and recovery for magnetically geared drivetrains [16, 18-23]; and they were all published by the same two groups of authors. All the magnetic gear control techniques presented in these papers were developed for mechanical servo drive systems, like the one shown in Figure 1.2. Speed control of a drivetrain incorporating a magnetic gear integrated with a permanent magnet machine (pseudo direct drive) was investigated by Bouheraoua [18]. Speed and position control of a drivetrain incorporating a 1:1 magnetic coupling was investigated by Montague [16]. Several control techniques were explored for the purposes of tracking, regulation, and reduction of torsional oscillations, a summary of which is given below.

Controllers were developed for a single output system, meaning the assumption was made that only one of the system states could be measured. In general, it is assumed that in servo drive systems, only the motor-side states are available for measurement [18]. Conventional Integral (I), Proportional Integral (PI) and Proportional Derivative (PD) control structures were explored, utilizing motor-side feedback (speed or position) to track a setpoint. The overall findings were that I and PI control did not sufficiently damp torsional oscillations with the pseudo direct drive; and that PI and PD control did not adequately regulate load torque disturbances with the magnetic coupling. Full state feedback compensation gave better performance across all metrics.

A few techniques were evaluated for tuning the state feedback compensator gains. The simplest was pole placement design, where pole locations were selected to minimize the integral of the time-weighted absolute error (ITAE) performance index [16]. The most complex, and best performing, was a genetic algorithm, which used ITAE as a performance criterion, but optimized it further through iterative evaluations. This was presented by Bouheraoua, along with a Linear Quadratic Regulator (LQR) design, the latter of which performed poorly because no way was found to map the Q and R matrices to the desired performance index.

With full state feedback compensation identified as the best controller structure, and only one state available for measurement, steps were taken to integrate state feedback with state estimation. Linear full and reduced order observers were evaluated by both authors [16, 18]. A key finding from using linear state estimators on a nonlinear system was that the estimation was only accurate when the load angle that the observer was linearized around was close to the load angle at which the system was operating. There was more flexibility in the linear regions of operation (Figure 1.4), but the accuracy was still compromised in systems where the load torque/angle was fluctuating, if there was not a method established to update the linearization point in real time. One solution proposed, and successfully tested by Bouheraoua, was a non-linear observer in the form of an extended Kalman filter, which dynamically updated the load angle in real time.

Having a linearized state estimator that can track and respond to changes in the system, particularly with regards to the load angle, is a key component of control techniques for pole slip detection, prevention and recovery. Both authors developed slip

detection and prevention control schemes, both of which relied on measurements from the high-speed rotor to detect pole slipping. Montague [16] noted that pole slip conditions imposed a modulating signal on the speed feedback signal, which could be used as a detection variable. Bouheroaou [18] used an estimate of the load angle as a slip detection variable; and with the increased estimation accuracy provided by the extended Kalman filter, this was shown to be reliable. To implement slip prevention and recovery, both authors proposed control structures that utilized the feedback from slip detection to modify the speed of the motor so that synchronism with the load could be maintained.

1.5 Objectives and Scope

This thesis looks at the application of the mechanical two-mass model and some of the control techniques discussed in Section 1.4 to model the dynamics and control of a Halbach magnetic gear for a wind turbine drivetrain application. While a lot of work has been done to develop models for control of magnetic gears in mechanically stiff drivetrains, they have all been servomechanisms for motor-driven loads. The orientation of the magnetic gear in a wind turbine drivetrain is similar in that the disturbance still comes from the load side, but now it is also the driving input to the system. The main objective of this thesis is to lay the groundwork for modeling, analysis, and optimization of magnetic gear controls, specifically for pole-slip prevention in wind turbine drivetrains. The focus will be on control of the magnetic gear dynamics without integration into pitch angle control, generator control, or any other control structures that are typical for wind turbine systems. Since wind turbine speed is controlled by pitch

angle [24], the approach taken here is to focus on pole-slip prevention by using the generator input to avoid load angle overshoot conditions that cause the magnetic gear to pole slip. The magnetic gear used for simulations is modeled on an experimental prototype being developed in the Laboratory for Electromechanical Energy Conversion and Control at Portland State University.

2.1 Characteristics and Operation of a Coaxial Magnetic Gear

A prototype Halbach rotor coaxial magnetic gear was designed and constructed by Wong *et al* [25], a cross-sectional view of which is shown in Figure 2.1.

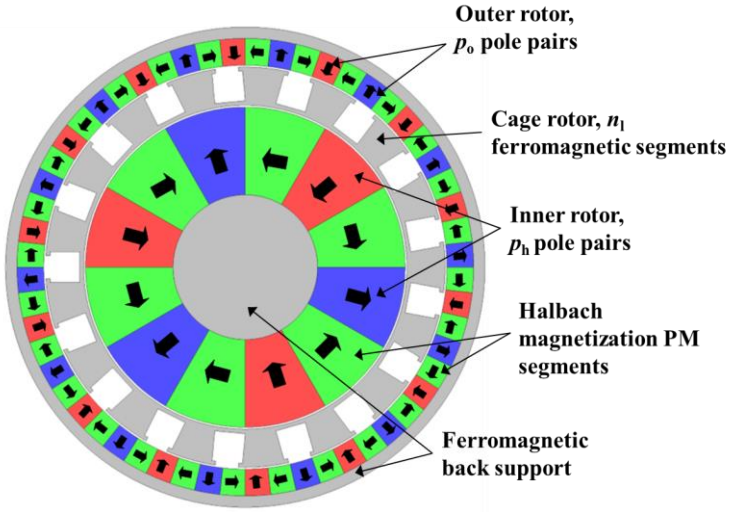

Figure 2.1. Prototype coaxial Halbach rotor magnetic gear [25]

The gear consists of three rotors, an outer permanent magnet (PM) rotor with p_o =14 pole pairs, an inner PM rotor with p_h =3 pole pairs and a cage rotor with n_l =17 ferromagnetic segments. In addition, a partial Halbach array (two PM segments per pole) has been added to both the outer and inner rotors. The Halbach PM array, first introduced by [26], utilizes PM pieces with a selected magnetization direction to help sinusoidally shape the air gap flux density distribution, potentially leading to increased torque and other benefits

[27]. The operation of the gear is as follows. The outer rotor is kept fixed (according to this design, other designs may choose to fix the cage rotor) while the inner and cage rotors are attached to separate drive shafts. The cage rotor rotates at speed ω_l and the inner rotor rotates at speed ω_h [1]. The angular speeds are related by

$$\omega_h = \frac{n_l}{p_h}\omega_l \tag{2.1}$$

The rotation of the ferromagnetic cage rotor with respect to the PM rotor creates magnetic fields in the air gaps between them. The cage rotor modulates the magnetic field flux density in the air gaps, the dominant space harmonics of which can be tuned to produce continuous torque transmission. If the number of pole pairs and ferromagnetic segments are selected such that:

$$n_l = p_h + p_o \tag{2.2}$$

the cage rotor will modulate the magnetic field so that each PM rotor interacts with a dominant space harmonic having an equal number of poles, thereby allowing for stable torque transmission through the gear while the rotors rotate at different speeds [27]. The gear ratio is then defined as:

$$G_r = \frac{n_l}{p_h} = 5.67 \tag{2.3}$$

If losses are neglected, the power transmission relationship between rotors is given by

$$|T_l|\omega_l = |T_h|\omega_h \tag{2.4}$$

From (2.1), (2.3) and (2.4) it is clear that when the outer rotor is fixed, the cage rotor is the low speed, high torque side and the inner rotor is the high speed, low torque side of the gear.

2.2 Dynamic Operation in a Wind Turbine Drivetrain

If the Halbach magnetic gear replaces a mechanical gearbox in a wind turbine drivetrain, the aerodynamic wind turbine torque will rotate an input drive shaft to the gearbox, which will be attached to the magnetic gear cage or low speed rotor (LSR). Rotating wind turbine blades have a large amount of torque but do not rotate at the speed necessary to maintain grid frequency [28]. The power transmitted from the LSR to the inner, high speed rotor (HSR) constitutes a decrease in torque and an increase in speed. The shaft attached to the HSR provides the input speed to a generator. The torque transmitted to the LSR side is given by:

$$T_t(\phi) = T_{\mathrm{m}} \sin(\phi) \tag{2.5}$$

and referred to the HSR side it is given by:

$$\begin{aligned} T_{th}(\phi) &= \frac{T_{\mathrm{m}}}{G_r} \sin(\phi) \\ &= \frac{T_t(\phi)}{G_r} \end{aligned} \tag{2.6}$$

where

$$\phi = n_l \theta_l - p_h \theta_h \tag{2.7}$$

is the angular displacement between the rotors, or load angle, T_m is the pullout torque of the gear referred to the LSR, G_r is the gear ratio defined in (2.3), and θ_l and θ_h are the angular positions of the LSR and HSR respectively. Combining (2.5) and (2.7) gives a more developed expression for magnetic torque

$$T_t(\phi) = T_{\mathrm{m}} \sin[n_l\theta_l - p_h\theta_h] \tag{2.8}$$

Now, at initial time t=0, the load angle between rotors is assumed to be

$$\phi(0) = n_l\theta_{l0} - p_h\theta_{h0} \tag{2.9}$$

where θ_{l0} and θ_{h0} are the initial angular positions of the high and low speed rotors at time t=0. This initial (steady state) load angle will also be defined as

$$\phi(0) = \phi_0 \tag{2.10}$$

Then, defining:

$$\dot{\theta}_l = \omega_l \tag{2.11}$$

$$\dot{\theta}_h = \omega_h \tag{2.12}$$

the change in load angle, or load angle speed is given by

$$\dot{\phi} = n_l\omega_l - p_h\omega_h \tag{2.13}$$

In steady state

$$\dot{\phi} = 0 \tag{2.14}$$

and we can define steady state load angle speed as

$$\dot{\phi}_0 = n_l\omega_{l0} - p_h\omega_{h0} = 0 \tag{2.15}$$

where ω_{l0} and ω_{h0} are the steady state angular speeds at time $t = 0$. The complete non-linear dynamic operating equations for the magnetic gear in a wind turbine drivetrain, with sign definition given by [28] are [18]:

$$J_l \dot{\omega}_l = T_l - T_t(\phi) - B_l \omega_l + G_r k_d \dot{\phi} \tag{2.16}$$

$$J_h \dot{\omega}_h = \frac{T_t(\phi)}{G_r} - T_g - B_h \omega_h - k_d \dot{\phi} \tag{2.17}$$

where T_l is the aerodynamic torque, T_g is the electromagnetic braking torque developed by the generator, J_l is the low-speed side lumped inertia of the magnetic gear and J_h is the high-speed side lumped inertia. There are two sources of damping in (2.16) and (2.17). B_l and B_h are viscous damping of the LSR and HSR respectively [16]. The other source of damping, k_d, is a function of the angular speed between the rotors, due to eddy current and iron losses. It will be assumed, moving forward, that the losses in the magnetic gear are small and so these sources of damping will be negligible compared to the damping introduced by the controller; they will generally be neglected. If damping is neglected, (2.16) and (2.17) reduce to

$$J_l \dot{\omega}_l = T_l - T_t(\phi) \tag{2.18}$$

$$J_h \dot{\omega}_h = \frac{T_t(\phi)}{G_r} - T_g \tag{2.19}$$

Taking the Laplace transforms and rearranging, (2.18) and (2.19) become

$$\omega_l = \frac{1}{sJ_l}(T_l - T_t(\phi)) \tag{2.20}$$

$$\omega_h = \frac{1}{sJ_h}\left(\frac{T_t(\phi)}{G_r} - T_g\right) \tag{2.21}$$

While aerodynamic load torque, T_l, is an input, it is not one that can be controlled, which makes it a disturbance. There are ways to control wind torque input, through pitch angle control, for example, but this thesis is only focused on the magnetic gear dynamics and pole slip prevention/recovery. The only input we will assume we can directly measure, and control is the generator torque. Figure 2.2 gives a state-flow diagram of the dynamics described in (2.20) and (2.21), when damping is neglected. The flow diagram is rearranged to show the generator torque input to the magnetic gear and the disturbance torque, T_l from the wind.

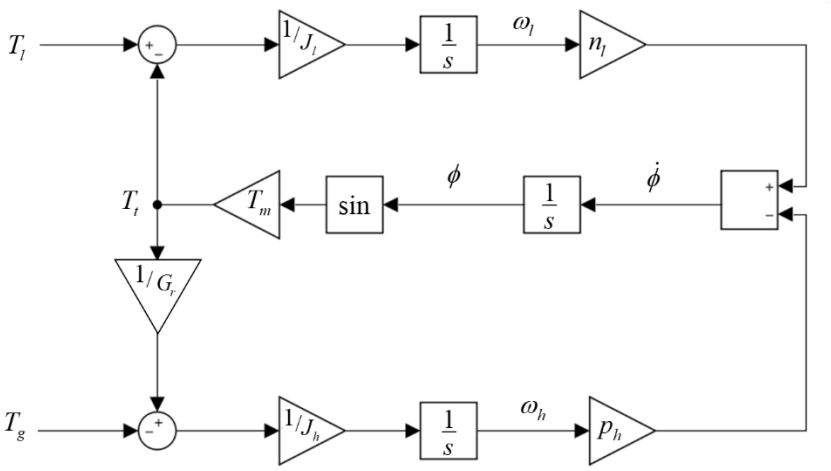

Figure 2.2. State flow diagram of (2.18) and (2.19), where damping is neglected

Table 2.1 gives a summary of the parameters for the Halbach magnetic gear and laboratory setup that will be used in the dynamic modeling. The inertia values presented are lumped parameters, where J_l is the combined inertia of the LSR and DC motor; and

J_h is the combined inertia of the HSR and PM generator. The lumped inertia of the HSR given in Table 2.1 is taken from the prototype design [25], further broken out in Table 2.2. The lumped inertia of the LSR is calculated using the following steps. If we first note that

$$\dot{\omega}_h = G_r \dot{\omega}_l \tag{2.22}$$

we can rearrange (2.19) so that

$$J_h G_r \dot{\omega}_h = T_t(\phi) - T_g G_r \tag{2.23}$$

Then substituting (2.22) into (2.23) gives

$$J_h G_r^2 \dot{\omega}_l = T_t(\phi) - T_g G_r \tag{2.24}$$

In steady state,

$$\dot{\omega}_h = 0 \tag{2.25}$$

and

$$\dot{\omega}_l = 0 \tag{2.26}$$

which means that, in steady state, substituting (2.25) and (2.26) into (2.18) and (2.19) yields

$$T_t(\phi) = T_l \tag{2.27}$$

$$T_t(\phi) = T_g G_r \tag{2.28}$$

which makes it easy to see that

$$T_g = \frac{T_l}{G_r} \tag{2.29}$$

Now, substituting (2.29) into (2.24) gives

$$J_h G_r^2 \dot{\omega}_l = T_t(\phi) - T_l \tag{2.30}$$

and substituting (2.30) into (2.18) gives

$$-J_l \dot{\omega}_l = J_h G_r^2 \dot{\omega}_l \tag{2.31}$$

From here, we can cancel $\dot{\omega}_l$ from both sides, giving us the following expression for LSR inertia in terms of HSR inertia

$$-J_l = J_h G_r^2 \tag{2.32}$$

Table 2.1. Summary of Magnetic Gear Parameters [25]

Parameter	Value	Units	Source
T_m	147.8	N·m	Measured
G_r	5.67	-	Design
p_h	3	-	Design
n_l	17	-	Design
J_h	2.9×10^{-2}	kg·m^2	Design (Table 2.2)
J_l	93.1×10^{-2}	kg·m^2	(2.32)

Table 2.2. Inertia data

Parameter	Value	Units	Description
J_{HSR}	1.88×10^{-3}	kg·m^2	HSR assembly
J_{PM}	27.3×10^{-3}	kg·m^2	Rexroth MSK100C PM generator, attached to the HSR

If damping is neglected, (2.13), (2.18), and (2.19) describe the dynamics of the non-linear system. As $T_t(\phi) = T_m \sin[\phi(t)]$ is the only non-linear term we can linearize around $(\phi_0, \omega_{h0}, \omega_{l0})$, which gives

$$T_t(\phi) \approx T_t(\phi_0) + (\phi - \phi_o)\left[\frac{\partial}{\partial \phi} T_t(\phi)\right]_{(\phi_0, \omega_{h0}, \omega_{l0})} \tag{2.33}$$

Evaluating

$$T_t(\phi) \approx T_m \sin(\phi_0) + (\phi - \phi_0) T_m \cos(\phi_0) \tag{2.34}$$

and substituting (2.34) into (2.18) gives

$$\dot{\omega}_l = \frac{T_l}{J_l} - \frac{T_m}{J_l}[\sin(\phi_0) + (\phi - \phi_0)\cos(\phi_0)] \tag{2.35}$$

expanding (2.35) gives

$$\dot{\omega}_l = \frac{T_l}{J_l} - \frac{T_m}{J_l}\cos(\phi_0)\phi - \frac{T_m}{J_l}\sin(\phi_0) + \frac{T_m}{J_l}\cos(\phi_0)\phi_0 \tag{2.36}$$

Substituting (2.34) into (2.19) gives

$$\dot{\omega}_h = \frac{T_m}{J_h G_r}[\sin(\phi_0) + \cos(\phi_0)(\phi - \phi_0)] - \frac{T_g}{J_h} \tag{2.37}$$

expanding (2.37) gives

$$\dot{\omega}_h = \frac{T_m}{J_h G_r}\cos(\phi_0)\phi - \frac{T_g}{J_h} + \frac{T_m}{J_h G_r}\sin(\phi_0) - \frac{T_m}{J_h G_r}\cos(\phi_0)\phi_0 \tag{2.38}$$

The last two terms in (2.36) and (2.38) are related to the initial condition torque values. Equation (2.13) is not non-linear, but the initial condition must still be accounted for

$$\dot{\phi} = n_l(\omega_l - \omega_{l0}) - p_h(\omega_h - \omega_{h0}) \tag{2.39}$$

Now, if we define the equivalent stiffness of the magnetic torque transferred at the load angle linearization point as

$$K_m = T_m(\cos(\phi_0)) \tag{2.40}$$

and substitute into (2.36), (2.38) and (2.39), then in state space matrix form, these equations are

$$\begin{bmatrix} \dot{\omega}_h \\ \dot{\omega}_l \\ \dot{\phi} \end{bmatrix} = \begin{bmatrix} 0 & 0 & \dfrac{K_{\mathrm{m}}}{J_h G_r} \\ 0 & 0 & \dfrac{-K_{\mathrm{m}}}{J_l} \\ -p_h & n_l & 0 \end{bmatrix} \begin{bmatrix} \omega_h \\ \omega_l \\ \phi \end{bmatrix} + \begin{bmatrix} \dfrac{-1}{J_h} \\ 0 \\ 0 \end{bmatrix} T_g + \begin{bmatrix} 0 \\ \dfrac{1}{J_l} \\ 0 \end{bmatrix} T_l$$
$$- \begin{bmatrix} 0 & 0 & \dfrac{K_{\mathrm{m}}}{J_h G_r} \\ 0 & 0 & \dfrac{-K_{\mathrm{m}}}{J_l} \\ -p_h & n_l & 0 \end{bmatrix} \begin{bmatrix} \omega_{h0} \\ \omega_{l0} \\ \phi_0 \end{bmatrix} - \begin{bmatrix} \dfrac{-1}{J_h} & 0 \\ 0 & \dfrac{1}{J_l} \\ 0 & 0 \end{bmatrix} \begin{bmatrix} \dfrac{T_m}{G_r}\sin(\phi_0) \\ T_m \sin(\phi_0) \end{bmatrix} \tag{2.41}$$

From (2.41) it can be seen that, at the linearized operating point (at steady state) the magnetic torque is

$$T_{t0} = T_m \sin(\phi_0) \tag{2.42}$$

and referred to the high-speed rotor side:

$$T_{th0} = \frac{T_{t0}}{G_r}. \tag{2.43}$$

From (2.42) we can define the following expression for steady state load angle

$$\phi_0 = \sin^{-1}(\frac{T_{t0}}{T_m}) \tag{2.44}$$

The matrices on the second line of (2.41) account for the linearization around the operating point $(\phi_0, \omega_{h0}, \omega_{l0})$ that do not have to be (0,0,0) at the initial simulation condition. This is a good starting point for designing a linear controller, but care must be taken when applying it to the non-linear magnetic gear system.

As we saw in Figure 1.4, there is a range of load angles where the transmitted torque is linear. In this region, control laws based on linearized dynamics can work, but a few things must be considered. The steady state load angle, ϕ_0, around which the dynamics are linearized must match the load angle at which the system is operating. Linearization is only accurate at the point it is linearized and a small deviation around it. How large that deviation can be and still provide a good approximation depends on how stiff the coupling is. If the magnetic gear is operating in the linear region and there is a significant load increase, the controller will not be responding accurately to the system if the load angle, ϕ_0, is not updated in real time. Figure 2.3 shows an updated state-flow diagram for the linearized magnetic gear dynamics given by (2.34).

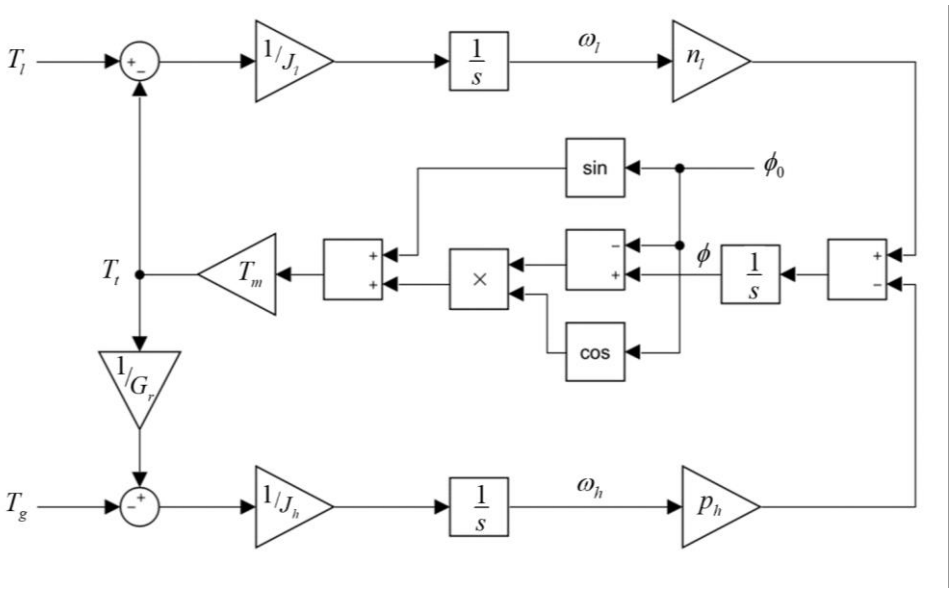

Figure 2.3 State flow diagram for linearized magnetic gear dynamics

2.4 Transfer Function Development

Using the model that is linearized around ϕ_0, we can solve for the HSR speed as a function of generator torque (input transfer function), and the response for HSR speed as a function of load torque (load transfer function), by first taking the Laplace transforms of (2.36), (2.38) and (2.39). In this section, $\omega_l, \omega_h, \phi, T_l$ and T_g are all functions of *s*, though for notation purposes it is not explicitly stated. If we assume initial conditions are $(\phi_0, \omega_{h0}, \omega_{l0})$, the Laplace transforms are

$$s\omega_l - \omega_{l0} = \frac{T_l}{J_l} - \frac{K_m}{J_l}(\phi - \phi_0) - \frac{T_m}{J_l}\sin(\phi_0) \tag{2.45}$$

$$s\omega_h - \omega_{h0} = \frac{K_m}{J_h G_r}(\phi - \phi_0) - \frac{T_g}{J_h} + \frac{T_m}{J_h G_r}\sin(\phi_0) \tag{2.46}$$

$$s\phi - \phi_0 = n_l(\omega_l - \omega_{l0}) - p_h(\omega_h - \omega_{h0}) \tag{2.47}$$

Solving (2.47) for ϕ gives

$$\phi = \frac{n_l(\omega_l - \omega_{l0}) - p_h(\omega_h - \omega_{h0})}{s} + \frac{\phi_0}{s}. \tag{2.48}$$

If we substitute (2.42) into (2.45) and (2.46) then we can write

$$s\omega_l - \omega_{l0} = \frac{T_l}{J_l} - \frac{K_m}{J_l}(\phi - \phi_0) - \frac{T_{t0}}{J_l} \tag{2.49}$$

$$s\omega_h - \omega_{h0} = \frac{K_m}{J_h G_r}(\phi - \phi_0) - \frac{T_g}{J_h} + \frac{T_{t0}}{J_h G_r}. \tag{2.50}$$

Substituting (2.48) into (2.49) and (2.50) gives

$$s\omega_l - \omega_{l0} = \frac{T_l}{J_l} - \frac{K_m}{J_l}\frac{n_l(\omega_l - \omega_{l0}) - p_h(\omega_h - \omega_{h0})}{s} - \frac{K_m}{J_l}(\frac{\phi_0 - s\phi_0}{s}) - \frac{T_{t0}}{J_l} \tag{2.51}$$

$$s\omega_h - \omega_{h0} = \frac{K_m}{J_h G_r}\frac{n_l(\omega_l - \omega_{l0}) - p_h(\omega_h - \omega_{h0})}{s} + \frac{K_m}{J_h G_r}(\frac{\phi_0 - s\phi_0}{s}) - \frac{T_g}{J_h} + \frac{T_{t0}}{J_h G_r} \tag{2.52}$$

From here we can solve (2.51) for ω_l

$$\omega_l = \frac{sT_l + K_m p_h \omega_h + (sJ_l + K_m n_l)\omega_{l0} - K_m(p_h\omega_{h0} + (\phi_0 - s\phi_0)) - sT_{t0}}{s^2 J_l + K_m n_l} \tag{2.53}$$

which can also be written as

$$\omega_l = (\frac{sT_l + K_m p_h}{s^2 J_l + K_m n_l})\omega_h + \frac{(sJ_l + K_m n_l)\omega_{l0} - K_m(p_h\omega_{h0} + (\phi_0 - s\phi_0)) - sT_{t0}}{s^2 J_l + K_m n_l} \tag{2.54}$$

Now, taking the Laplace transform of (2.15) and substituting into (2.54) simplifies the expression for ω_l further

$$\omega_l = (\frac{sT_l + K_m p_h}{s^2 J_l + K_m n_l})\omega_h + \frac{sJ_l\omega_{l0} + s(K_m\phi_0 - T_{t0})}{s^2 J_l + K_m n_l}. \tag{2.55}$$

The first term in (2.55) is known as the zero-state response. The second term is known as the zero-input response [29]. Likewise, we can solve (2.52) for ω_h and rearrange to form the zero-state and zero-input equations for the HSR speed

$$\omega_h = \frac{K_m n_l \omega_l - sG_r T_g}{s^2 J_h G_r + K_m p_h} + \frac{s(T_{t0} + J_h G_r \omega_{h0}) - sK_m \phi_0}{s^2 J_h G_r + K_m p_h} \tag{2.56}$$

From here we could cross substitute (2.55) and (2.56) to express (2.55) only in terms of ω_l and (2.56) only in terms of ω_h. But to simplify the analysis in the frequency domain we will proceed from here assuming $(\phi_0, \omega_{h0}, \omega_{l0}) = 0$. This allows us to rewrite (2.45)-(2.47) as:

$$s\omega_l = \frac{T_l}{J_l} - \frac{K_m}{J_l}\phi \tag{2.57}$$

$$s\omega_h = \frac{K_m}{J_h G_r}\phi - \frac{T_g}{J_h} \tag{2.58}$$

$$s\phi = n_l \omega_l - p_h \omega_h \tag{2.59}$$

Substituting (2.59) into (2.57) and (2.58) gives

$$s\omega_l = \frac{T_l}{J_l} - \frac{K_m}{J_l} \cdot \frac{n_l \omega_l - p_h \omega_h}{s} \tag{2.60}$$

$$s\omega_h = \frac{K_m}{J_h G_r} \cdot \frac{n_l \omega_l - p_h \omega_h}{s} - \frac{T_g}{J_h} \tag{2.61}$$

From here we can solve (2.60) for ω_l

$$\omega_l = \frac{sT_l + K_m p_h \omega_h}{s^2 J_l + K_m n_l} \tag{2.62}$$

Then, setting $T_g = 0$ and substituting (2.62) into (2.61) gives

$$s\omega_h = \frac{-K_m p_h \omega_h}{sJ_h G_r} + \frac{K_m n_l}{sJ_h G_r} \cdot \frac{sT_l + K_m p_h \omega_h}{s^2 J_l + K_m n_l} - \frac{T_g}{J_h} \tag{2.63}$$

Grouping ω_h terms

$$\omega_h \left(\frac{s^2 J_h G_r (s^2 J_l + K_m n_l) + K_m p_h (s^2 J_l + K_m n_l) - K_m^2 n_l p_h}{sJ_h G_r (s^2 J_l + K_m n_l)}\right) = \frac{sT_l K_m n_l}{sJ_h G_r (s^2 J_l + K_m n_l)} \tag{2.64}$$

Simplifying

$$\omega_h = \frac{sT_l K_m n_l}{s^2 J_h G_r (s^2 J_l + K_m n_l) + K_m p_h (s^2 J_l + K_m n_l) - K_m n_l K_m p_h} \tag{2.65}$$

Simplifying further

$$\omega_h = \frac{sT_l K_m n_l}{s^2 J_h G_r (s^2 J_l + K_m n_l) + s^2 K_m p_h J_l} \tag{2.66}$$

From here, we can see a pole-zero cancellation and the load transfer function is

$$H_{load}\big|_{T_g=0} \triangleq \frac{\omega_h}{T_l} = \frac{\frac{K_m n_l}{J_l}}{sJ_h G_r \left(s^2 + \frac{K_m n_l}{J_l} + \frac{K_m p_h}{G_r J_h}\right)} \tag{2.67}$$

this can be simplified further if we define [20]

$$\omega_a = \sqrt{\frac{K_m n_l}{J_l}} \tag{2.68}$$

$$\omega_r = \sqrt{\frac{K_m n_l}{J_l} + \frac{K_m p_h}{G_r J_h}} \tag{2.69}$$

then (2.67) becomes

$$H_{load}\big|_{T_g=0} \triangleq \frac{\omega_h}{T_l} = \frac{\omega_a^2}{sJ_hG_r(s^2+\omega_r^2)} \tag{2.70}$$

where ω_a and ω_r are the anti-resonant and resonant frequencies, respectively.

To solve for the input transfer function we set T_l=0, in (2.62) and substitute it into (2.61), which gives

$$s\omega_h = \frac{K_m n_l}{sJ_hG_r} \cdot \frac{K_m p_h \omega_h}{s^2 J_l + K_m n_l} - \frac{K_m p_h \omega_h}{sJ_hG_r} - \frac{T_g}{J_h} \tag{2.71}$$

Grouping ω_h terms

$$\omega_h \cdot \left(\frac{s^2 J_h G_r (s^2 J_l + K_m n_l) + K_m p_h (s^2 J_l + K_m n_l) - K_m n_l K_m p_h}{sJ_hG_r(s^2 J_l + K_m n_l)}\right) = -\frac{T_g}{J_h} \tag{2.72}$$

Simplifying

$$\omega_h = -\frac{T_g}{J_h} \cdot \frac{sJ_hG_r(s^2 J_l + K_m n_l)}{s^2 J_h G_r (s^2 J_l + K_m n_l) + K_m p_h (s^2 J_l + K_m n_l) - K_m n_l K_m p_h} \tag{2.73}$$

Canceling the common factors of s in the numerator and denominator as follows,

$$\frac{\omega_h}{T_g} = -\frac{G_r(s^2 J_l + K_m n_l)}{s(J_h G_r (s^2 J_l + K_m n_l) + K_m p_h J_l)} \tag{2.74}$$

is also referred to as a pole-zero cancellation. The input transfer function then simplifies to

$$H_{input}\big|_{T_l=0} \triangleq \frac{\omega_h}{T_g} = -\frac{(s^2 + \frac{K_m n_l}{J_l})}{sJ_h(s^2 + \frac{K_m n_l}{J_l} + \frac{K_m p_h}{J_h G_r})}. \tag{2.75}$$

This can be simplified further if we substitute (2.68) and (2.69) into (2.75)

$$H_{input}\Big|_{T_l=0} \triangleq \frac{\omega_h}{T_g} = \frac{s^2 + \omega_a^2}{sJ_h(s^2 + \omega_r^2)}. \qquad (2.76)$$

If $\phi_0 = 0^o$,

$$K_m = 147.8\ Nm/rad. \qquad (2.77)$$

Using this and the values from Table 2.1, (2.68) and (2.69) are

$$\begin{aligned} \omega_a &= 51.9\ rad/s \\ &= 495.6\ rpm \end{aligned} \qquad (2.78)$$

and

$$\begin{aligned} \omega_r &= 73.4\ rad/s \\ &= 701\ rpm \end{aligned} \qquad (2.79)$$

The bode plot for the input transfer function (2.76) is shown in Figure 2.4, which shows both the resonant and anti-resonant frequencies for $\phi_0 = 0^o$. The bode plot for the load transfer function, equation (2.70), is shown in Figure 2.5.

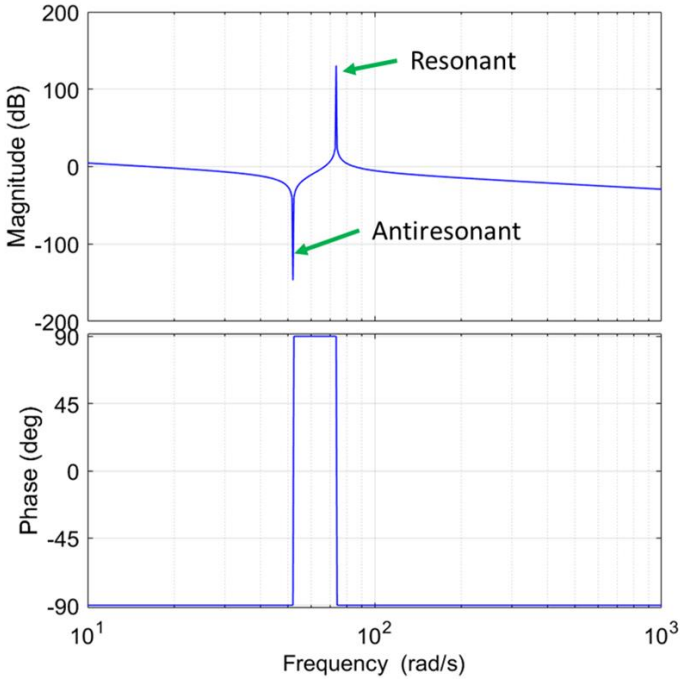

Figure 2.4. Bode plot for input transfer function (2.76) when $\phi_o = 0^o$

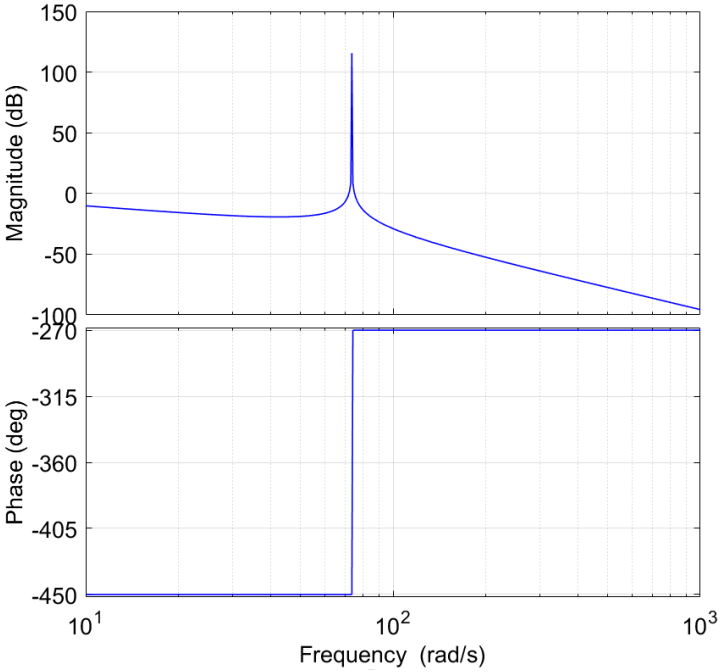

Figure 2.5. Bode plot for load transfer function, equation(2.70), when $\phi_o = 0^o$

The pole-zero plot for the input transfer function, when $\phi_0 = 0^o$ is shown in Figure 2.6; and for the load transfer function, Figure 2.7.

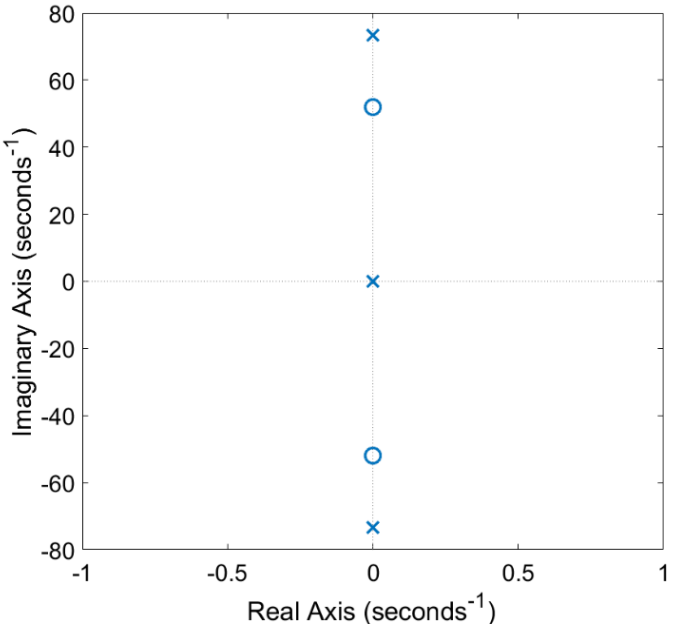

Figure 2.6. Pole-zero plot for input transfer function (2.76) when $\phi_o = 0^o$

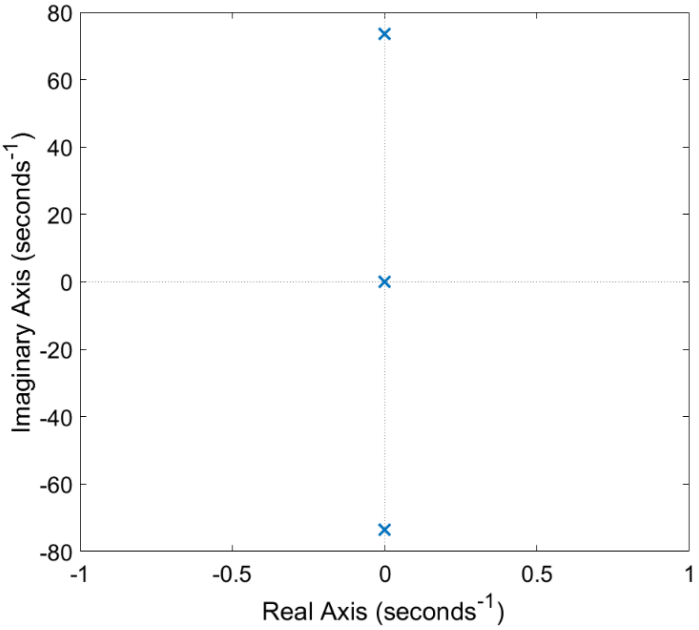

Figure 2.7. Pole-zero plot for load transfer function (2.70) when $\phi_o = 0^o$

The open loop poles from the pole-zero plots in Figure 2.6 and Figure 2.7 are

$$s = 0$$
$$s = 0 + 73.5i \qquad (2.80)$$
$$s = 0 - 73.5i$$

As K_m is a function of load angle, the anti and resonant frequencies shift with load angle. This is shown in Figure 2.8. The poles and zeros are also a function of load angle. Pole-zero plots for $0 \le \phi_0 \le 90^o$ are shown in Figure 2.9 and Figure 2.10, for the input and load transfer functions respectively.

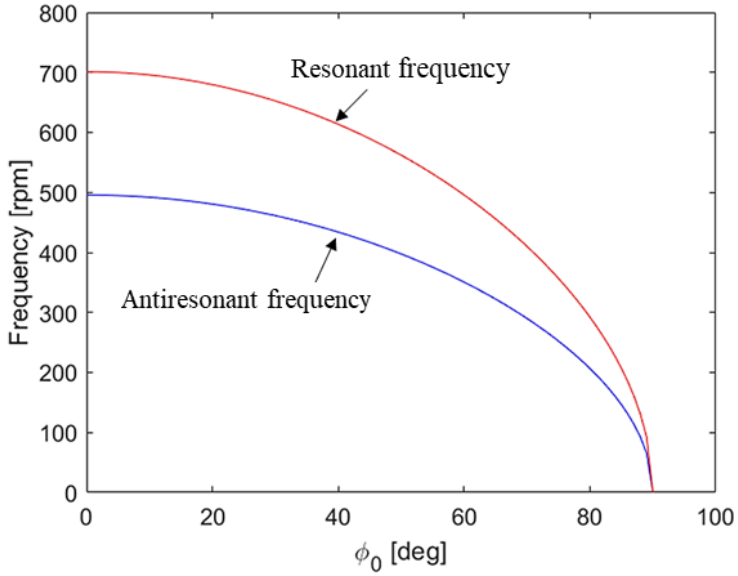

Figure 2.8. Antiresonant and resonant frequencies as a function of load angle

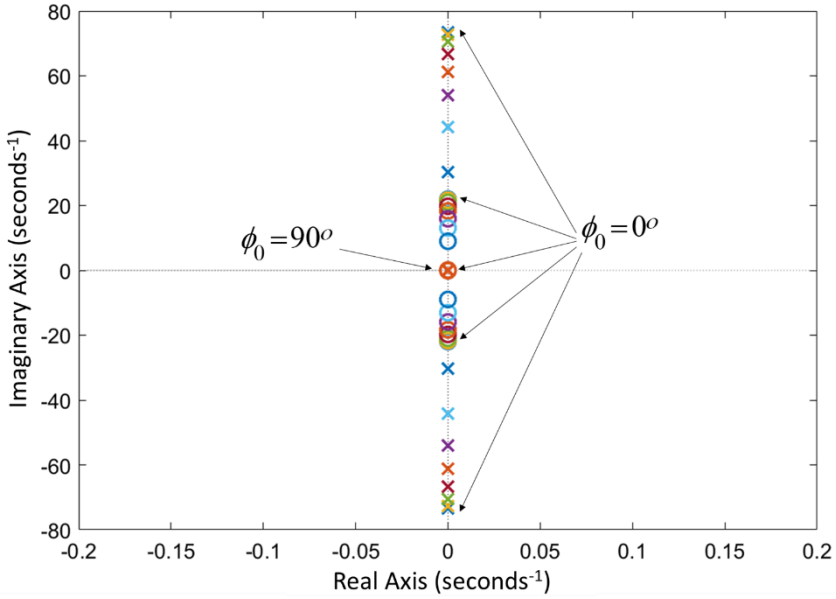

Figure 2.9. Pole-zero plot for input transfer function (2.76) as a function of load angle

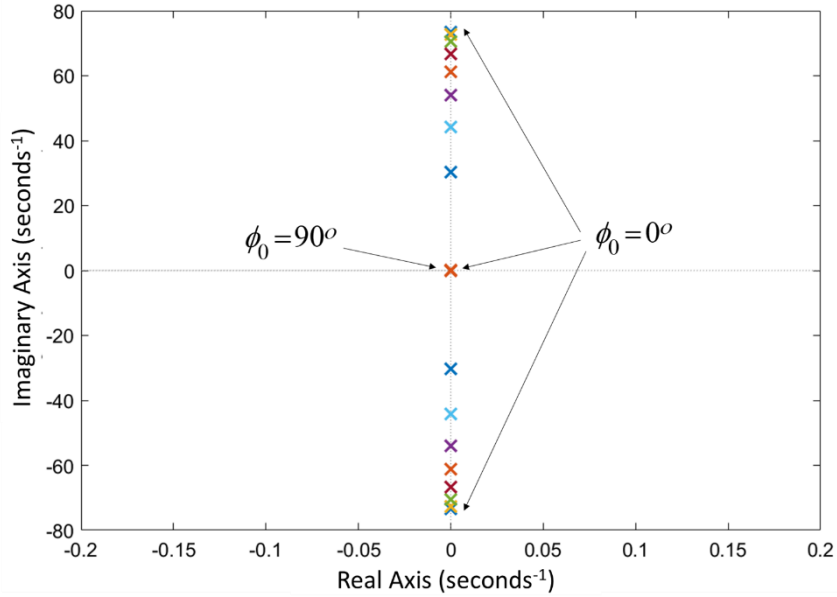

Figure 2.10. Pole-zero plot for load transfer function (2.70) as a function of load angle

In open loop, without any feedback control, the system is marginally stable, undamped, with all poles and zeros on the complex axis, including one oscillator pole at the origin.

As the load angle approaches the pullout angle of $\phi_0 = 90^o$ all the poles (and zeros in the case of the input transfer function) converge to the origin; and the dynamics become purely oscillatory. While the inclusion of damping terms would impact the pole-zero locations to a degree, it was deemed insignificant after the evaluation of the magnetic gear damping parameters presented in the next section.

2.5 Finite Element Modeling to Determine Damping Parameters

At the time this thesis was written, the damping parameters for the Halbach magnetic gear were not available. In order to justify the decision to exclude damping from the magnetic gear model used in this thesis, damping parameters were assessed, using finite element analysis (FEA) data available for a different coaxial magnetic gear produced in the laboratory. The parameters for the coaxial magnetic gear can be found in Table 2.3. In this design, the cage rotor is kept fixed, making the outer PM rotor the low speed rotor with $p_l = 40$ pole pairs. The inner PM rotor is the high-speed rotor, with $p_h = 6$ pole pairs. The gear ratio, $G_r = -p_l / p_h$ is negative because the outer and inner PM rotors spin in opposite directions.

Table 2.3. Magnetic Gear Parameters

Parameter	Value	Units
T_m	1702	N·m
G_r	-6.67	-
p_h	6	-
p_l	40	-
J_h	0.22	kg·m^2
J_l	0.51	kg·m^2

In order to evaluate the damping parameters for the inner and outer rotors, simulations using FEA were conducted in JMAG to produce data on power loss vs. rotor speed for each of the rotors. In one set of simulations, the inner rotor was kept fixed with the cage rotor and the outer rotor was rotated at varying electrical frequencies. The rotor was kept at each frequency until steady state power loss data was collected. The steady state power loss values were averaged at each frequency (f [Hz]) and plotted against rotor speed (ω [rad/s]), which was calculated from frequency using

$$\omega = \frac{40\pi f}{p} \tag{2.81}$$

where p is the number of pole pairs. The relationship between power loss and rotor speed can be given by

$$P = T\omega \quad [\text{Nm} \cdot \text{rad/s}] \tag{2.82}$$

noting that

$$T = B\omega \quad [Nm] \tag{2.83}$$

where B is the damping coefficient with units of $[\text{Nm} \cdot \text{s/rad}]$. Substituting (2.83) into (2.82); and solving for B gives

$$B = \frac{P}{\omega^2} \quad [\text{Nm} \cdot \text{s/rad}] \tag{2.84}$$

this shows us that we can solve for *B* by calculating the slope of a second-degree polynomial fit to the power loss vs. rotor speed curve. The same procedure was repeated for the inner rotor, holding the outer rotor fixed. The resulting damping parameters were

$$B_h = 0.577 \quad [\text{Nm} \cdot \text{s/rad}] \tag{2.85}$$

$$B_L = 0.0316 \quad [\text{Nm} \cdot \text{s/rad}]. \tag{2.86}$$

It is important to note that this method of approximating the damping coefficient is going to be less accurate if the polynomial that best fits the data has significant first degree and/or constant terms. In this case, those terms would be 3-5 orders of magnitude smaller, and could be considered negligible. Figure 2.11 - Figure 2.12 show plots of power loss as a function of outer rotor and inner rotor speed, respectively. Figure 2.13 - Figure 2.14 compare FEA and state space simulated outer rotor torque over shorter and

longer time intervals (when the outer rotor damping is 0.0316 [Nms/rad]. It is clear that the damping is negligible.

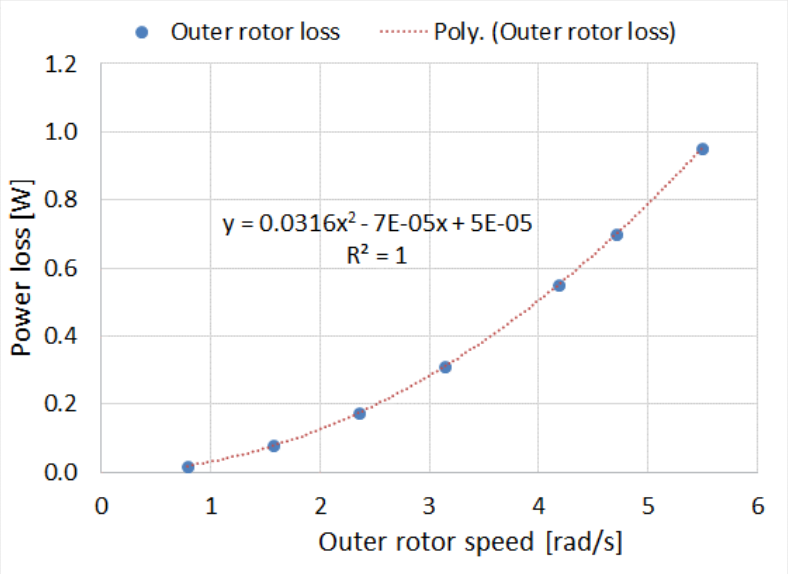

Figure 2.11. Outer rotor power loss as a function of rotor speed

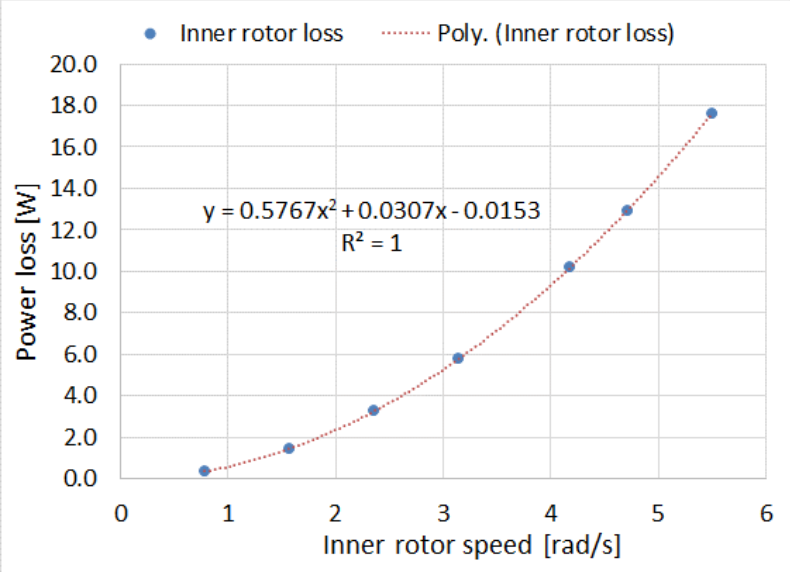

Figure 2.12. Inner rotor power loss as a function of rotor speed

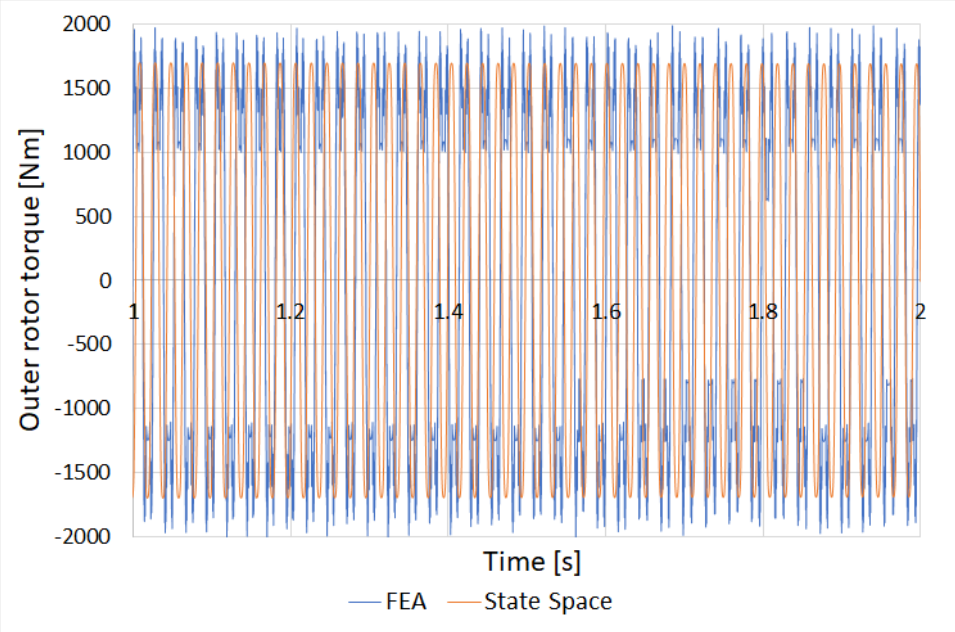

Figure 2.13. Outer rotor torque when B_L =0.0316 [Nms/rad], 1 s time interval

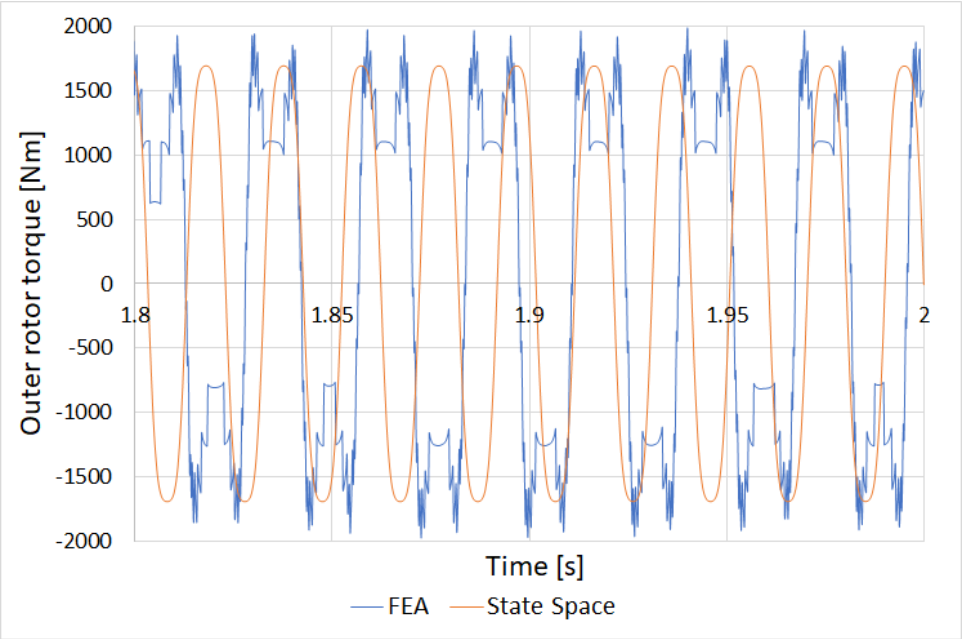

Figure 2.14. Outer rotor torque when B_L =0.0316 [Nms/rad], 0.2 s time interval

The full state space model, when $\phi_0 = 0^o$, is given by:

$$\begin{bmatrix} \dot{\omega}_h \\ \dot{\omega}_l \\ \dot{\phi} \end{bmatrix} = \begin{bmatrix} 0 & 0 & \dfrac{T_{\mathrm{m}} \cos[\phi_0]}{J_h G_r} \\ 0 & 0 & \dfrac{-T_{\mathrm{m}} \cos[\phi_0]}{J_l} \\ -p_h & n_l & 0 \end{bmatrix} \begin{bmatrix} \omega_h \\ \omega_l \\ \phi \end{bmatrix} + \begin{bmatrix} -\dfrac{1}{J_h} \\ 0 \\ 0 \end{bmatrix} T_g + \begin{bmatrix} 0 \\ \dfrac{1}{J_l} \\ 0 \end{bmatrix} T_l \quad (3.1)$$

which is a state equation of the form

$$\dot{\mathbf{x}} = \mathbf{A}\mathbf{x} + \mathbf{B}_\mathbf{u} u + \mathbf{B}_\mathbf{l} d_l \,. \quad (3.2)$$

It is assumed that only the HSR speed is the plant output, therefore the output, y, is given by

$$\mathbf{y} = \begin{bmatrix} 1 & 0 & 0 \end{bmatrix} \begin{bmatrix} \omega_h \\ \omega_l \\ \phi \end{bmatrix} \quad (3.3)$$

which is an output equation of the form

$$\mathbf{y} = \mathbf{C}\mathbf{x} \,. \quad (3.4)$$

We can then individually define our states

$$\mathbf{x} = \begin{bmatrix} \omega_h & \omega_l & \phi \end{bmatrix}^T \quad (3.5)$$

state matrix

$$\mathbf{A} = \begin{bmatrix} 0 & 0 & \dfrac{T_{\mathrm{m}} \cos[\phi_0]}{J_h G_r} \\ 0 & 0 & \dfrac{-T_{\mathrm{m}} \cos[\phi_0]}{J_l} \\ -p_h & n_l & 0 \end{bmatrix} \tag{3.6}$$

input matrix

$$\mathbf{B_u} = \begin{bmatrix} -\dfrac{1}{J_h} & 0 & 0 \end{bmatrix}^T \tag{3.7}$$

input

$$u = T_g \tag{3.8}$$

disturbance matrix

$$\mathbf{B}_l = \begin{bmatrix} 0 & \dfrac{1}{J_l} & 0 \end{bmatrix}^T \tag{3.9}$$

disturbance input

$$d_l = T_l \tag{3.10}$$

and output matrix

$$\mathbf{C} = \begin{bmatrix} 1 & 0 & 0 \end{bmatrix}. \tag{3.11}$$

The first step in designing state feedback control is evaluating whether the matrices we have selected for the controller are fully controllable by evaluating the rank of

$$\mathbf{C_o} = \begin{bmatrix} B & AB & A^2 B ... A^{n-1} B \end{bmatrix}. \tag{3.12}$$

Substituting (3.6)-(3.7) into (3.12) and evaluating using parameters from Table 2.1, the controllability matrix when the generator torque is the input is

$$\mathbf{C_o} = \begin{bmatrix} -34.5 & 0 & 9.3x10^4 \\ 0 & 0 & -1.64x10^4 \\ 0 & 103.4 & 0 \end{bmatrix} \tag{3.13}$$

By swapping rows, multiplying through by constants and adding rows in (3.13) together, the reduced row echelon form is

$$\mathbf{C_o} = \begin{bmatrix} 1 & 0 & 0 \\ 0 & 1 & 0 \\ 0 & 0 & 1 \end{bmatrix}. \tag{3.14}$$

This has a rank of 3, which is equal to the size of the **A** matrix. Therefore, the state space model as we have defined it is fully state controllable, at least when there is no load. When the load angle is at the peak pullout value of $\phi_0 = 90^o$, the controllability matrix, in reduced row echelon form is

$$\mathbf{C_o} = \begin{bmatrix} 1 & 0 & 0 \\ 0 & 1 & 0 \\ 0 & 0 & -1x10^{-12} \end{bmatrix}. \tag{3.15}$$

The bottom row is effectively zeros, which means the rank of the controllability matrix at the maximum load the magnetic gear can handle is 2. This is less than the size of the **A** matrix, which means the system is no longer fully state controllable. For scenarios where the system is fully state controllable, the following state feedback control development was guided by examples from [30]. The control law for full state feedback control is

$$\mathbf{u} = \mathbf{-Kx} \tag{3.16}$$

where **K** is a vector of gains for each state in the state space model

$$\mathbf{u} = -\begin{bmatrix} K_{\omega h} & K_{\omega l} & K_{\phi} \end{bmatrix} \cdot \begin{bmatrix} \omega_h \\ \omega_l \\ \phi \end{bmatrix}. \tag{3.17}$$

Substituting (3.16) into (3.2) gives

$$\dot{\mathbf{x}} = \mathbf{A}\mathbf{x} - \mathbf{B_u}\mathbf{K}\mathbf{x} + \mathbf{B_l} d_l . \tag{3.18}$$

Combining terms gives the state equation with full state feedback

$$\dot{\mathbf{x}} = (\mathbf{A} - \mathbf{B_u}\mathbf{K})\mathbf{x} + \mathbf{B_l} d_l . \tag{3.19}$$

The state flow diagram for the magnetic gear state space model defined in (3.4) and (3.19) with full state feedback control is given in Figure 3.1. An alternative presentation of the state flow detailing the signals and routing is in Figure 3.2.

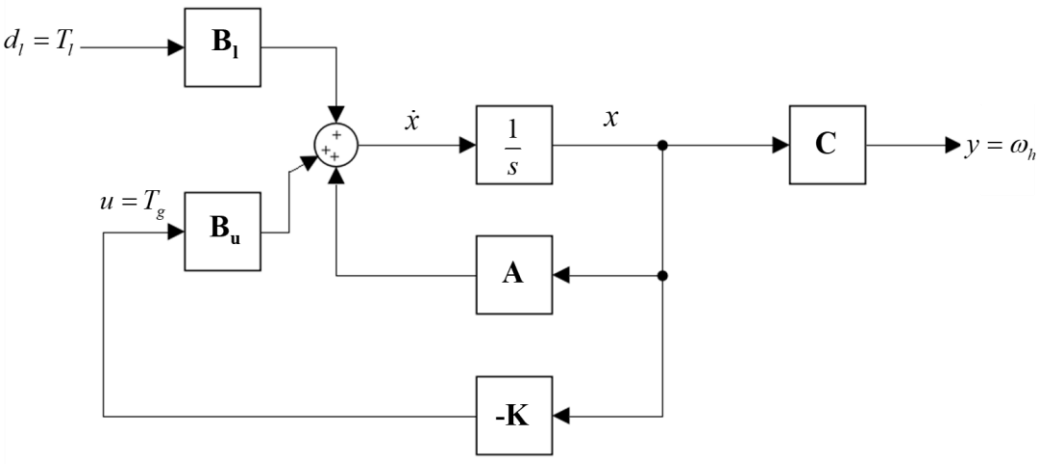

Figure 3.1. Full state feedback control block diagram

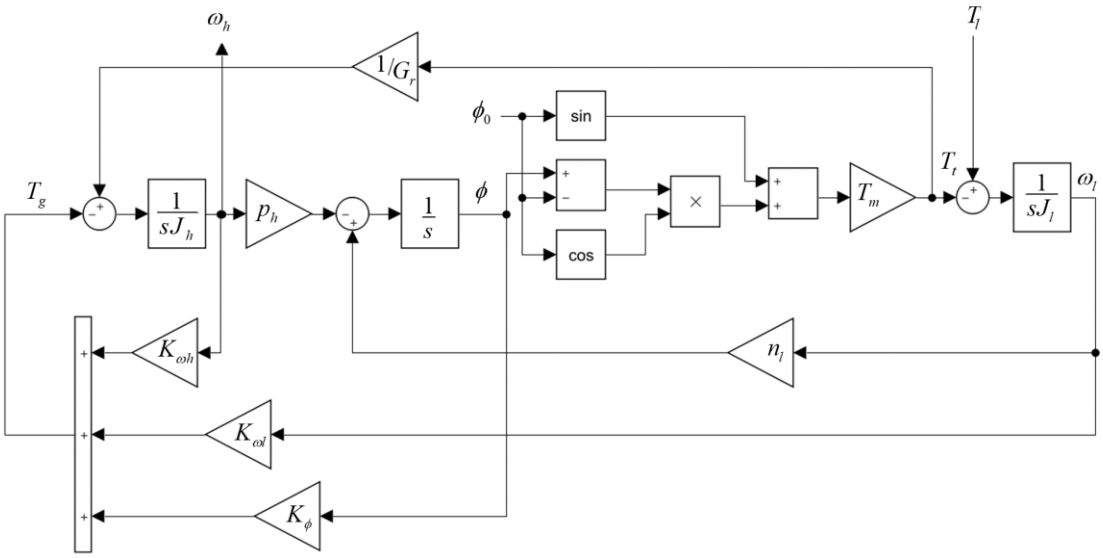

Figure 3.2. Full state feedback control, linearized dynamics

The closed loop state matrix is

$$\left\lfloor \mathbf{A}-\mathbf{B_u}\mathbf{K} \right\rfloor = \begin{bmatrix} \frac{K_{\omega h}}{J_h} & \frac{K_{\omega l}}{J_h} & \frac{K_\phi}{J_h}+\frac{K_m}{G_r J_h} \\ 0 & 0 & \frac{-K_m}{J_l} \\ -p_h & n_l & 0 \end{bmatrix}. \qquad (3.20)$$

The closed loop poles are the roots of the characteristic polynomial for the closed-loop system given by

$$\Delta_{CL} = \left| s\mathbf{I} - (\mathbf{A}-\mathbf{B_u}\mathbf{K}) \right|. \qquad (3.21)$$

Solving (3.21) using Matlab, the characteristic polynomial is

$$\Delta_{cl} = s^3 - \frac{K_{\omega h}}{J_h}s^2 + (\frac{K_m p_h}{G_r J_h} + \frac{K_m n_l}{J_l} + \frac{K_\phi p_h}{J_h})s - (\frac{K_m K_{\omega h} n_l}{J_l J_h} + \frac{K_m K_{\omega l} p_h}{J_l J_h}). \qquad (3.22)$$

Typically, poles are selected based on the desired closed-loop system performance. The ideal poles can be multiplied to produce a polynomial equation that is compared to the characteristic polynomial (3.22) [6]. From there it may be straightforward to see what the individual state feedback gain terms need to be in order to have the polynomials match. If it is not straightforward, *place* or *acker* commands can be used in Matlab to generate the gains needed to achieve the desired closed loop poles.

3.1 Pole Placement Design

For this closed-loop system, initially a second order dominant pole approximation [12] will be used to determine pole placement. With this method, ideal pole locations for a third order system are selected such that the characteristic equation factors into one real pole, and two complex poles. The real pole is chosen far enough to the left of the complex poles in the pole-zero plane that the dominant complex poles determine the system response. The zero must also be moved far enough to the left of the complex poles so that it does not affect system performance. A common criteria [12] for selecting a dominant complex pole pair is the following

$$s_{1,2} = -\zeta\omega_r \pm j\omega_r\sqrt{1-\zeta^2} \tag{3.23}$$

where ζ is the desired damping ratio and ω_r is the resonant or natural frequency. Where peak overshoot, *OS*, is related to damping by

$$OS = e^{-\pi\zeta/\sqrt{1-\zeta^2}}. \tag{3.24}$$

Ideally, we would like our overshoot to be 0, but a balance must be struck between acceptable overshoot and acceptable control action, among other things. The pole placement design approach often requires some trial and error. If we select a damping ratio of 0.6 and substitute (2.79) into (3.23) our dominant poles are

$$s_{1,2} = -44 \pm 58.72i\,. \tag{3.25}$$

When we look at setting the real pole further to the left, we are comparing it to the real part of the complex pole. If we select the real pole to be roughly twice the value of the real part of the complex poles we get

$$s_3 = -88. \tag{3.26}$$

If we place those gains using the Matlab 'place' command as follows

$$\begin{aligned} &\text{P=[-88 \quad -44+58.7i \quad -44-58.7i]} \\ &\text{K=}\textit{place}\text{[A,B}_\text{u}\text{,P]} \end{aligned} \tag{3.27}$$

with $\phi_0 = 0$, this gives

$$\begin{aligned} K_{\omega h} &= -5 \\ K_{\omega l} &= 0.08 \\ K_{\phi} &= 75 \end{aligned} \tag{3.28}$$

Pole-zero plots using the gains in (3.28), with $\phi_0 = 0^o$, is shown in Figure 3.3 andFigure 3.4. In Figure 3.3, we can see that the closed-loop zero is orders of magnitude farther to the left of the closed-loop poles, indicating it should not have an impact on the dynamics. In Figure 3.4 we can see that the poles are placed where we wanted them. To see how the poles shift within the range of operating load angle, a pole-zero plot was created (Figure 3.5 and Figure 3.6) where the load angle was swept over the interval

$0 \le \phi_0 \le 90^o$ for the linear model. Figure 3.6 shows that as the load angle increases from 0 to roughly $64-65^o$ (132-134 Nm of load torque (2.8)), the complex poles are dominant but decreasingly so. In this range, the real pole and complex poles move toward each other, the real pole has increasing influence over the complex and damping increases. After 65^o, the real pole becomes dominant and the complex poles move further to the left. As we saw with the open-loop poles, as the load angle approaches the pullout value of $\phi_0 = 90^o$ the real pole converges to the origin. Approaching this angle, we would expect to see more oscillatory behavior before the system becomes unstable.

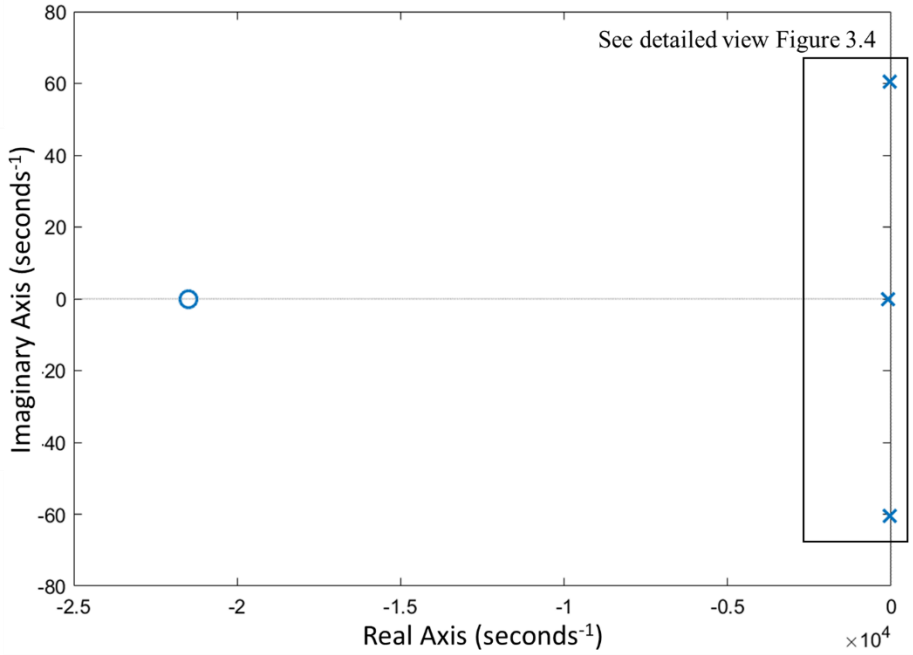

Figure 3.3. Pole-zero plot for (3.25)-(3.26), when $\phi_o = 0^o$.

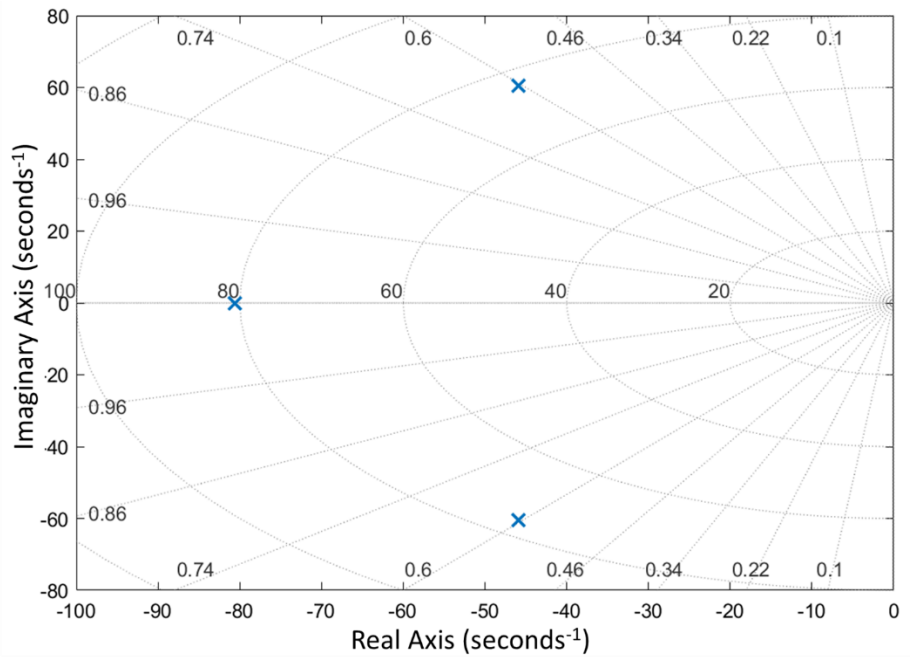

Figure 3.4. Pole-zero plot for (3.25)-(3.26), when $\phi_o = 0^\circ$, detailed view.

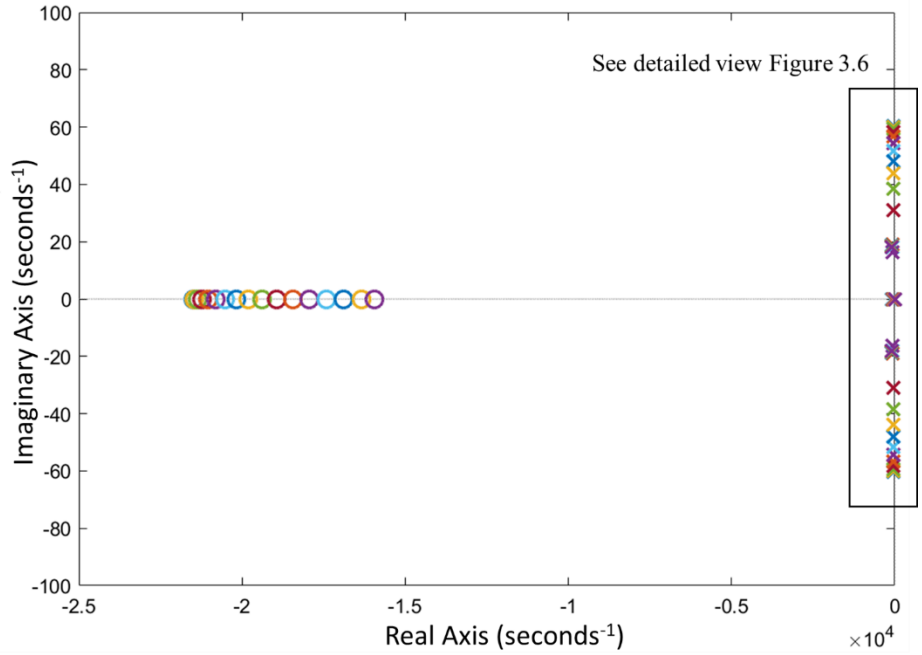

Figure 3.5. Pole-zero plot for (3.25)-(3.26) with load angle sweep.

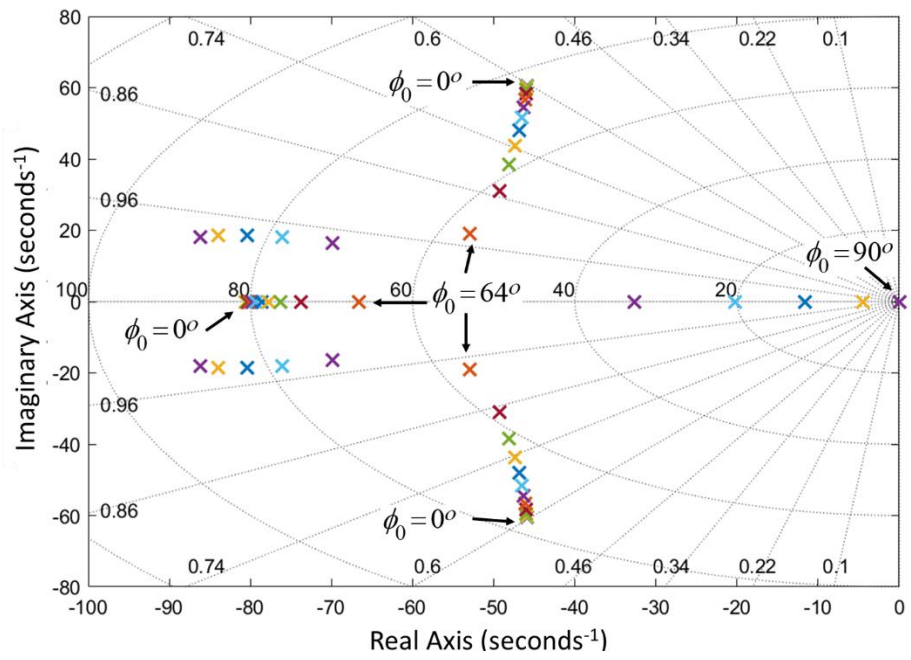

Figure 3.6. Pole-zero plot for (3.25)-(3.26) with load angle sweep, detailed view.

Using the linearized dynamic Simulink model shown in Figure 3.2, a simulation was performed using a starting load torque of 0 Nm with a 10 Nm step increase at t = 1.5 s. The results can be seen in Figure 3.7 (a)-(d). A second simulation was performed using a starting load torque of 140 Nm with a 5 Nm step increase at t = 1.5 s. The results from the second simulation are shown in Figure 3.8 (a)-(d). Comparing the results of both simulations, the overshoot decreases as the load torque approaches the pullout torque of $T_m = 147.8$ Nm. This is a result of the real system pole becoming more dominant than the complex conjugate poles, as we saw in Figure 3.6. These results are useful for verifying the pole placement design, for providing a starting point to discuss how accurate linearization can be when the real system is nonlinear, and for determining what the boundaries of that accuracy might be.

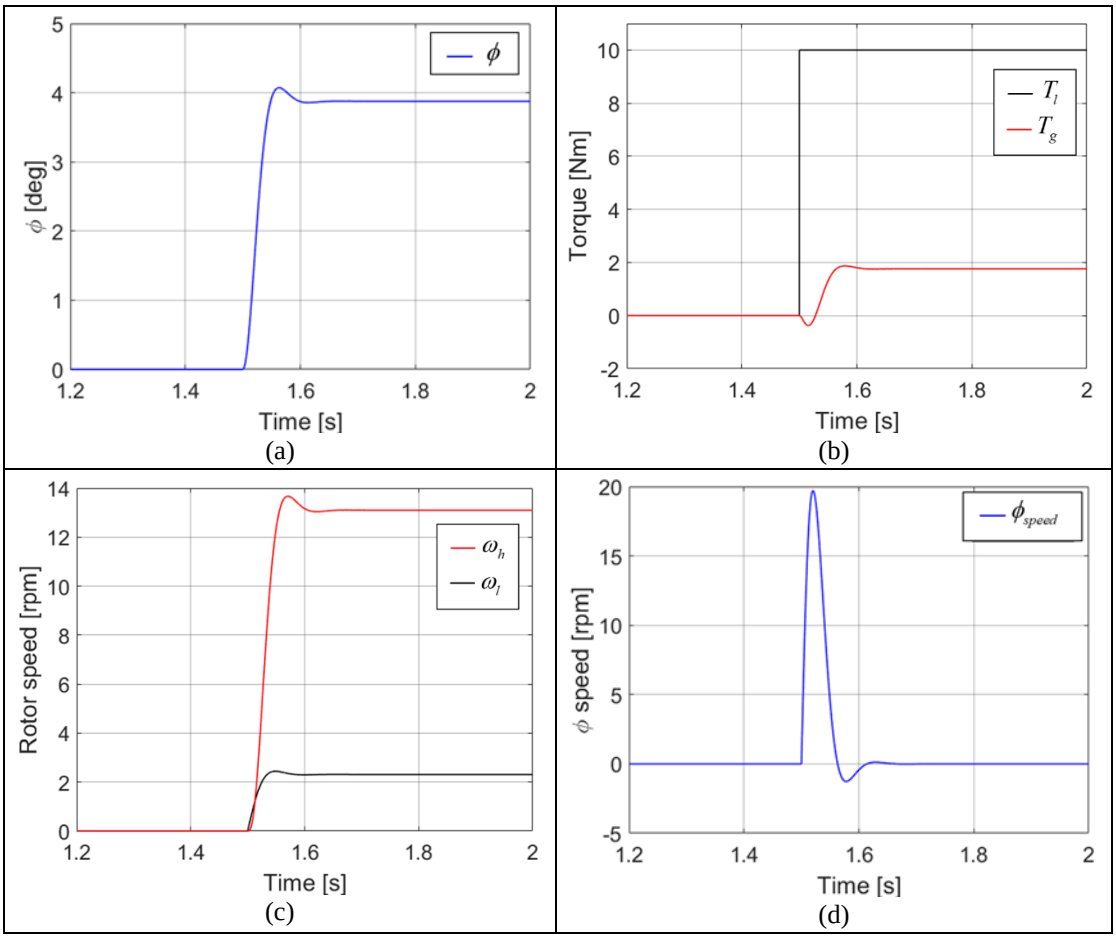

Figure 3.7. Transient plot showing linear system states - load angle (a), torque (b), rotor speeds (c), load speed (d) - following a step change in load torque, T_l, from 0-10 Nm at t = 1.5s.

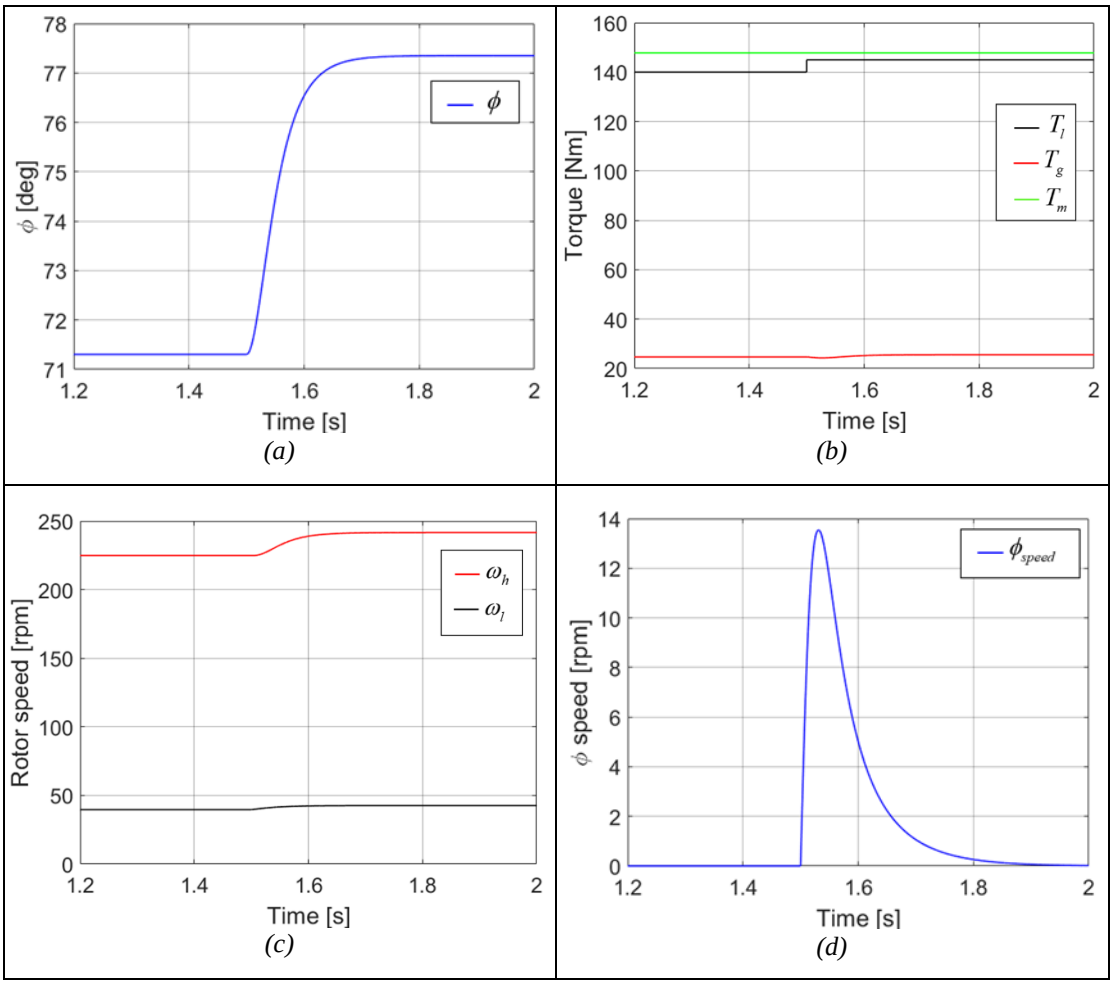

Figure 3.8. Transient plot showing linear system states - load angle (a), torque (b), rotor speeds (c), load speed (d) - following a step change in load torque, T_l, from 140-145 Nm at t = 1.5s.

One of the most useful outcomes from the pole placement design was the observation that the real pole becomes more dominant as the load angle increases, completely damping the overshoot as the load angle approaches the pullout value. If there is no load angle overshoot, it may be possible to transmit up to the maximum rated torque through the gear. We have verified that this works when the system is linearized. Now we need to compare these results to the non-linear system, to see whether the load angle overshoot is damped when the system is non-linear. The simulation that produced

the results in Figure 3.8 ($T_l = 140 - 145$ Nm at t = 1.5s) was repeated for the non-linear system shown in Figure 3.9. The starting load angle for both the linear and non-linear simulations was $\phi_0 = 71.3^o$. The linear and non-linear results are compared in Figure 3.10.

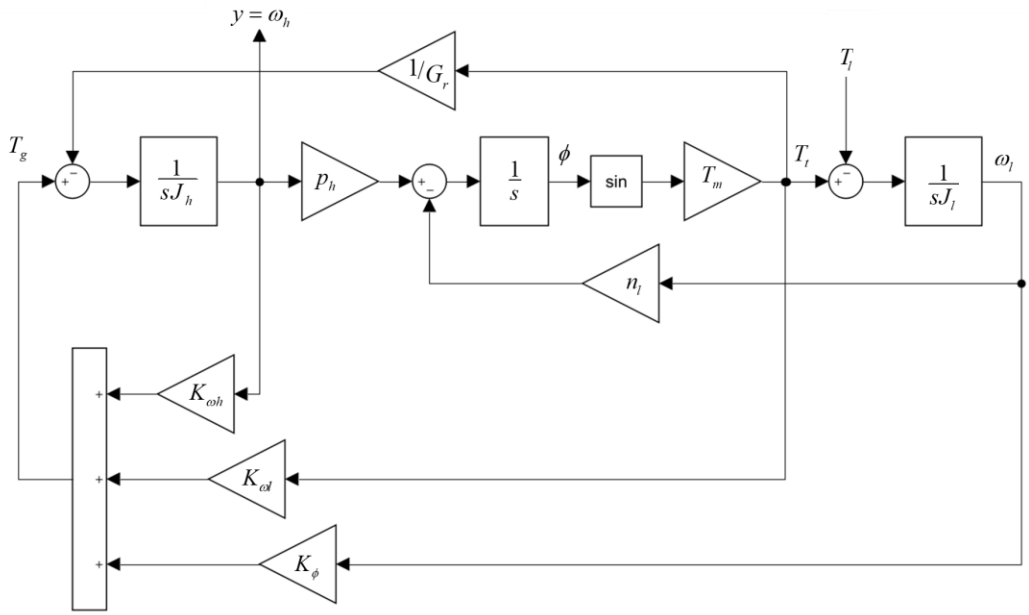

Figure 3.9. Full state feedback control, non-linear dynamics.

It is clear from the plots in Figure 3.10 that the overshoot is damped for both the linear and non-linear systems when the load torque is approaching the pullout value. What is also clear is that the settling time is faster for the transient linear states, and there is steady state error in the linear response to a 5 Nm step change in load torque. Both the linear and non-linear simulations started with the same steady state load angle and load torque values. A step change in load torque of $T_l = 5$ Nm was enough to cause an error in the linear estimate of the non-linear states. This is because the linear controller isn't being updated with a new linearization point when the load changes; and the magnetic

gear is operating in the non-linear region. The next section will take a closer look at the conditions in which a linear approximation of the system dynamics can be accurate when operation is in the non-linear region.

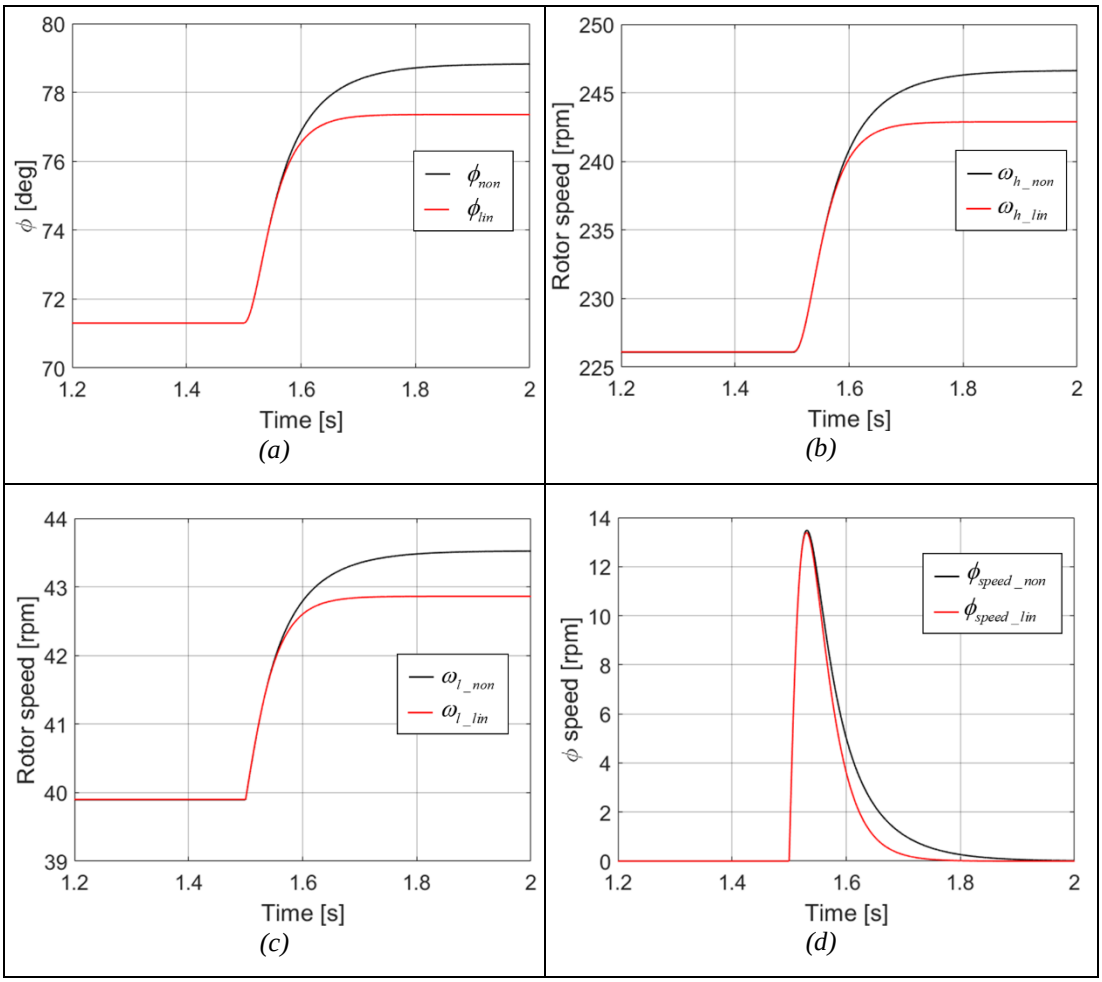

Figure 3.10. Transient plot comparing linear system states - load angle (a), high-speed rotor speed (b), low speed rotor speed (c), load speed (d) - following a step change in load torque, T_l, from 140-145 Nm at t = 1.5s.

3.2 Linear Control of Non-linear Dynamics

Before moving further in the design of a linear controller for the nonlinear magnetic gear it is good to look at how the accuracy changes with different amounts of load torque disturbance. Using (2.41) and the dynamic Simulink model shown in Figure 3.2, Figure 3.12 and Figure 3.13 show what happens to the load angle when it is linearized around a stable operating point and there is a step change in load torque of 5, 10, and 20 Nm, respectively. Figure 3.11 is a visualization of the load torque step profiles used for the simulations. In the actual simulations, the load torque was increased each increment (5, 10 or 20 Nm) from 60 Nm and allowed to reach steady state before being increased again. Final values from each simulation were extracted and used to create the plots in Figure 3.12 and Figure 3.13. These curves are compared to the non-linear load angle evolution, to show how accurately the linearized controller could estimate the non-linear dynamics if there were a step change and the load angle was not updated in the linearized controller.

It is clear from the plots that the closer the load angle gets to the pullout value of 90^o, the more a step increase of 5, 10 or 20 Nm causes error in the linearized load angle approximations. The linearization is fairly accurate, even with 20 Nm step changes, up to 130 Nm, or 88% of rated torque. If the load change is in 5-10 Nm increments, the linearization has minimal error up to 95% of rated torque. Any load torque changes

greater than 20 Nm will only make the load angle in the linear model less accurate following the increase. This is why it is important for a linear controller to dynamically update the load angle with load changes in the system.

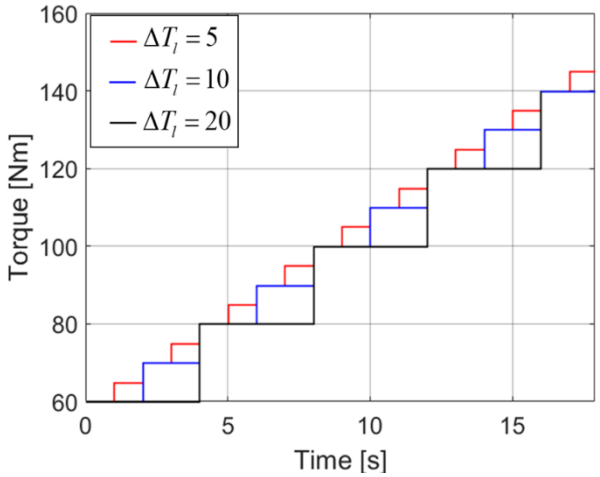

Figure 3.11. Step torque profiles for Figure 3.12 and Figure 3.13

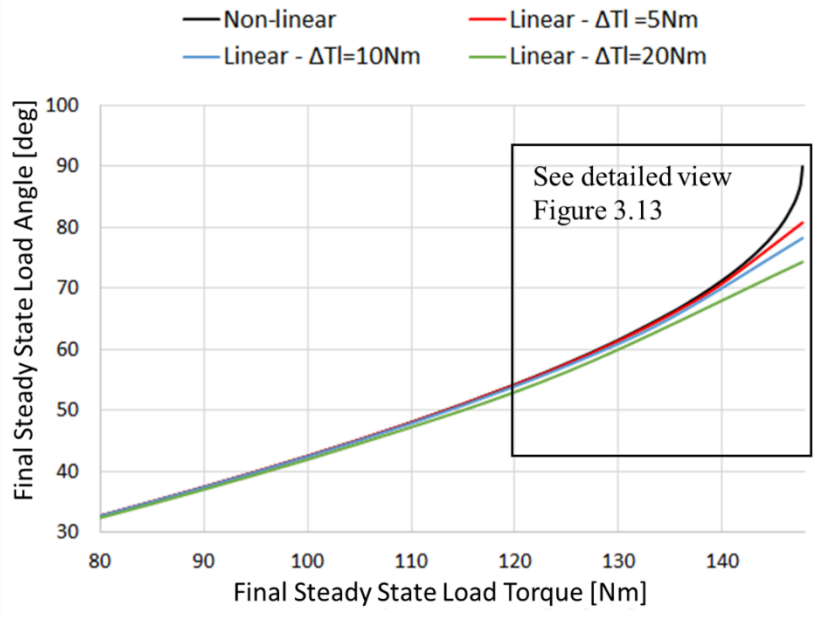

Figure 3.12. Linearized load angle responses to step changes in load torque

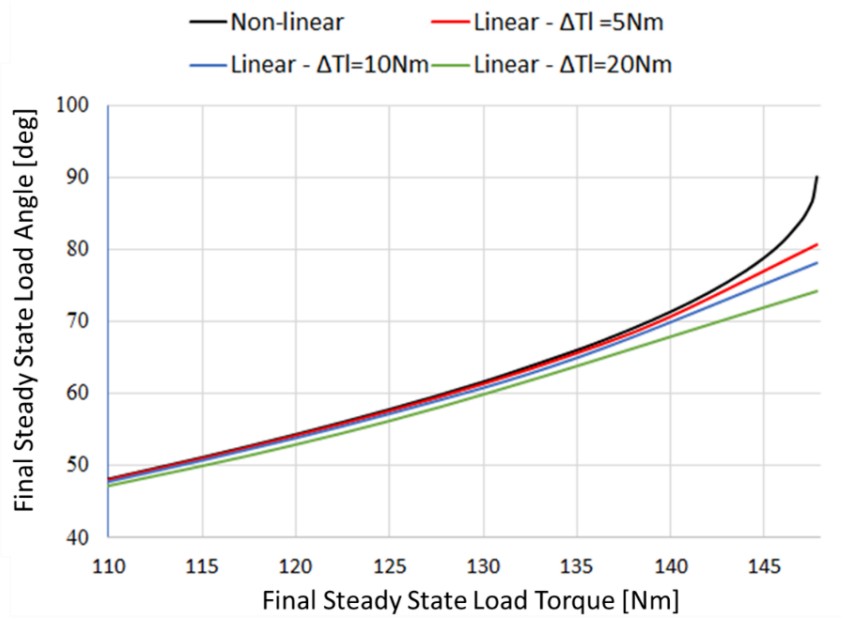

Figure 3.13. Linearized load angle responses to step changes in load torque, detailed view.

4 Full Order Observer – State Feedback Control

When designing state feedback controllers for physical systems it is important to keep in mind which states can be physically measured and which can be measured with the accuracy required. It may be too costly or physically impossible to accurately and/or reliably measure all of the states needed for feedback control [31]. In these situations, an observer is useful because it can provide accurate estimates of the states that cannot be directly measured. While state observers are discussed in most controls texts, the following explanation and development of the full order (FO) observer equations is based on information in [29-31].

The observed or estimated states are provided through a replica of the state space model of the system being controlled, which takes in the physical system inputs and outputs and replicates the state vector. The estimated state vector, denoted $\hat{\mathbf{x}}$, contains all the states that are in the system state vector. This is what makes the observer full order. The estimated state vector is scaled with the state feedback gain vector, **K**, defined in (3.28), to modify the input to the system

$$u = -\mathbf{K}\hat{\mathbf{x}} \tag{4.1}$$

Because this feedback structure utilizes estimated states to influence the physical input to a system there must be a way to ensure the estimates are accurate. This is achieved by comparing the outputs of the system, $\mathbf{y}$, and observer, $\hat{\mathbf{y}}$; and creating a feedback signal to the observer with gain

$$\mathbf{L}(\mathbf{y} - \hat{\mathbf{y}}) \tag{4.2}$$

The observer state equation can then be defined as

$$\dot{\hat{\mathbf{x}}} = \hat{\mathbf{A}}\hat{\mathbf{x}} + \hat{\mathbf{B}}_{\mathbf{u}}u + \mathbf{L}(\mathbf{y} - \hat{\mathbf{y}}) \tag{4.3}$$

where if we note

$$\hat{\mathbf{y}} = \hat{\mathbf{C}}\hat{\mathbf{x}} \tag{4.4}$$

Then substituting (3.4) and (4.4) into (4.3) yields

$$\dot{\hat{\mathbf{x}}} = \hat{\mathbf{A}}\hat{\mathbf{x}} + \hat{\mathbf{B}}_{\mathbf{u}}u + \mathbf{L}\hat{\mathbf{C}}(\mathbf{x} - \hat{\mathbf{x}}) \tag{4.5}$$

Where it is assumed that $\mathbf{C} = \hat{\mathbf{C}}$, $\mathbf{A} = \hat{\mathbf{A}}$, and $\mathbf{B}_{\mathbf{u}} = \hat{\mathbf{B}}_{\mathbf{u}}$, substituting (4.1) into (4.5) and grouping state vector terms gives

$$\dot{\hat{\mathbf{x}}} = (\mathbf{A} - \mathbf{LC})\hat{\mathbf{x}} - \mathbf{B}_{\mathbf{u}}\mathbf{K}\hat{\mathbf{x}} + \mathbf{LC}\mathbf{x} \tag{4.6}$$

this simplifies to

$$\dot{\hat{\mathbf{x}}} = (\mathbf{A} - \mathbf{LC} - \mathbf{B}_{\mathbf{u}}\mathbf{K})\hat{\mathbf{x}} + \mathbf{LC}\mathbf{x}\,. \tag{4.7}$$

If (4.1) replaces (3.16), in (3.19), the state feedback equation for the system becomes

$$\dot{\mathbf{x}} = \mathbf{A}\mathbf{x} - \mathbf{B}_{\mathbf{u}}\mathbf{K}\hat{\mathbf{x}} + \mathbf{B}_{\mathbf{l}}d_l \tag{4.8}$$

Combining (4.7) and (4.8), the state equation for combined system and observer states is

$$\begin{bmatrix} \dot{\mathbf{x}} \\ \dot{\hat{\mathbf{x}}} \end{bmatrix} = \begin{bmatrix} \mathbf{A} & -\mathbf{B}_{\mathbf{u}}\mathbf{K} \\ \mathbf{LC} & \mathbf{A} - \mathbf{LC} - \mathbf{B}_{\mathbf{u}}\mathbf{K} \end{bmatrix} \begin{bmatrix} \mathbf{x} \\ \hat{\mathbf{x}} \end{bmatrix} + \begin{bmatrix} \mathbf{B}_{\mathbf{l}} \\ 0 \end{bmatrix} d_l \tag{4.9}$$

A state flow diagram of (4.9) is shown in Figure 4.1.

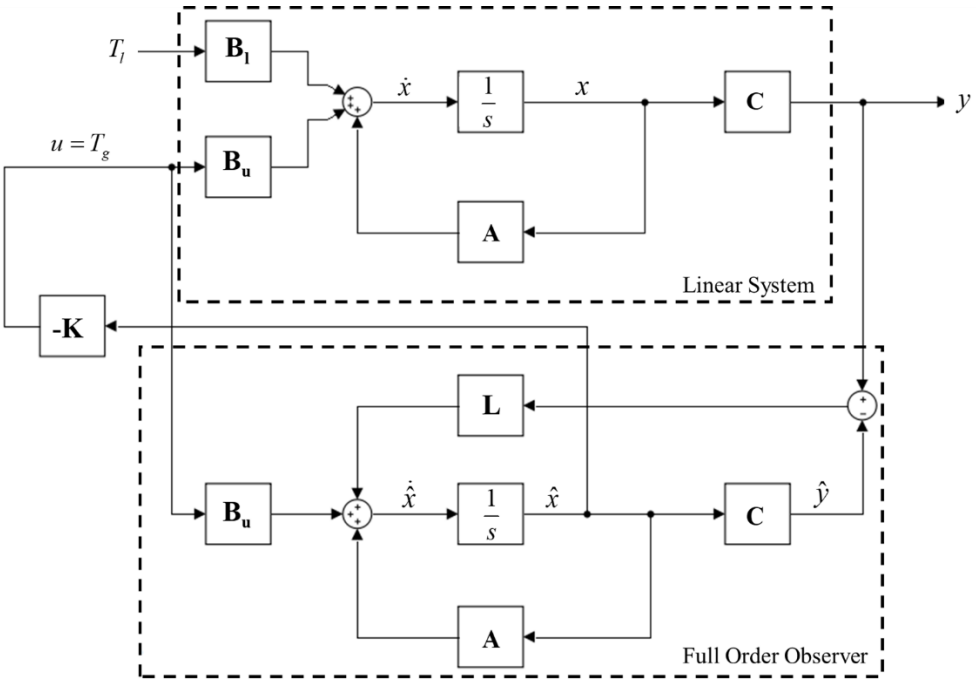

Figure 4.1. Magnetic gear state flow diagram, linear system, with observer state feedback control.

If the linear observer is applied to the nonlinear system, which will be the case in this section, the observer dynamics are defined by the second row in (4.9). The plant dynamics are defined by (2.18), (2.19) and (2.13). The flow diagram for the nonlinear system with full order observer is shown in Figure 4.2.

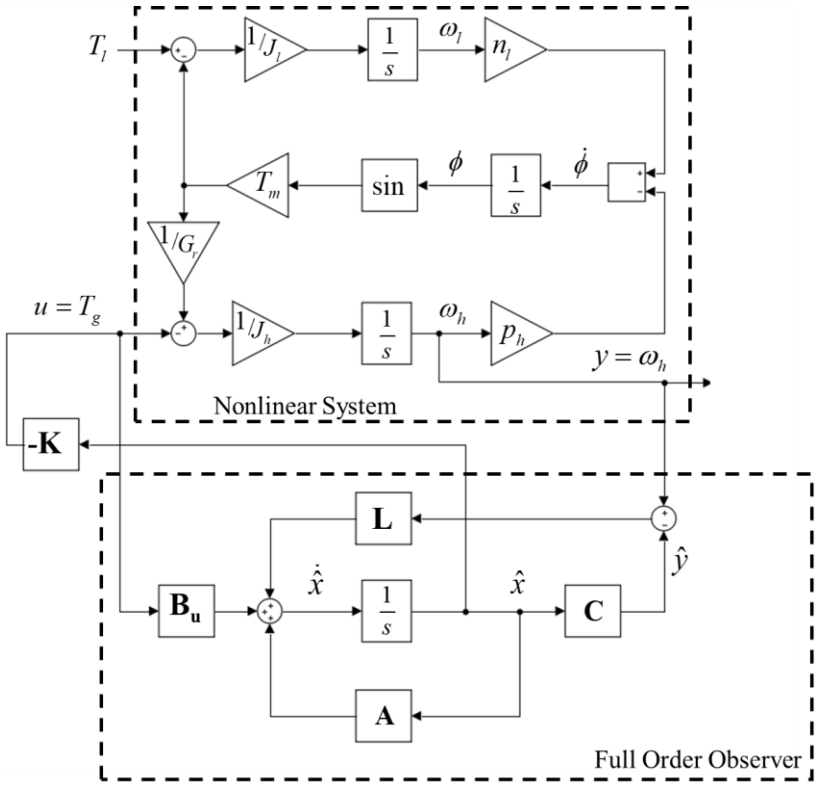

Figure 4.2. State flow diagram for the nonlinear system with observer state feedback control.

Equation (4.9) can be further simplified if we replace the full observer state vector with the estimate error in our state space model. The estimated error is defined as

$$e = (\mathbf{x} - \hat{\mathbf{x}}) . \tag{4.10}$$

Taking the derivative and substituting in (4.8) and (4.7) gives

$$\dot{\mathbf{e}} = \mathbf{Ax} - \mathbf{B_u K\hat{x}} - (\mathbf{A} - \mathbf{LC} - \mathbf{B_u K})\hat{\mathbf{x}} + \mathbf{LCx} + \mathbf{B_l} d_l \tag{4.11}$$

which simplifies to

$$\dot{\mathbf{e}} = (\mathbf{A} - \mathbf{LC})\mathbf{e} + \mathbf{B_l} d_l \tag{4.12}$$

Replacing $\dot{\hat{\mathbf{x}}}$ with (4.12), (4.9) becomes [6]

$$\begin{bmatrix} \dot{\mathbf{x}} \\ \dot{\mathbf{e}} \end{bmatrix} = \begin{bmatrix} \mathbf{A} & -\mathbf{B_u K} \\ 0 & \mathbf{A - LC} \end{bmatrix} \begin{bmatrix} \mathbf{x} \\ \mathbf{e} \end{bmatrix} + \mathbf{B_l} d_l \tag{4.13}$$

The benefit of this state equation is that it separates the feedback gains, **K**, from the observer gains, **L.** This separation allows the poles of each to be placed independently, provided all states are controllable and observable. The gain vector, **L**, is typically selected so that the poles of **A-LC** are 2-5 times faster (further to the left) than the system poles with state feedback [31]. This is done to ensure the estimate error, ***e***, converges to **0** as $t \to \infty$ quickly enough. Before doing this, we must verify that the state observer model we have defined is fully state observable. To determine observability, the rank of the observability matrix (4.14) is compared to the rank, *n*, of the **A** matrix.

$$\mathbf{O_b} = \begin{bmatrix} \mathbf{C} & \mathbf{CA} & \mathbf{CA}^2 ... \mathbf{CA}^{n-1} \end{bmatrix} \tag{4.14}$$

For the matrices defined in (3.6) and (3.11), equation (4.14) is evaluated as

$$\mathbf{O_b} = \begin{bmatrix} 1 & 0 & 0 \\ 0 & 0 & 899 \\ -2.7x10^3 & 1.5x10^4 & 0 \end{bmatrix} \tag{4.15}$$

With row swaps, multiplying rows by constants and adding them to other rows this reduces to

$$\mathbf{O_b} = \begin{bmatrix} 1 & 0 & 0 \\ 0 & 1 & 0 \\ 0 & 0 & 1 \end{bmatrix}. \tag{4.16}$$

The rank of the observability matrix is 3, which is also the size of the A matrix. Therefore, the state observer model as it has been defined is fully state observable.

To help select the observer pole multiplier, load angle simulations were run using observer poles placed 3, 4 and 5 times the state feedback poles (3.27). The simulated observer load angle error for each set of conditions is shown in Figure 4.3. For all three simulations, the initial condition for the observer load angle is $\phi_0 = 0^o$; and the initial load angle for the system is $\phi_0 = 1.94^o$. Using (2.44), this corresponds to $T_{l0} = 5$ Nm of steady state load torque.

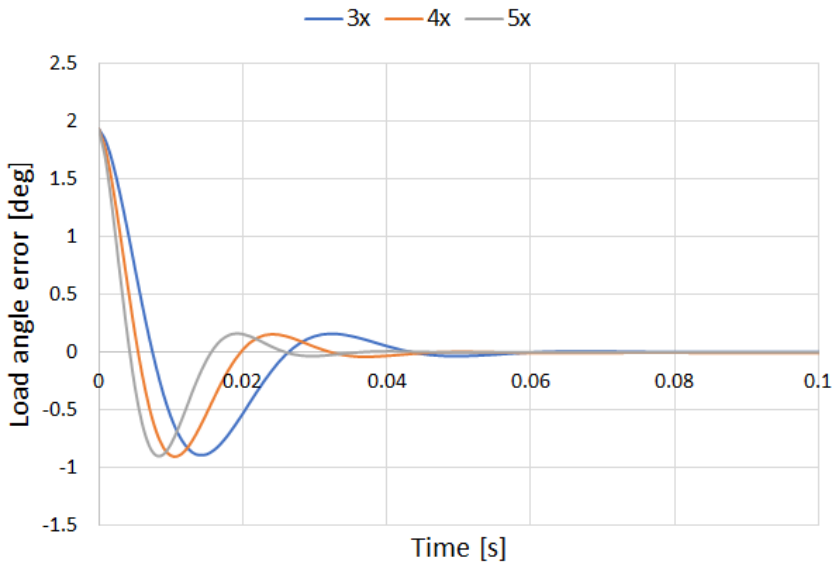

Figure 4.3. Observer load angle error for observer poles placed 3, 4- and 5-times state feedback poles

It is clear from Figure 4.3 that increasing the pole placement multiplier decreases the settling time. A multiplier of 5 is not that much faster than 4, so we will choose 4 to reduce control effort. The observer poles are the roots of

$$\Delta_{FO} = |s\mathbf{I} - (\mathbf{A} - \mathbf{LC})| \qquad (4.17)$$

Since we know we want to place them 4 times faster than the state feedback poles defined by (3.27), we can solve for the corresponding gains using the Matlab *place* command as follows

$$\begin{aligned}&\mathbf{P_{obs}}=4\mathbf{P}\\&\mathbf{P_{obs}}=[-352 \quad -176+235i \quad -176-235i]\\&\mathbf{L}=place[\mathbf{A},\mathbf{B_u},\mathbf{P_{obs}}]\end{aligned} \tag{4.18}$$

which yields

$$\begin{aligned}L_{\omega h} &= 704\\L_{\omega l} &= 1858\\L_{\phi} &= 227\end{aligned} \tag{4.19}$$

Figure 4.4 (a)-(c) and Figure 4.5 (a)-(b) show the linear system and linear full order observer responses of each state when the initial load angles are different. The load torque input to the system at the start of the simulation is 0 Nm, with an initial load angle (prior to the simulation start) of $\phi_0 = 1.94^o$ (5 Nm of load torque). The initial load angle for the observer is $\phi_0 = 0^o$. The purpose of this simulation is to see how well the observer can resolve differences in initial conditions.

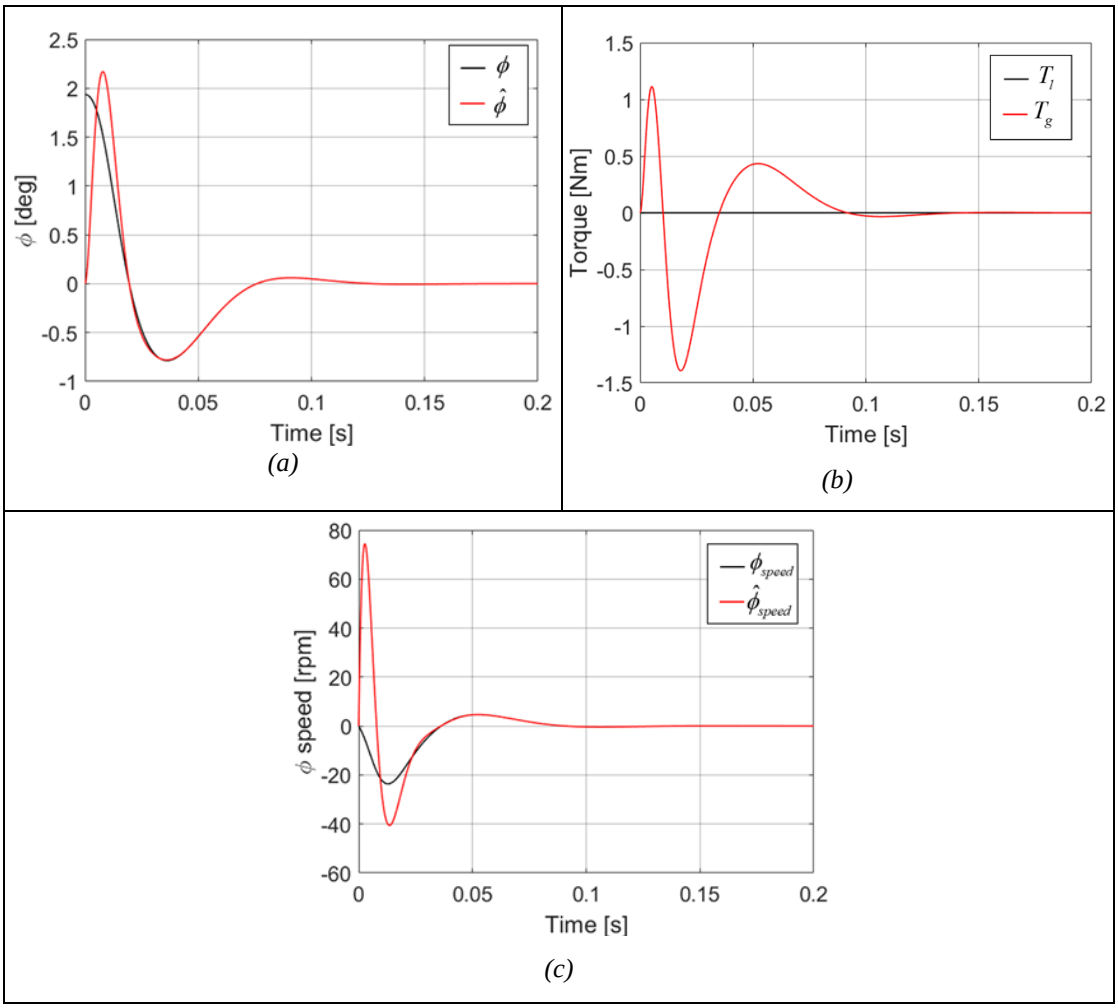

Figure 4.4. Transient plot showing non-linear system and full order observer states - load angle (a), torque (b), load angle speed (c) – when the initial load angle is $\phi_0 = 1.94^\circ$ *for the system and* $\phi_0 = 0^\circ$ *deg for the observer*

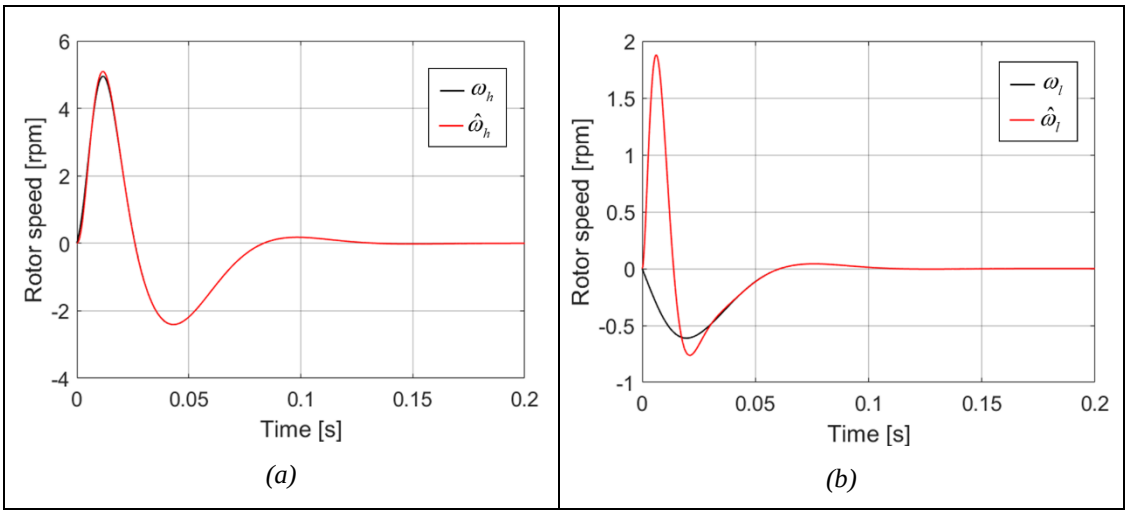

Figure 4.5. Transient plot showing non-linear system and full order observer states - HSR speed (a), LSR speed (b)– when the initial load angle is $\phi_0 = 1.94^\circ$ *for the system and* $\phi_0 = 0^\circ$ *for the observer*

It is clear from the plots that the selected observer gains quickly drive the estimation error to 0. The HSR speed shows the least amount of estimation error because that is the only state we can measure; hence it is the only one we are comparing to the output of the observer. Figure 4.6 (a)-(d) show the system and observer states when there is a 10 Nm step change in load torque from 0 Nm steady state. The initial load angles for the system and observer are $\phi_0 = 0^o$.

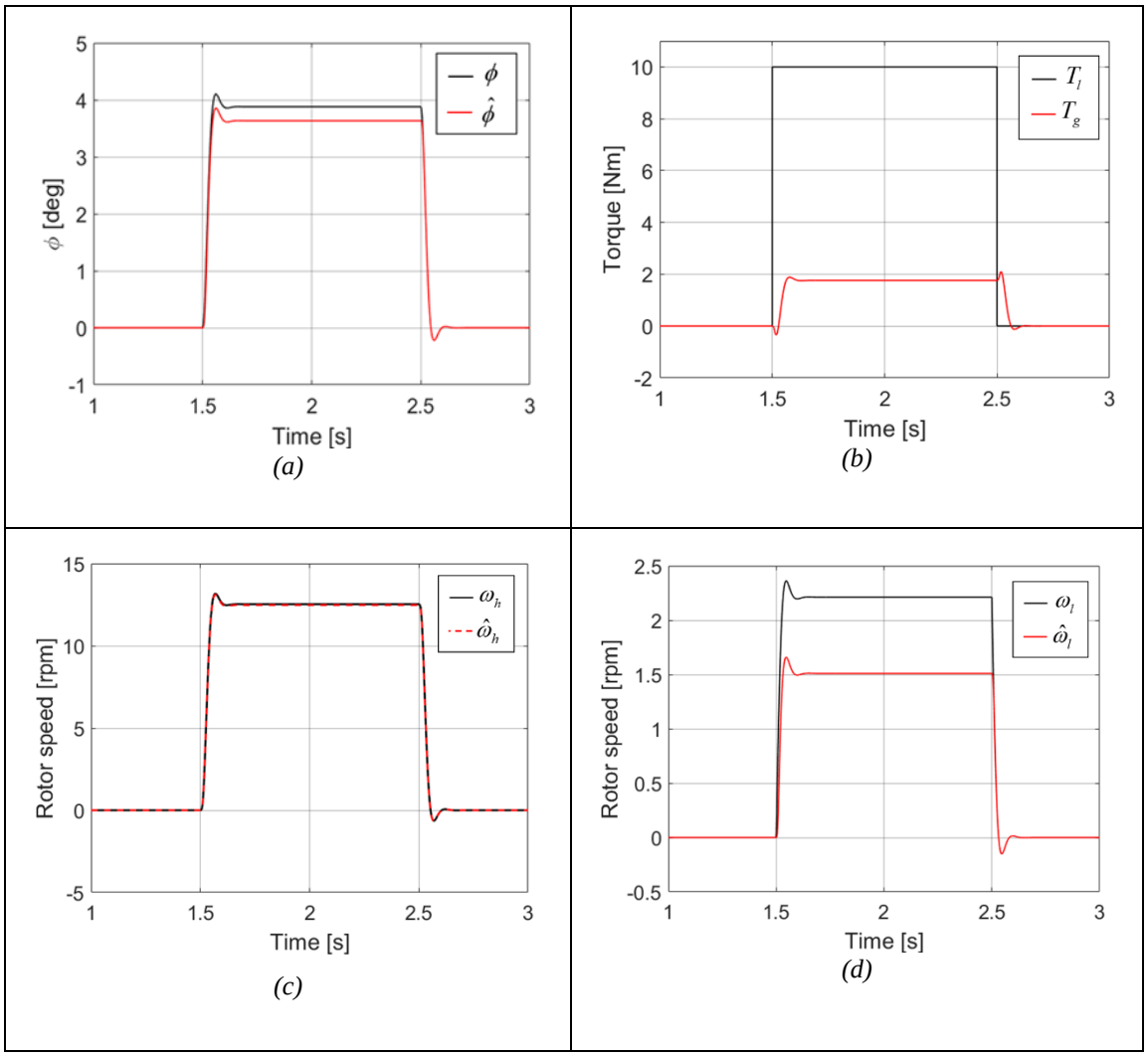

Figure 4.6. Transient plot showing nonlinear system and observer states - load angle (a), torque (b), HSR speed (c), LSR speed (d) - following a step change in load torque, T_l from 0-10 Nm at t = 1.5s.

It is clear from Figure 4.6 (a) and (d) that the full order observer estimates for load angle and LSR speed have steady state error. With only one measured signal (HSR speed) and the generator torque as inputs, the observer does not accurately account for the effect of load torque changes on the system. It is possible that the steady state error can be driven to zero with the addition of integral control and a reference input, *r*, for

defining error. Since the focus of this control scheme is load angle control, one potential candidate for the reference input is load angle speed.

4.1 Load Angle Speed Control

If we hypothesize that most of the load torque disturbances that lead to pole slipping would cause the load angle to change rapidly in the transient, we can set a fixed reference load angle speed to 0. We can then compare the load angle speed estimated from the observer to the reference; and integrate that error with an integral gain, K_i. The flow diagram for this non-linear system with full order observer plus integral control and load angle speed regulation [6] is shown in Figure 4.7.

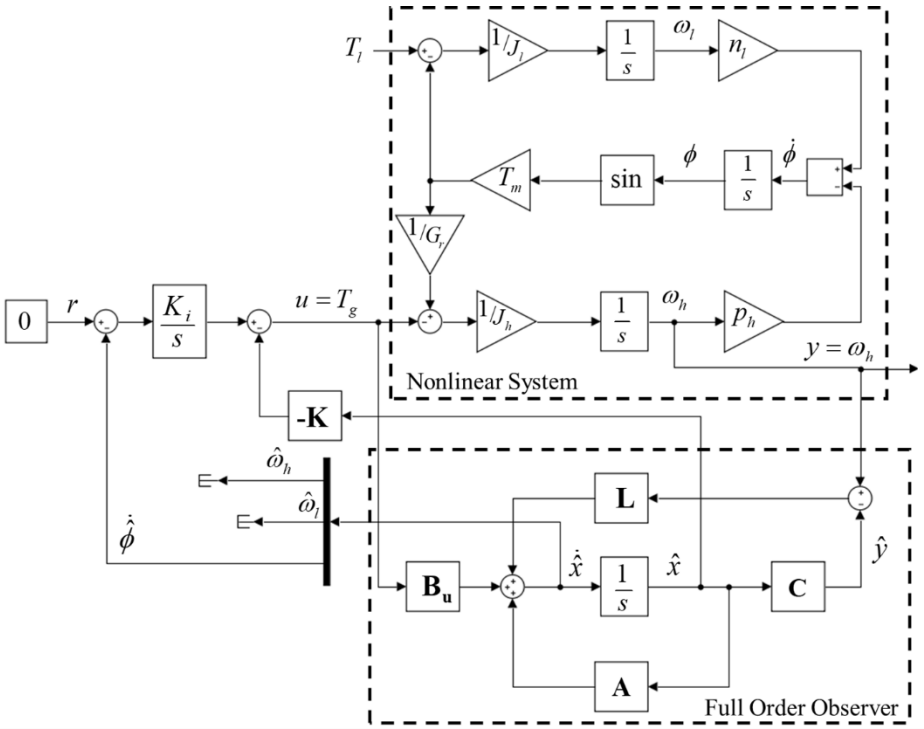

Figure 4.7. Magnetic gear drivetrain with full order observer and regulator with integral control.

Figure 4.8 shows the full order observer estimate of the load angle, with load angle speed regulation, for different values of the integral gain, K_i. The starting load angle for the simulations was $\phi_0 = 0^o$, the initial load torque was $T_l = 0$ Nm and there was a load disturbance step increase of 10 Nm at t = 0.4s. It is clear from the plots that varying the integral gain for load angle speed error regulation only impacts the transient evolution of the load angle. The steady state value of the load angle is not impacted.

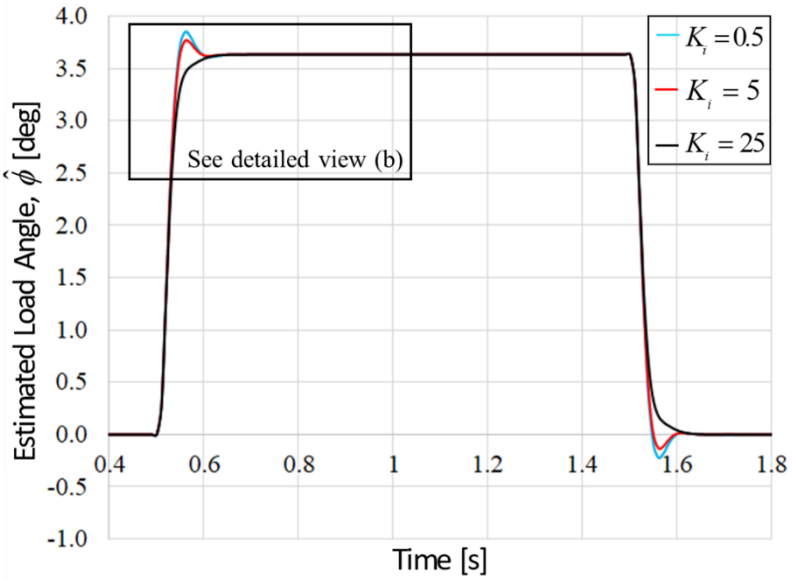

(a)

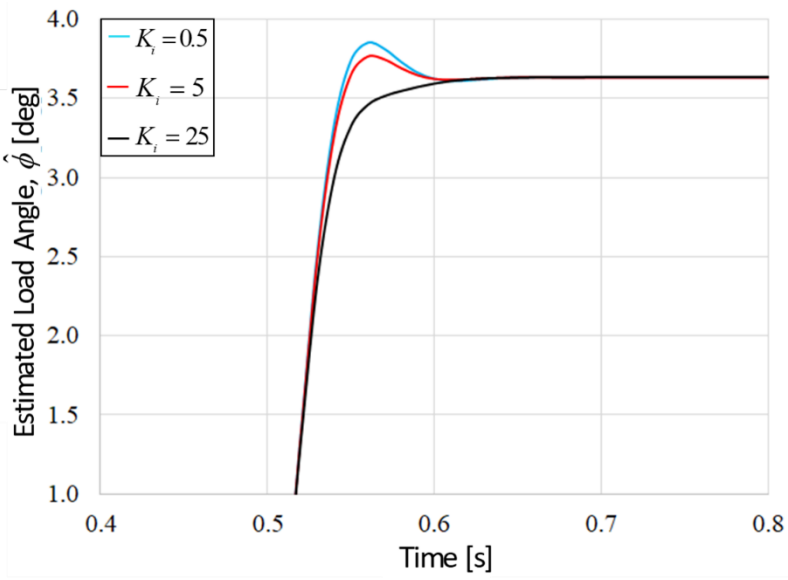

(b)

Figure 4.8. Transient plot showing full order observer estimated load angle for varying values of integral gain, K_i (a), and detailed view (b).

Similarly, Figure 4.9 shows the evolution of the non-linear system load angle for different values of K_i. Again, the steady state value of load angle is not affected by the addition of load angle speed regulation.

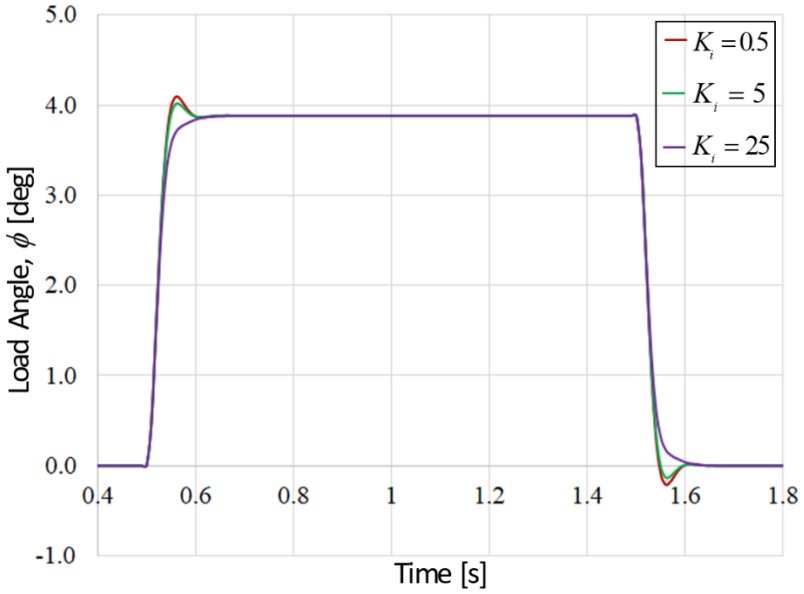

Figure 4.9. Transient plot showing non-linear system load angle for varying values of integral gain, K_i

To bring the focus back to the original issue, Figure 4.10 compares the evolution of the non-linear system load angle when $K_i = 0.5$, to the evolution of the full order estimated load angle for varying values of K_i. It is clear that the addition of the load angle speed regulation does not fix the steady state error in the observer estimated load angle.

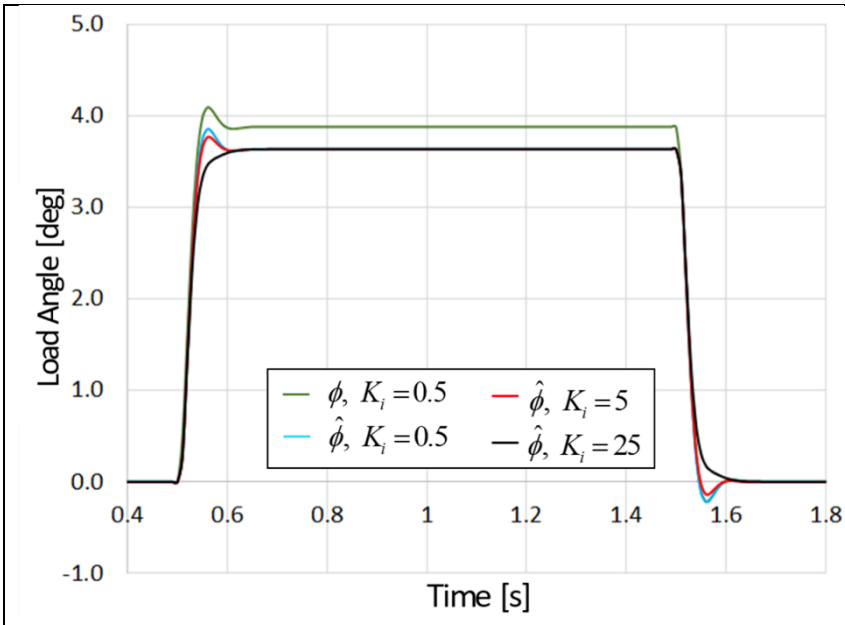

Figure 4.10. Transient plot comparing non-linear system load angle and estimated load angle for varying values of integral gain, K_i.

Figure 4.11 compares the transient plots of load angle speed from the non-linear system and from the reduced order observer with load angle speed regulation ($\hat{\phi}_{speed\_I}$) (Figure 4.7) for a step change in load torque from $T_l = 0$ Nm to $T_l = 10$ Nm. The initial load angles in both the magnetic gear model and the full order observer were set to $\phi_0 = 0^o$; and an arbitrary value was selected for the integral gain, $K_i = 1.5$. For ease of differentiation, dashed lines are used to plot state estimates that closely match the evolution of actual states.

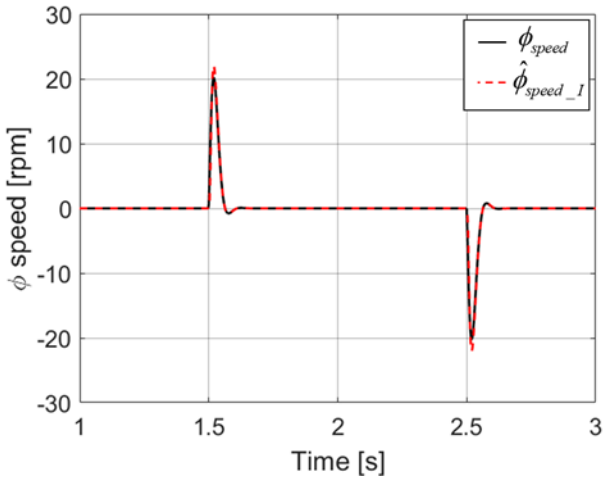

Figure 4.11. Actual and estimated load speed [rpm]. Load speed estimation from reduced order observer with load angle speed regulation (Figure 4.7).

Figure 4.12 (a)-(d) compares the non-linear system states to the states estimated by the reduced order observer ($\hat{x}$) and the reduced order observer with load angle speed regulation ($\hat{x}_I$). Again, it is clear from the plots that the addition of the load angle speed regulation does not improve the steady-state error. It is possible that increasing the response time might improve the performance. It is more likely that controlling the speed at which the load angle is changing does not ultimately affect the steady-state system load angle. This is controlled by the physical system load. Controlling the speed at which the load angle is changing might not affect the steady state estimated load angle either. That value is hardcoded into the linearized state space matrices. Controlling the load angle speed impacts the transient value of the load angle, but not the steady state value. The next section will look at using a reduced order observer and techniques for estimating the load torque disturbances.

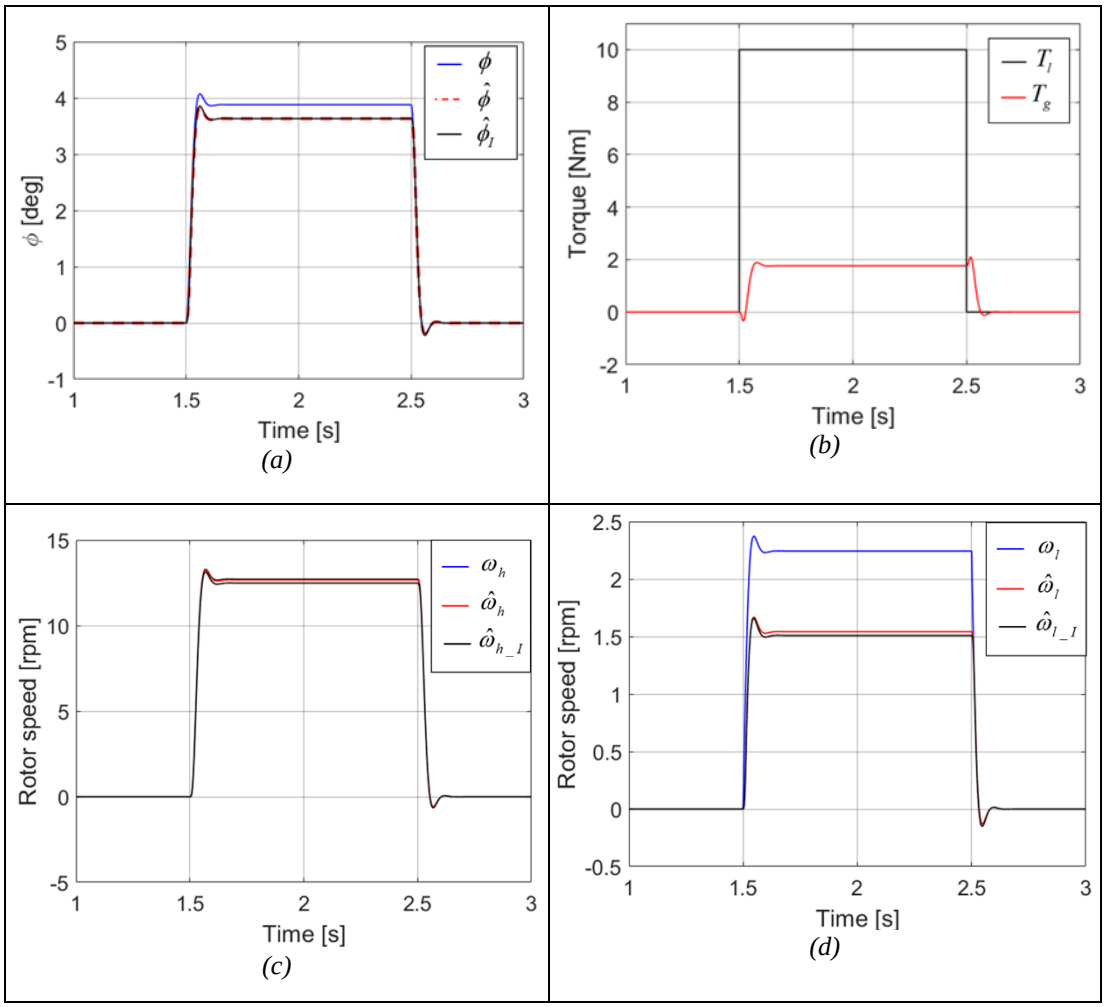

Figure 4.12. Transient plot showing nonlinear system and observer with load angle speed regulation states - load angle (a), torque (b), HSR speed (c), LSR speed (d) - following a step change in load torque, T_l from 0-10 Nm at t = 1.5s.

One approach to accounting for the disturbance load torque input that cannot reliably be measured is to add it to the observer as a state that can be estimated using measured and observed inputs. This idea has been explored by [8, 10, 16, 18]. If the load torque can be estimated with minimal error, it may be possible to then use that signal to counteract load angle transients and/or update the load angle in the linear controller.
If the load torque input is changed to a state, it will be assumed that the change in load torque is sufficiently slow, compared to the observer dynamics, that the load torque derivative is 0. If initial conditions are set to 0 the model defined by (3.1) becomes

$$\begin{bmatrix} \dot{\omega}_h \\ \dot{\omega}_l \\ \dot{\phi} \\ \dot{T}_l \end{bmatrix} = \begin{bmatrix} 0 & 0 & \dfrac{T_{\mathrm{m}} \cos[\phi]}{J_h G_r} & 0 \\ 0 & 0 & \dfrac{-T_{\mathrm{m}} \cos[\phi]}{J_l} & \dfrac{1}{J_l} \\ -p_h & n_l & 0 & 0 \\ 0 & 0 & 0 & 0 \end{bmatrix} \begin{bmatrix} \omega_h \\ \omega_l \\ \phi \\ T_l \end{bmatrix} - \begin{bmatrix} \dfrac{1}{J_h} \\ 0 \\ 0 \\ 0 \end{bmatrix} T_g \qquad (5.1)$$

$$\mathbf{y} = \begin{bmatrix} 1 & 0 & 0 & 0 \end{bmatrix} \begin{bmatrix} \omega_h \\ \omega_l \\ \phi \\ T_l \end{bmatrix}$$

One way the observer can be simplified is to remove the states that can be measured, in this case ω_h. The measured state will still be used as an input to the observer, but it will not be estimated with the others. This creates what is known as a reduced order (RO) observer, constructed from the model defined in (5.1), which is of the form:

$$\begin{aligned}\dot{\mathbf{x}} &= \mathbf{A}\mathbf{x} + \mathbf{B}u \\ y &= \mathbf{C}\mathbf{x}\end{aligned} \tag{5.2}$$

From here the state vector is partitioned into observable, x_1, and non-observable, x_2, parts where

$$\tilde{\mathbf{x}} = [x_1 \ \tilde{\mathbf{x}}_2]^T \tag{5.3}$$

$$x_1 = \omega_h \tag{5.4}$$

$$\tilde{\mathbf{x}}_2 = \begin{bmatrix} \omega_l & \phi & T_l \end{bmatrix}^T \tag{5.5}$$

so that (5.2) becomes [32]

$$\begin{bmatrix} \dot{x}_1 \\ \dot{\tilde{\mathbf{x}}}_2 \end{bmatrix} = \left[\begin{array}{c|c} A_{11} & \mathbf{A}_{12} \\ \hline \mathbf{A}_{21} & \mathbf{A}_{22} \end{array}\right] \begin{bmatrix} x_1 \\ \tilde{\mathbf{x}}_2 \end{bmatrix} + \begin{bmatrix} B_1 \\ \mathbf{B}_2 \end{bmatrix} u \tag{5.6}$$

and

$$\begin{bmatrix} y_1 \\ y_2 \end{bmatrix} = \begin{bmatrix} C_1 \mid C_2 \end{bmatrix} \begin{bmatrix} x_1 \\ \tilde{\mathbf{x}}_2 \end{bmatrix} \tag{5.7}$$

where

$$C_1 = 1 \tag{5.8}$$

$$C_2 = 0 \tag{5.9}$$

$$A_{11} = 0 \tag{5.10}$$

$$\mathbf{A}_{12} = \begin{bmatrix} 0 & \dfrac{T_{\mathrm{m}} \cos[\phi]}{J_h G_r} & 0 \end{bmatrix} \tag{5.11}$$

$$\mathbf{A}_{21} = \begin{bmatrix} 0 & -p_h & 0 \end{bmatrix}^T \tag{5.12}$$

$$\mathbf{A}_{22} = \begin{bmatrix} 0 & \dfrac{-T_{\mathrm{m}} \cos[\phi]}{J_l} & \dfrac{1}{J_l} \\ n_l & 0 & 0 \\ 0 & 0 & 0 \end{bmatrix} \tag{5.13}$$

$$B_1 = \frac{-1}{J_h} \tag{5.14}$$

$$\mathbf{B}_2 = \begin{bmatrix} 0 & 0 & 0 \end{bmatrix}^T \tag{5.15}$$

From here, the reduced order observer is constructed according to the processes developed in [32], [33], and [6].

The development of a reduced order observer is like that of the full-order observer. The observer is modeled on the plant, with estimated states replacing the states that cannot be measured, and a weighted correction factor that multiplies the difference between the measured and estimated outputs. The main difference is that the full-order observer contains all the system states, giving it an order of *n*. The reduced order observer has an order of *n-m*, where *n* is the order of the system and *m* is the number of states that can be measured. The reduced order equations can be taken from (5.6) and (5.7). The equation for the measured states is given by

$$\dot{x}_1 = A_{11} x_1 + \mathbf{A}_{12} \tilde{\mathbf{x}}_2 + B_1 u \tag{5.16}$$

The equation for the unmeasured states is given by

$$\dot{\tilde{\mathbf{x}}}_2 = (\mathbf{A}_{21} x_1 + \mathbf{B}_2 u) + \mathbf{A}_{22} \tilde{\mathbf{x}}_2 \tag{5.17}$$

divided into measured (parentheses) and unmeasured parts; and noting that $A_{11} = 0$ and $\mathbf{B_2} = \mathbf{0}$, (5.16)-(5.17) become

$$\dot{x}_1 = \mathbf{A}_{12}\tilde{\mathbf{x}}_2 + B_1 u \tag{5.18}$$

$$\dot{\tilde{\mathbf{x}}}_2 = \mathbf{A}_{21}x_1 + \mathbf{A}_{22}\tilde{\mathbf{x}}_2 \tag{5.19}$$

Since the output only contains the measured states the output equation for the system is

$$\begin{aligned} y &= y_1 \\ &= C_1 x_1 \\ &= x_1 \end{aligned} \tag{5.20}$$

The observer state vector is given by

$$\tilde{\mathbf{x}} = \begin{bmatrix} x_1 & \tilde{\mathbf{x}}_2 \end{bmatrix}^T \tag{5.21}$$

This shows that the measured states are part of the reduced order observer but are fed in as known variables. While [32] chose to define an observer equation for the measured states, it is simply a duplicate of (5.16), and will be omitted here. From (5.19), the observer equation with an output error corrective term added is

$$\dot{\tilde{\mathbf{x}}}_2 = \mathbf{A}_{21}x_1 + \mathbf{A}_{22}\tilde{\mathbf{x}}_2 + \mathbf{L}_r(y - \tilde{y}) \tag{5.22}$$

where the tilde sign, ~, indicates a reduced order estimated parameter; and $\mathbf{L_r}$ is the corrective output error gain matrix. From (5.3), and (5.7)-(5.9)

$$\begin{aligned} y &= \mathbf{C}\mathbf{x} \\ &= \begin{bmatrix} 1 & \mathbf{0} \end{bmatrix} \begin{bmatrix} x_1 \\ \tilde{\mathbf{x}}_\mathbf{2} \end{bmatrix} \\ &= x_1 \end{aligned} \tag{5.23}$$

similarly, replacing (5.3) with (5.21)

$$\begin{aligned}\tilde{y} &= \mathbf{C}\tilde{\mathbf{x}} \\ &= \begin{bmatrix}1 & 0\end{bmatrix}\begin{bmatrix}x_1 \\ \tilde{\mathbf{x}}_2\end{bmatrix}. \\ &= x_1\end{aligned} \tag{5.24}$$

If we define the plant and observer output to be the same, then only the measured states will be reflected in the output and the error will always be 0. A different way to define the observer output equation was set forth by [33]. If we assume that having access to the measurements in *y* means we also have access to their derivatives then from (5.20)

$$\dot{y} = \dot{x}_1 \tag{5.25}$$

and substituting (5.18) into (5.25) yields

$$\dot{y} = \mathbf{A}_{12}\tilde{\mathbf{x}}_2 + B_1 u \tag{5.26}$$

Rearranging so that measured terms are on one side and unmeasured terms are on the other

$$\dot{y} - B_1 u = \mathbf{A}_{12}\tilde{\mathbf{x}}_2 \tag{5.27}$$

If we treat the measured terms as the plant output and the unmeasured terms as the observer output, then substituting into (5.22) gives

$$\dot{\tilde{\mathbf{x}}}_2 = \mathbf{A}_{21}x_1 + \mathbf{A}_{22}\tilde{\mathbf{x}}_2 + \mathbf{L}_\mathbf{r}(\dot{y} - B_1 u - \mathbf{A}_{12}\tilde{\mathbf{x}}_2) \tag{5.28}$$

It was pointed out by [6, 33], that the use of the derivative of $y\ (= x_1)$ to estimate $\tilde{x}_2$ can amplify system noise, and should be avoided. To eliminate $\dot{y}$, first expand and rearrange (5.28), which gives

$$\dot{\tilde{\mathbf{x}}}_2 - \mathbf{L}_\mathbf{r}\dot{y} = (-\mathbf{L}_\mathbf{r}B_1)u + (\mathbf{A}_{22} - \mathbf{L}_\mathbf{r}\mathbf{A}_{12})\tilde{\mathbf{x}}_2 + \mathbf{A}_{21}y\,. \tag{5.29}$$

Then, define a new variable

$$\mathbf{z} = \tilde{\mathbf{x}}_2 - \mathbf{L}_\mathbf{r} y \tag{5.30}$$

and rearrange (5.30) as

$$\tilde{\mathbf{x}}_2 = \mathbf{z} + \mathbf{L}_\mathbf{r} y \,. \tag{5.31}$$

Now, substitute (5.31) into (5.29), and expand and group

$$\begin{aligned} \dot{\tilde{\mathbf{x}}}_2 - \mathbf{L}_\mathbf{r}\dot{y} &= -\mathbf{L}_\mathbf{r} B_1 u + (\mathbf{A}_{22} - \mathbf{L}_\mathbf{r}\mathbf{A}_{12})(\mathbf{z} + \mathbf{L}_\mathbf{r} y) + \mathbf{A}_{21} y \\ &= -\mathbf{L}_\mathbf{r} B_1 u + \mathbf{A}_{22}\mathbf{z} + \mathbf{A}_{22}\mathbf{L}_\mathbf{r} y - \mathbf{L}_\mathbf{r}\mathbf{A}_{12}\mathbf{z} - \mathbf{L}_\mathbf{r}\mathbf{A}_{12}\mathbf{L}_\mathbf{r} y + \mathbf{A}_{21} y \\ &= (\mathbf{A}_{22} - \mathbf{L}_\mathbf{r}\mathbf{A}_{12})\mathbf{z} + [(\mathbf{A}_{22} - \mathbf{L}_\mathbf{r}\mathbf{A}_{12})\mathbf{L}_\mathbf{r} + \mathbf{A}_{21}]y - \mathbf{L}_\mathbf{r} B_1 u \end{aligned}$$

(5.32)

define

$$\mathbf{F} = \mathbf{A}_{22} - \mathbf{L}_\mathbf{r}\mathbf{A}_{12} \tag{5.33}$$

$$\mathbf{G} = -\mathbf{L}_\mathbf{r} B_1 \tag{5.34}$$

then substituting (5.33) and (5.34) into (5.32) gives

$$\dot{\mathbf{z}} = \mathbf{F}\mathbf{z} + [\mathbf{A}_{21} + \mathbf{F}\mathbf{L}_\mathbf{r}]y + \mathbf{G}u \,. \tag{5.35}$$

We can simplify further by defining

$$\mathbf{H} = \mathbf{A}_{21} + \mathbf{F}\mathbf{L}_\mathbf{r} \tag{5.36}$$

and substituting (5.36) into (5.35) gives

$$\dot{\mathbf{z}} = \mathbf{F}\mathbf{z} + \mathbf{G}u + \mathbf{H}y \,. \tag{5.37}$$

The partitioned observer error matrix equation can be defined as

$$\mathbf{e} = \begin{pmatrix} e_1 \\ \mathbf{e}_2 \end{pmatrix} \mathbf{x} - \tilde{\mathbf{x}} = \begin{bmatrix} x_1 - \tilde{x}_1 \\ \mathbf{x}_2 - \tilde{\mathbf{x}}_2 \end{bmatrix} \tag{5.38}$$

but since x_1 is measured not observed

$$\tilde{x}_1 = x_1 \tag{5.39}$$

thus

$$e_1 = 0 \tag{5.40}$$

and the only error we are concerned with is

$$\mathbf{e}_2 = \mathbf{x}_2 - \tilde{\mathbf{x}}_2 . \tag{5.41}$$

To see how the error evolves with time, take the derivative of (5.41)

$$\dot{\mathbf{e}}_2 = \dot{\mathbf{x}}_2 - \dot{\tilde{\mathbf{x}}}_2 \tag{5.42}$$

and substitute (5.19) and (5.28) into (5.42), which gives

$$\dot{\mathbf{e}}_2 = (\mathbf{A}_{21}x_1 + \mathbf{A}_{22}\mathbf{x}_2) - (\mathbf{A}_{21}x_1 + \mathbf{A}_{22}\tilde{\mathbf{x}}_2 + \mathbf{L}_\mathbf{r}(\dot{y} - B_1u - \mathbf{A}_{12}\tilde{\mathbf{x}}_2)) . \tag{5.43}$$

Now, cancelling terms and rearranging gives

$$\begin{aligned} \dot{\mathbf{e}}_2 &= \mathbf{A}_{22}\mathbf{x}_2 - \mathbf{A}_{22}\tilde{\mathbf{x}}_2 - \mathbf{L}_\mathbf{r}(\mathbf{A}_{12}\mathbf{x}_2 - \mathbf{A}_{12}\tilde{\mathbf{x}}_2) \\ \dot{\mathbf{e}}_2 &= (\mathbf{A}_{22} - \mathbf{L}_\mathbf{r}\mathbf{A}_{12})(\mathbf{x}_2 - \tilde{\mathbf{x}}_2) \end{aligned} \tag{5.44}$$

and substituting (5.41) into (5.44) gives

$$\dot{\mathbf{e}}_2 = (\mathbf{A}_{22} - \mathbf{L}_\mathbf{r}\mathbf{A}_{12})\mathbf{e}_2 . \tag{5.45}$$

Equation (5.45) shows that the reduced order observer error dynamics can be shaped by selecting the $\mathbf{L}_r$ gain matrix. But first it must be shown that the matrix pair ($\mathbf{A}_{12}$, $\mathbf{A}_{22}$) is observable. This can be determined by evaluating

$$\tilde{\mathbf{O}}_b = [\mathbf{A}_{12}^T \quad \mathbf{A}_{22}^T\mathbf{A}_{12}^T \quad (\mathbf{A}_{22}^T)^{n-m-1}\mathbf{A}_{12}^T] \tag{5.46}$$

If the rank of $\tilde{\mathbf{O}}_b$ is *n-m*, where *n* is the order of the system and *m* is the number of independent, measurable outputs, the observability condition is satisfied.

The order of the system given in (5.6) is 4 and there is 1 measurable state. This gives $n - m = 3$. Substituting (5.11) and (5.13) into (5.46), with values from Table 2.1, yields the observability test matrix

$$\tilde{\mathbf{O}}_b = \begin{bmatrix} 0 & 4.69x10^4 & 0 \\ 1172 & 0 & -1.61x10^8 \\ 0 & 0 & 9x10^4 \end{bmatrix} \tag{5.47}$$

with reduced row echelon form

$$\tilde{\mathbf{O}}_b = \begin{bmatrix} 1 & 0 & 0 \\ 0 & 1 & 0 \\ 0 & 0 & 1 \end{bmatrix} \tag{5.48}$$

which has a rank of 3. Therefore, the reduced order observer poles, the roots of

$$\Delta_{RO} = \left| s\mathbf{I} - (\mathbf{A}_{22} - \mathbf{L}_\mathbf{r}\mathbf{A}_{12}) \right| \tag{5.49}$$

can be placed as needed. The reduced order observer will use the same poles as the full order observer, these poles are defined in (4.18). However, now the gains will be solved for using

$$\mathbf{L}_\mathbf{r} = place(A_{22}^T, A_{12}^T, poles) \tag{5.50}$$

which yields

$$\begin{aligned} L_{r\omega h} &= 14.4 \\ L_{r\omega l} &= 0.83 \\ L_{r\phi} &= 1962 \end{aligned}$$

The reduced order observer flow diagram using (5.6)-(5.15) and (5.33)-(5.36) is shown in Figure 5.1.

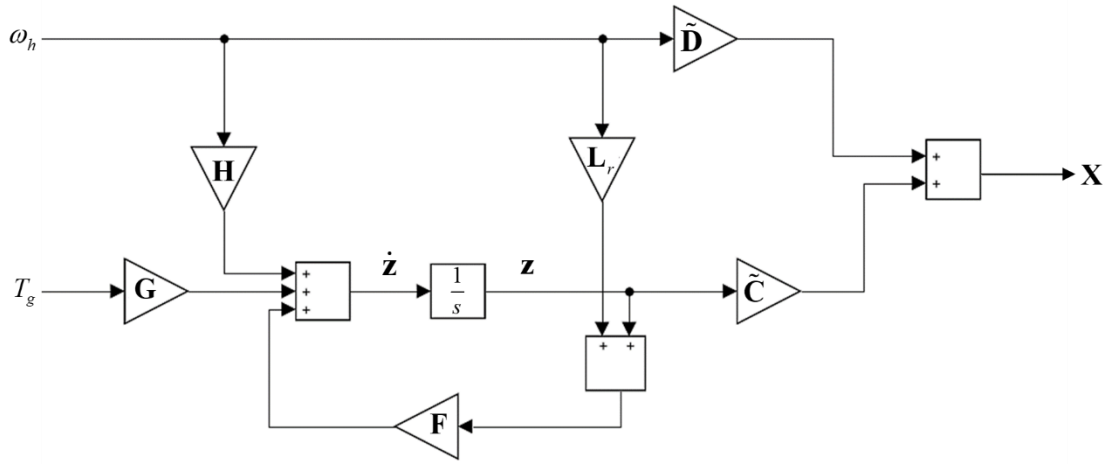

Figure 5.1. Flow diagram for reduced order observer

where

$$\tilde{\mathbf{C}} = \begin{bmatrix} 0 & 0 & 0 \\ 1 & 0 & 0 \\ 0 & 1 & 0 \\ 0 & 0 & 1 \end{bmatrix} \tag{5.51}$$

$$\tilde{\mathbf{D}} = \begin{bmatrix} 1 \\ \mathbf{L_r} \end{bmatrix} \tag{5.52}$$

The $\tilde{\mathbf{C}}$ and $\tilde{\mathbf{D}}$ matrices transform the states from **z** back to **x** through the relationship defined in (5.30). The next question that needs to be addressed is how to incorporate the estimated states into the controller.

5.1 Reduced Order Observer - State Feedback Control

We saw in Chapter 4, that if the controllability and observability conditions are met, the estimated states of the full order observer can be incorporated into the state feedback control law. For the reduced order observer, the observability condition was satisfied as shown by (5.46)-(5.48). The system controllability matrix was given in (3.12). With the addition of another state to the observer, we must verify that the system is still controllable. Considering (5.1), the $\bar{\mathbf{A}}$ and $\bar{\mathbf{B}}$ matrices are given by

$$\bar{\mathbf{A}} = \begin{bmatrix} 0 & 0 & \dfrac{T_{\mathrm{m}} \cos[\phi]}{J_h G_r} & 0 \\ 0 & 0 & \dfrac{-T_{\mathrm{m}} \cos[\phi]}{J_l} & \dfrac{1}{J_l} \\ -p_h & n_l & 0 & 0 \\ 0 & 0 & 0 & 0 \end{bmatrix} \tag{5.53}$$

$$\bar{\mathbf{B}} = \begin{bmatrix} \dfrac{1}{J_h} & 0 & 0 & 0 \end{bmatrix}^T \tag{5.54}$$

Substituting (5.53) and (5.54) into (3.12), with load angle $\phi_0 = 0^o$, gives

$$\bar{\mathbf{C}}_o = \begin{bmatrix} 4.55 & 0 & -31973 & 0 \\ 0 & 0 & 93835 & 0 \\ 0 & -27.27 & 0 & 3.95x10^6 \\ 0 & 0 & 0 & 0 \end{bmatrix} \tag{5.55}$$

Rearranging (5.55), multiplying through by constants and adding rows gives the reduced row echelon form as follows

$$\bar{\mathbf{C}}_o = \begin{bmatrix} 1 & 0 & 0 & 0 \\ 0 & 1 & 0 & -1.45x10^5 \\ 0 & 0 & 1 & 0 \\ 0 & 0 & 0 & 0 \end{bmatrix}. \qquad (5.56)$$

The rank of $\bar{\mathbf{C}}_o$ is 3, which is less than the size of the $\bar{\mathbf{A}}$ matrix. Therefore, adding the disturbance input to the state matrix has meant that the system is no longer fully state controllable. This problem was discussed in detail by [32]. When there are disturbance or reference inputs to a system, there is a natural inclination to turn them into states that can be estimated and integrated into an observer state feedback control scheme.

These new states are referred to as 'metastates' [32]; and while they can often be observed they cannot be controlled. Ultimately what this means for this controller design is that the load torque metastate can be observed but it cannot be fed back into the system as part of observer state feedback control. However, the original state estimates still form a controllable subset that can be used for state feedback. Figure 5.2 gives a state flow diagram for the nonlinear magnetic gear with linear reduced order (RO) observer. Note that the load torque output from the reduced order observer is terminated, not fed back into the system.

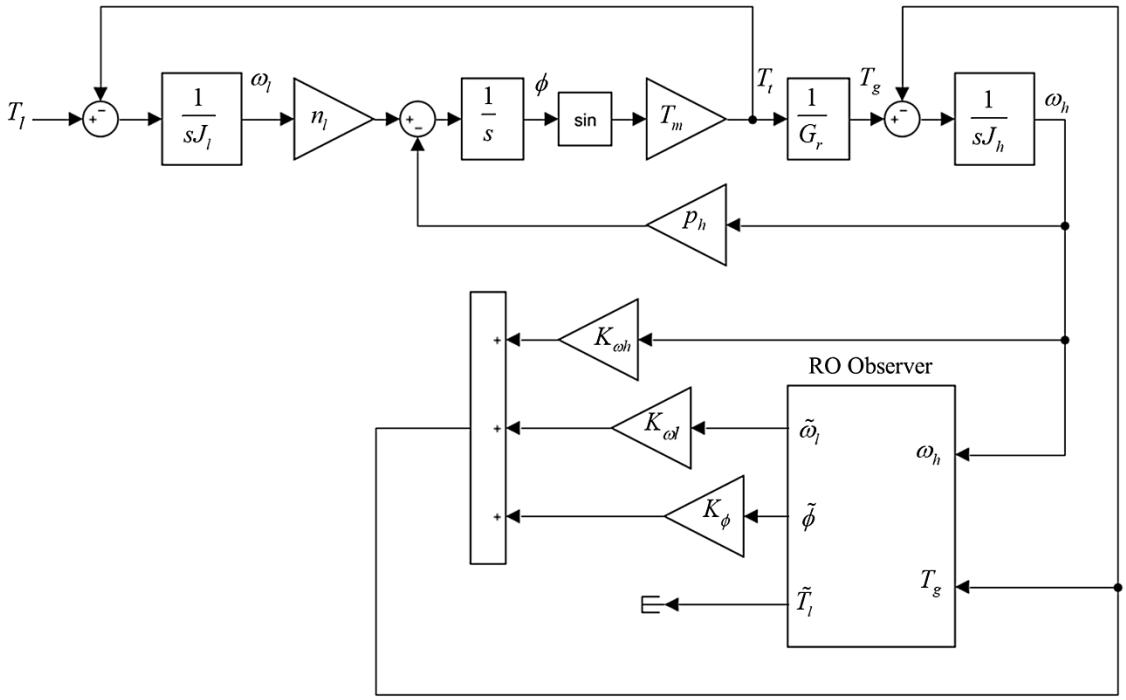

Figure 5.2. Nonlinear magnetic gear with reduced order observer state feedback.

Figure 5.3 (a)-(d) show actual and estimated states when the magnetic gear is operating with $T_{l0} = 50$ Nm of load torque in steady state and then there is a 10 Nm load disturbance at time t = 1.5s. For ease of differentiation, dashed lines are used to plot state estimates that closely match the evolution of actual states. From Figure 5.3 (a) it is clear that the load angle offset is also a problem with the reduced order observer.

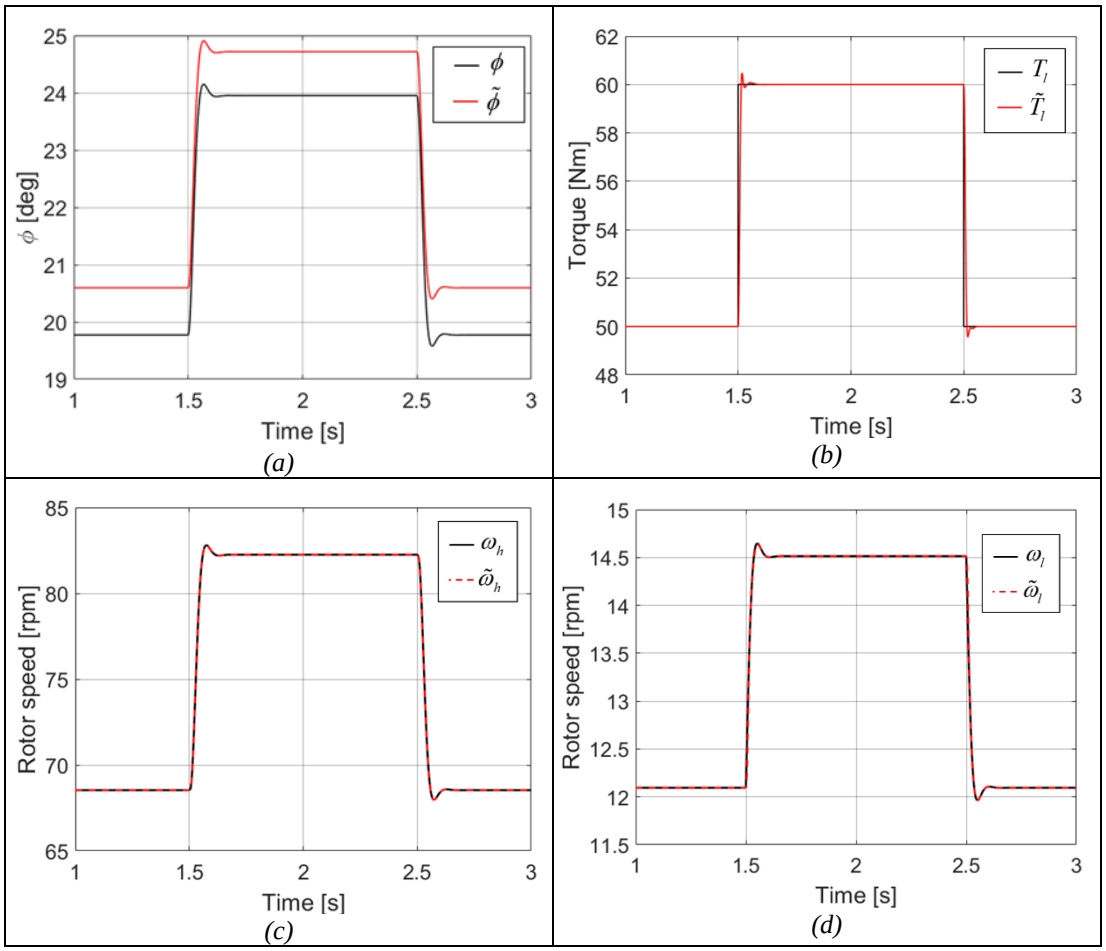

Figure 5.3. Transient plot showing nonlinear system and observer states - load angle (a), torque (b), HSR speed (c), LSR speed (d) - following a step change in load torque, T_l from 50-60 Nm at t = 1.5s.

One thing to note from Figure 5.3 (b) is, despite the error in load angle estimation, the reduced order observer does a good job of estimating the load torque. This could be useful for correcting the error in load angle estimation; and will be the focus of the next section.

5.2 Load Angle Correction

The relationship between magnetic torque and load angle was defined for steady-state conditions in (2.44). Here we can note that in steady state, $\dot{\omega}_L = 0$, and so (2.18) simplifies to

$$T_l = T_{\mathrm{m}} \sin(\phi), \tag{5.57}$$

which indicates that, without damping, the load torque and magnetic torque are equal in steady state. Solving (5.57) for load angle yields

$$\phi = \sin^{-1}(\frac{T_l}{T_m}) \tag{5.58}$$

We can use this relationship to approximate the load angle from the estimated load torque. Figure 5.4 shows a flow diagram for (5.58).

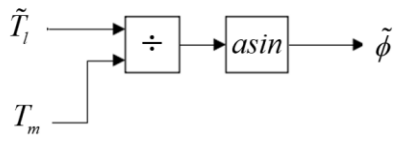

Figure 5.4. Flow diagram for (5.58)

Figure 5.5 shows the flow diagram for the load angle calculation in the structure of the reduced order observer.

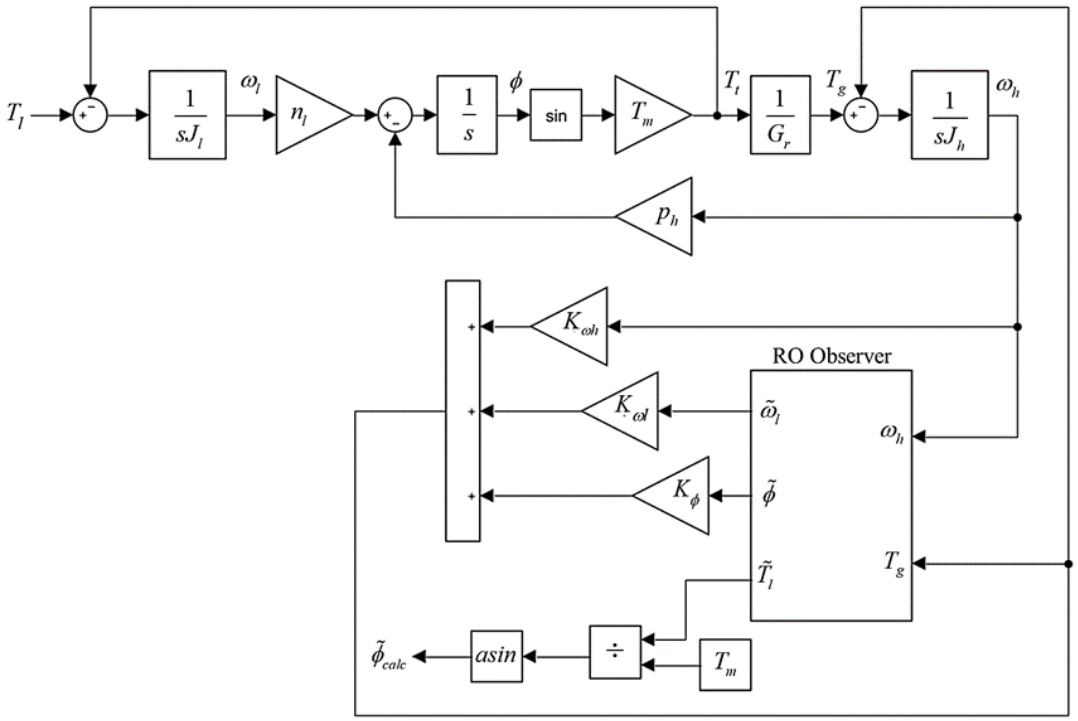

Figure 5.5. Flow diagram for nonlinear system with reduced order observer and load angle calculation from estimated load torque.

Figure 5.6 shows the system and calculated load angles, when using (5.58), following a step change in load torque from 50-60 Nm. Figure 5.7 shows the load torque applied to the system to produce the plots in Figure 5.6; and the load torque estimate from the reduced order observer. The calculated load angle is a good approximation of the system load angle, with only a small amount of error in the transient response to changes in load torque. This error, which appears as an almost instantaneous response to load torque changes compared to a slower system load angle response, is due to the fact that the equation for calculating the load angle (5.58) assumes that $\dot{\omega}_L = 0$.

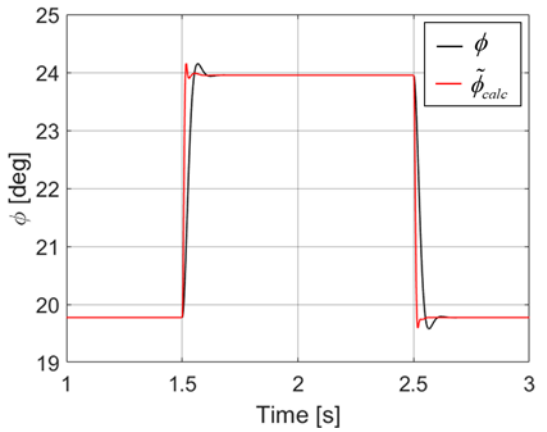

Figure 5.6. Transient plot of non-linear system load angle and load angle calculated from the reduced order estimated load torque (5.58).

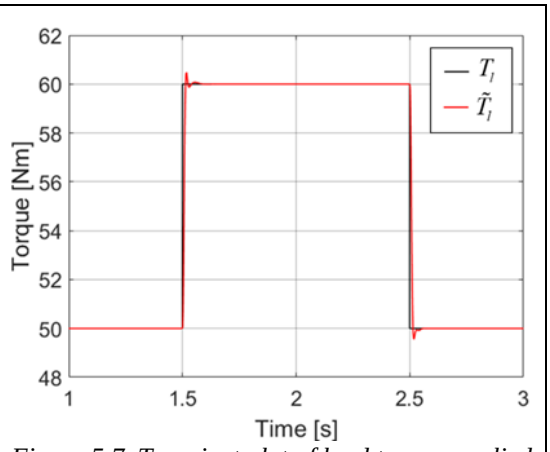

Figure 5.7. Transient plot of load torque applied to the non-linear system and load torque estimated by the reduced order observer.

For comparison purposes, Figure 5.8 shows the system load angle, the reduced order estimated load angle ($\tilde{\phi}$) and the load angle calculated from the reduced order observer estimate of the load torque ($\tilde{\phi}_{calc}$). Simulation conditions for system and observer are an initial load torque of $T_{l0} = 50$ Nm, an initial load angle of $\phi_0 = 19.78^o$, and a 10 Nm step disturbance at t = 1.5 s. With the restrictions this thesis has placed on observer design – the generator torque and high-speed rotor speeds are the only available inputs – the best way to dynamically estimate the system load angle is by calculating it from the estimated load torque. Finding a way to use the calculated load angle to dynamically update the reduce order observer is an objective for future research. The final section of this thesis will look at how well the reduced order observer can estimate load torque fluctuations from wind turbine data.

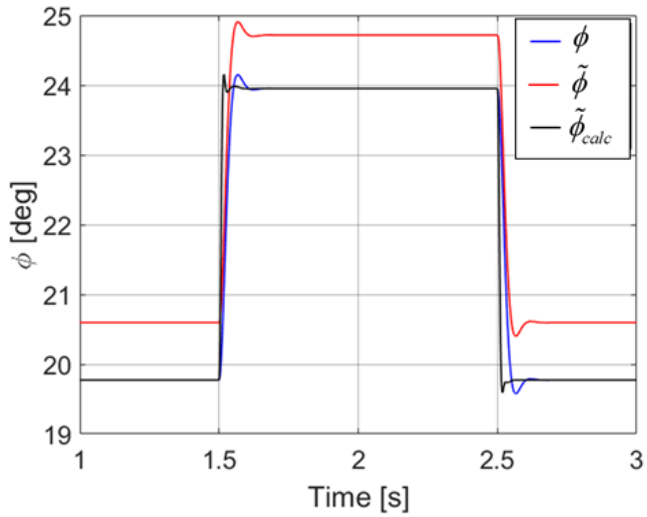

Figure 5.8. Load angle comparison from the system, reduced order observer, and calculated from the reduced order estimated load torque.

5.3 Reduced Order Observer Estimation of Wind Torque

A subset of wind data was provided by Xzeres Wind Corporation from a 10 kW wind turbine. The data included rotor angular speed, ω_a [rad/s] and aerodynamic power, P [W], from which aerodynamic torque, T_a was calculated using the following [24]:

$$T_a = \frac{P}{\omega_a} \quad \text{[Nm]} \tag{5.59}$$

The torque values were scaled down by a factor of 7, to accommodate the operating range of the magnetic gear, where the pull-out torque is $T_m = 147.8$ Nm. The resulting torque values were then fed into the reduced order observer model shown in Figure 5.5. Initially, the starting load angle for the system and the observer was set to $\phi_0 = 0^o$. A plot of the wind torque data and load torque estimation is shown in Figure 5.9 (a)-(b).

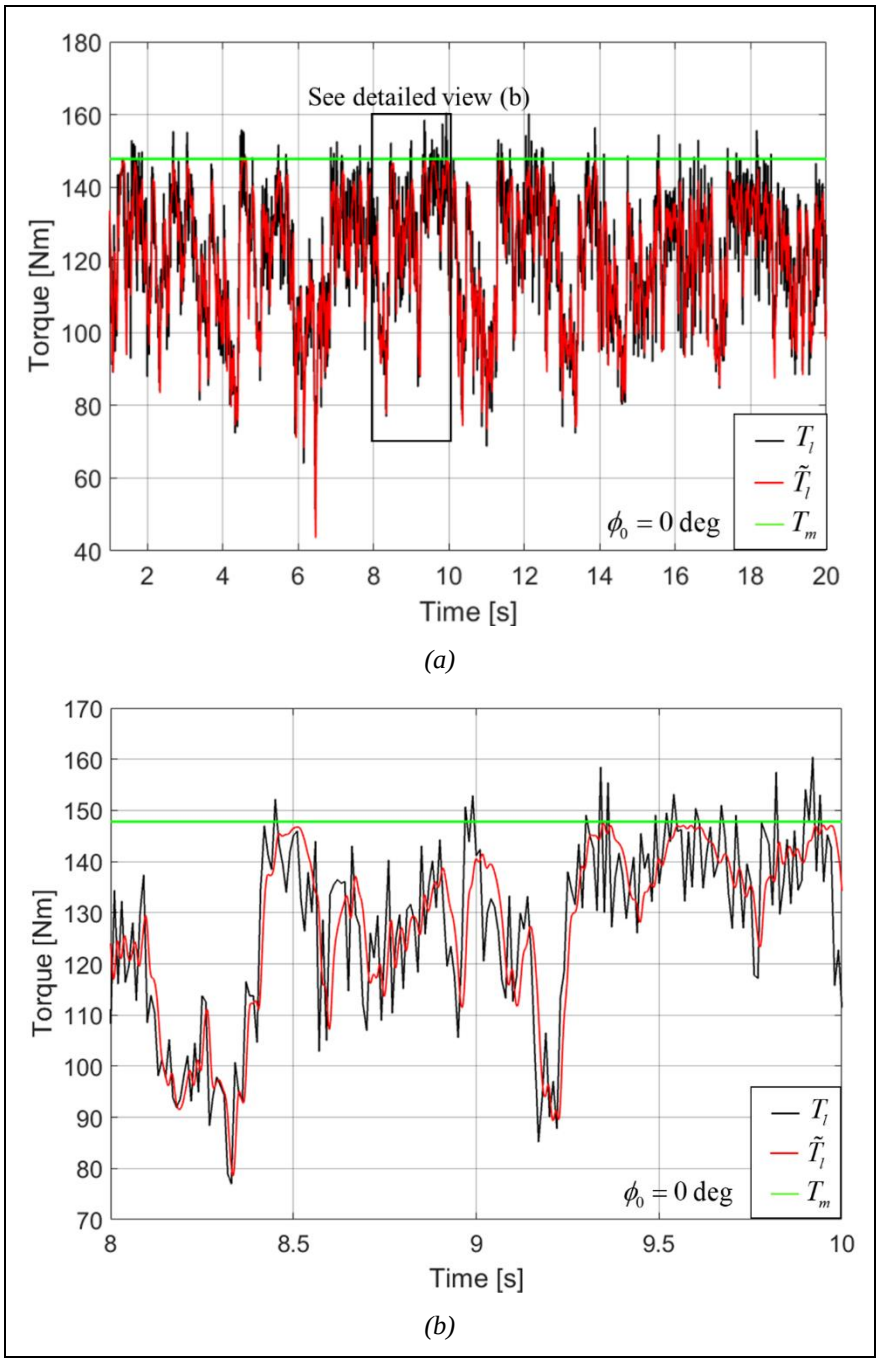

Figure 5.9. Plot of wind torque data obtained from [34] and reduced order estimated load torque (a) and detailed view (b), $\phi_0 = 0^o$.

It is clear that the observer is estimating the wind torque in broad trends but missing a lot of the content. Figure 5.10 (a)-(b) compares the load angle from the system fed from

wind torque data to the load angle calculated from the reduced order estimated load torque.

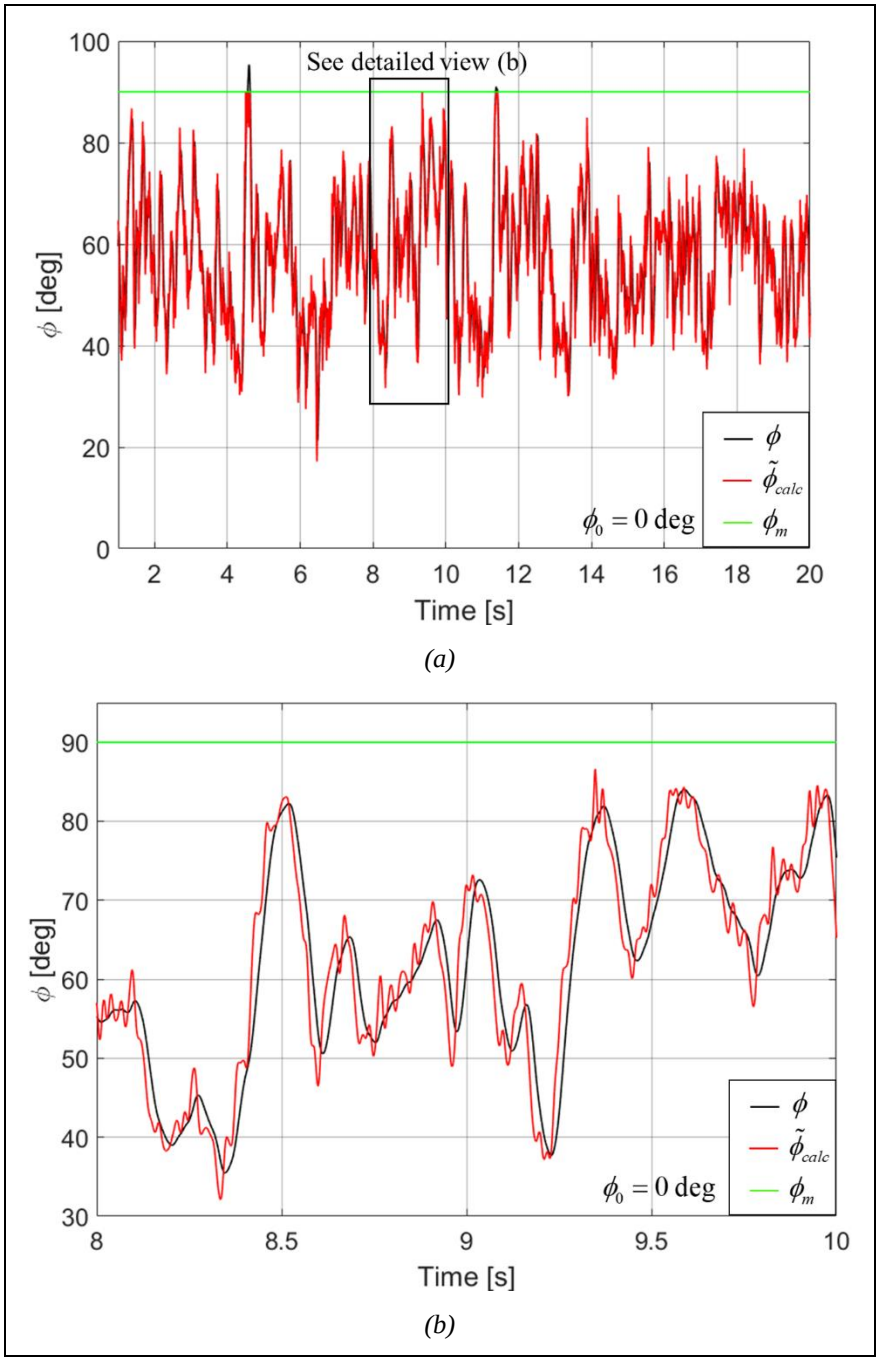

Figure 5.10. Transient plot of system load angle and load angle calculated from reduced order estimated load torque (a) and detailed view (b), $\phi_0 = 0$.

For comparison purposes, the average wind torque over the 20 s shown was calculated and then used to calculate the average load angle using (2.44). While this equation is for calculating steady-state load angle, it serves the purpose of approximation in this case. The average wind torque is 119 Nm, giving an average load angle of $\phi_0 = 53.6^o$. Figure 5.11 (a)-(b) show the wind torque data and reduced order estimated load torque data, when the reduced order estimator is linearized around $\phi_0 = 53.6^o$. Figure 5.12 (a)-(b) compare the resulting system load angle and load angle calculated from the reduced order estimate of the load torque.

Comparing the detailed plots of load torque (Figure 5.9 (b) and Figure 5.11 (b)), updating the load angle in the observer so that it is at least somewhat more representative of the system load angle produces better estimation of the load torque. While still missing some of the content, the load torque estimation at $\phi_0 = 53.6^o$ does capture more of the dynamic movement of the wind than it did linearized at $\phi_0 = 0^o$. Looking at the detailed load angle plots in Figure 5.10 (b) and Figure 5.12 (b), the calculated load angle is noisier than it was when the system was linearized around $\phi_0 = 0^o$, but the average appears to be tracking the system load angle well. To test that theory, an averaging filter was applied to the calculated load torque using a fundamental frequency of 20 Hz. The resulting plot in Figure 5.13 shows that the averaged load angle is far closer to the actual. For comparison purposes, Figure 5.14 shows the same filter applied to the calculated load angle, when the observer is linearized around $\phi_0 = 0^o$. The average is a better approximation of the system load angle for this linearization point as well. This may be a

potential application for filters, but the estimation noise might also be resolved if the observer were modified so that the load angle was dynamically updated.

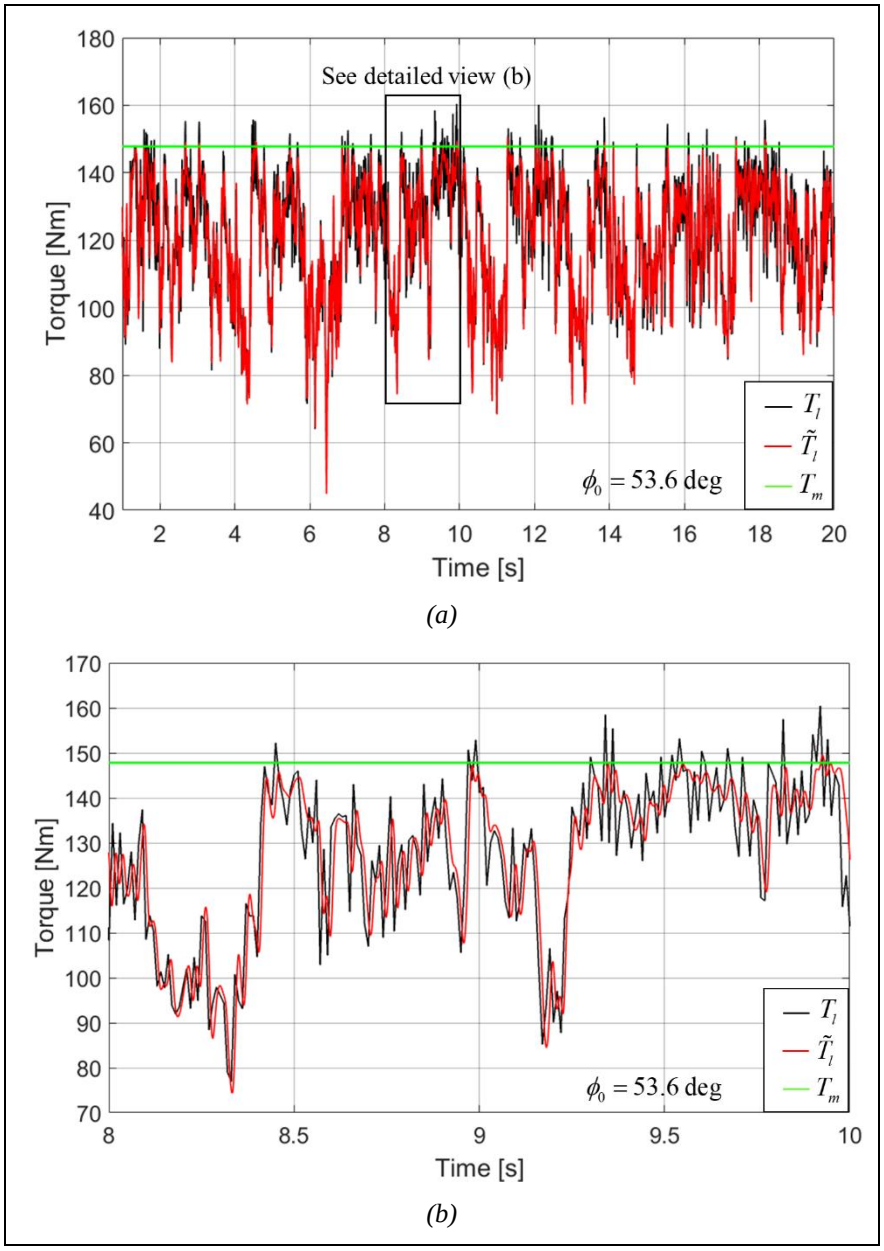

Figure 5.11. Plot of wind torque data obtained from [34] and reduced order estimated load torque (a) and detailed view (b), $\phi_0 = 53.6^o$.

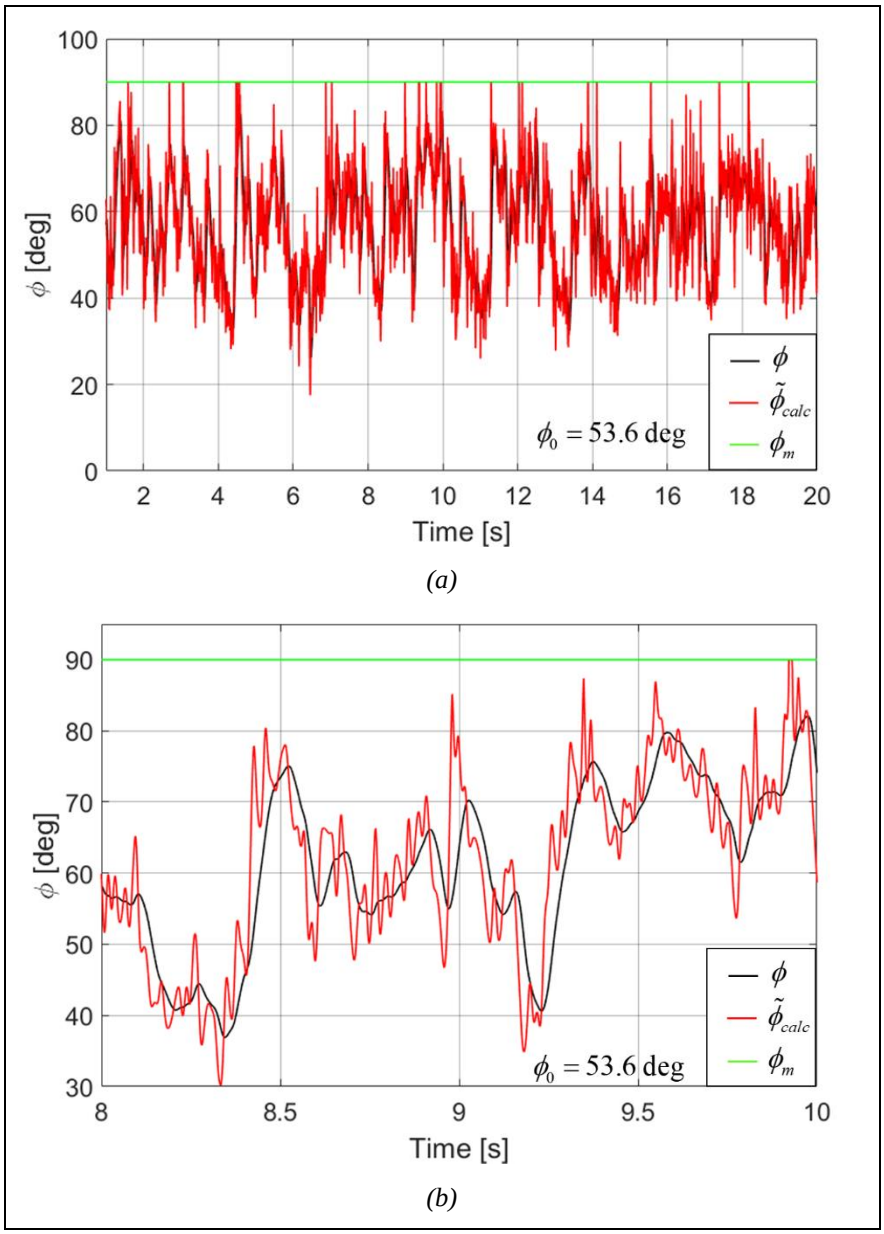

Figure 5.12. Transient plot of system load angle and load angle calculated from reduced order estimated load torque (a) and detailed view (b), $\phi_0 = 53.6^o$.

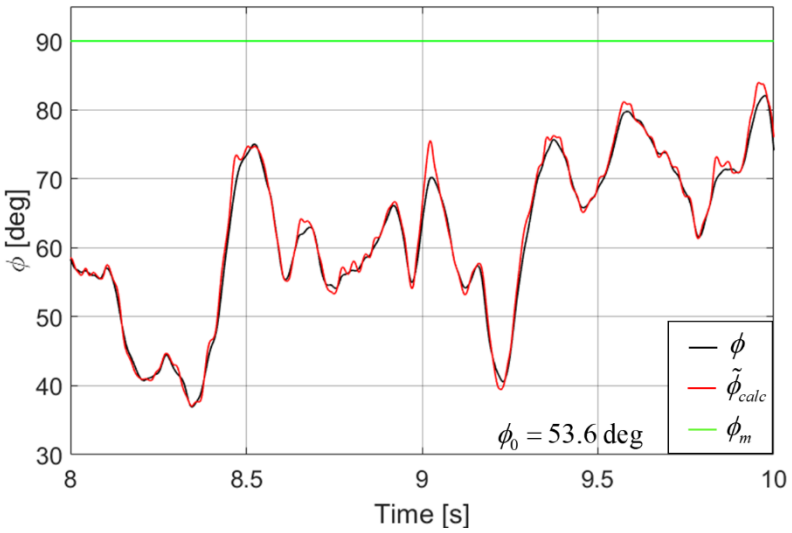

Figure 5.13. Transient plot of system load angle and load angle calculated from reduced order estimated load torque, $\phi_0 = 53.6^o$ and 20 Hz frequency averaging filter applied

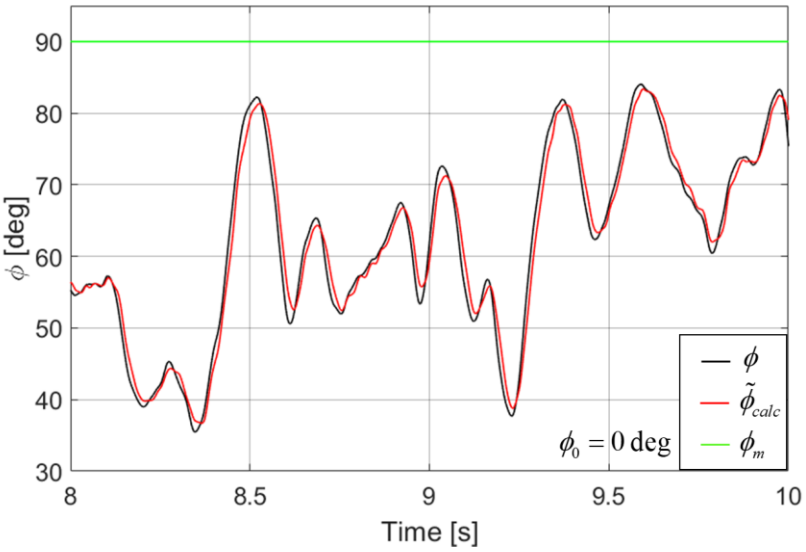

Figure 5.14. Transient plot of system load angle and load angle calculated from reduced order estimated load torque, $\phi_0 = 0^o$ and 20 Hz frequency averaging filter applied.

6 Conclusions and Areas for Future Research

The objective of this Master's thesis was to lay the groundwork for modeling, analyzing and optimizing control schemes for pole-slip prevention in a magnetically geared drivetrain. Systems of equations for the linear and nonlinear magnetic gear dynamics were developed. The open-loop dynamics were evaluated in the frequency domain and frequency domain techniques were used for pole placement design in a state feedback compensation controller. Linearized dynamic equations were used to build a state-space model of the system, the basis for a state feedback controller, full order observer and reduced order observer. A novel feedback regulation control structure was tested, utilizing load angle speed control that tracked 0 set point. A method of estimating the nonlinear system load angle was developed and tested against both step changes in load torque and changes in load torque from wind turbine data.

One key next step toward continuing this research effort would be to find a way to feed the load torque estimate or load angle calculation back into the reduced order observer so that it can update in real-time with changes to the system dynamics. While this thesis assumed that only the high-speed rotor speed was available for measurement, it would be interesting to expand the state space model to a MIMO structure to see if any combination of states would allow the observer to accurately calculate the system load dynamics. Once the load angle can be monitored accurately by the state estimator, the next step would be to set up a pole slip detection algorithm and explore how prevention and recovery can be achieved with integration into the broader control system of a wind turbine drivetrain.

References

[1] K. Atallah, S. D. Calverley, and D. Howe, "Design, analysis and realisation of a high-performance magnetic gear," *IEEE Proceedings on Electrical Power Applications,* vol. 151, no. 2, 3/2004 2004, doi: 10.1049.

[2] D. S. Painter, "A Comparative Study of the Performance Capabilities of Magnetic Gears," University Honors Theses, University Honors College, Portland State University, 2016.

[3] S. Connors, A. Kalmikov, and K. Dykes, "Wind Power Fundamentals," MIT, 2015.

[4] I. P. Girsang, J. S. Dhupia, E. Muljadi, M. Singh, and L. Y. Pao, "Gearbox and Drivetrain Models to Study Dynamic Effects of Modern Wind Turbines," presented at the IEEE Energy Conversion Conference, Denver, CO, 2013.

[5] Magnomatics. "Contactless, high-efficiency, high-torque transmission with inherent overload protection." http://www.magnomatics.com/pages/technology/low-ratio-magnetic-gears.htm (accessed March 3, 2019.

[6] K. Ogata, *Modern Control Engineering*. Upper Saddle River, NJ, USA: Prentice Hall, 2001.

[7] J. Ji and S. Sul, "Kalman Filter and LQ Based Speed Controller for Torsional Vibration Suppression in a 2-Mass Motor Drive System," *IEEE Transactions on Industrial Electronics,* vol. 42, no. 6, 1995.

[8] K. B. Lee, J. Y. Yoo, J. H. Song, and I. Choy, "Improvement of low speed operation of electric machine with an inertia identification using ROELO," *IEEE Proceedings on Electrical Power Applications,* vol. 151, no. 1, January 2004 2004.

[9] T. O'Sullivan, C. Bingham, and N. Schoefield, "High-Performance Control of Dual-Inertia Servo-Drive Systems Using Low-Cost Integrated SAW Torque Transducers," *IEEE Transactions on Industrial Electronics,* vol. 53, no. 4, pp. 1226-1237, 2006.

[10] T. O'Sullivan, C. Bingham, and N. Schofield, "Observer-based tuning of two-inertia servo-drive systems with integrated SAW torque transducers," *IEEE Transactions on Industrial Electronics,* vol. 54, no. 2, 2007.

[11] G. Shahgholian, "Modeling and Simulation of a Two-Mass Resonant System with Speed Controller," *International Journal of Information and Electronics Engineering,* vol. 3, no. 5, 2013.

[12] A. Waqas, "Speed Control of Electrical Drives with Resonant Loads," MS in Technology, Electrical Engineering, Aalto University, 2011.

[13] G. Zhang and J. Furusho, "Speed control of a two-inertia system by PI/PID control," *IEEE Transactions on Industrial Electronics,* vol. 47, no. 3, pp. 603-609, 2000.

[14] L. Yi and M. Tomizuka, "Robust Motion Control of Mechanical Systems with Compliance," in *35th Conference on Decision and Control*, Kobe, Japan, 1996: IEEE.

[15] R. Dhaouadi, K. Kubo, and M. Tobise, "Robust speed control of rolling mill drive systems using the loop transfer recovery design methodology," in *International Conference on Industrial Electronics, Control and Instrumentation*, 1991: IEEE.

[16] R. Montague, "Control of Drive Trains Incorporating Magnetic Gears," PhD, Electronic and Electrical Engineering, University of Sheffield, 2014.

[17] M. Desvaux, R. Latimier, B. Multon, S. Sire, and H. B. Ahmed, "Analysis of the dynamic behaviour of magnetic gear with nonlinear modellling for large wind turbines,"

presented at the International Conference on Electrical Machines, Lausanne, France, 9/2016, 2016.
[18] M. Bouheraoua, "Control of Pseudo Direct Drive Permanent Magnet Machines," Ph.D, Department of Electronic and Electrical Engineering, University of Sheffield, 2013.
[19] M. Bouheraoua, J. Wang, and K. Atallah, "Speed Control for a Pseudo Direct Drive Permanent Magnet Machine With One Position Sensor on Low-Speed Rotor," *IEEE Transactions on Industrial Electronics,* vol. 50, no. 6, pp. 3825-3833, 11/2014 2014.
[20] M. Bouheraoua, J. Wang, and K. Atallah, "Design and implementation of an observer-based state feedback controller for a pseudo-direct drive," *IET Electric Power Applications,* vol. 7, no. 8, pp. 643-653, 6/19/2013 2013, doi: 10.1049.
[21] R. Montague and C. Bingham, "Nonlinear Control of Magnetically-geared Drive Trains," *International Journal of Automation and Computing,* vol. 10, no. 4, pp. 319-326, 2013.
[22] R. Montague, C. Bingham, and K. Atallah, "Servo Control of Magnetic Gears," *IEEE Transactions on Mechatronics,* vol. 17, no. 2, pp. 29-278, 2011.
[23] R. Montague, C. Bingham, and K. Atallah, "Magnetic Gear Pole-Slip Prevention Using Explicit Model Predictive Control," *IEEE Transactions on Mechatronics,* vol. 18, no. 5, pp. 1535-1543, 2012.
[24] A. Merabet, J. Gu, and J. Thongam, "Torque and pitch angle control for variable speed wind turbines operating in all operating regimes," presented at the 10th International Conference on Environment and Electrical Engineering, Roma, Italy, May 2011, 2011.
[25] D. Wong, J. Bird, D. Barnett, and W. Williams, "A High Torque Density Halbach Rotor Magnetic Gearbox". Presented at the International Electric Machines and Drives Conference, San Diego, May 12-15.
[26] K. Halbach, "Design of permanent multipole magnets with oriented rare earth cobalt material," *Nuclear Instructional Methods,* vol. 187, pp. 1-10, 1980.
[27] L. Jian and K. T. Chau, "A Coaxial Magnetic Gear with Halbach Permanent Magnet Arrays," *IEEE Transactions on Energy Conversion,* vol. 25, no. 2, 2010.
[28] M. Singh, M. Vyas, and S. Santoso, "Using Generic Wind Turbine Models to Compare Inertial Response of Wind Turbine Technologies," presented at the IEEE PES General Meeting, Providence, RI, 2010.
[29] R. Dorf and R. Bishop, *Modern Control Systems*, 12th ed. Upper Saddle River, NJ: Prentice Hall, 2011.
[30] R. Tymerski and F. Rytkonen. P. S. University. (2017). Classical and Modern Control Design: with examples from power electronics.
[31] J. S. Bay, *Fundamentals of Linear State Space Systems*. McGraw Hill, 1999.
[32] B. Friedland, *Control System Design: An Introduction To State-Space Methods*. UK: McGraw-Hill, 1986.
[33] R. T. Stefani, B. Shahian, C. J. Savant, and G. H. Hostetter, *Design of Feedback Control Systems*, 4th ed. Oxford, NY: Oxford University Press, 2002.
[34] B. Fleskes. *10 kW Wind Turbine Power Data*.